

A census of the stellar content in the protocluster core SPT2349–56 at $z = 4.3$

Ryley Hill,¹ Scott Chapman,^{1,2,3} Kedar A. Phadke,⁴ Manuel Aravena,⁵ Melanie Archipley,^{4,6} Matthieu Béthermin,⁷ Rebecca E. A. Canning,⁸ Anthony Gonzalez,⁹ Thomas R. Greve,^{10,11,12} Gayathri Gururajan,⁷ Christopher C. Hayward,¹³ Yashar Hezaveh,^{13,14} Sreevani Jarugula,⁴ Daniel P. Marrone,¹⁵ Tim Miller,¹⁶ Cassie Reuter,⁴ Kaja Rotermund,³ Douglas Scott,¹ Justin Spilker,^{17,18} Joaquin D. Vieira,^{4,6} George Wang,¹ Axel Weiß¹⁹

¹Department of Physics and Astronomy, University of British Columbia, 6225 Agricultural Road, Vancouver, V6T 1Z1, Canada

²National Research Council, Herzberg Astronomy and Astrophysics, 5071 West Saanich Road, Victoria, V9E 2E7, Canada

³Department of Physics and Atmospheric Science, Dalhousie University, 6310 Coburg Road, B3H 4R2, Halifax, Canada

⁴Department of Astronomy, University of Illinois, 1002 West Green Street, Urbana, IL 61801, USA

⁵Núcleo de Astronomía, Facultad de Ingeniería y Ciencias, Universidad Diego Portales, Av. Ejército 441, Santiago, 8320000, Chile

⁶Center for Astrophysical Surveys, National Center for Supercomputing Applications, Urbana, IL, 61801, USA

⁷Laboratoire d'Astrophysique de Marseille, 38 rue Frédéric Joliot-Curie, Marseille, 13013, France

⁸Institute of Cosmology and Gravitation, University of Portsmouth, Dennis Sciama Building, Portsmouth, PO1 3FX, UK

⁹Department of Astronomy, University of Florida, 211 Bryant Space Science Center, Gainesville, FL 32611-2055, USA

¹⁰Cosmic Dawn Center

¹¹DTU Space, Technical University of Denmark, Elektrovej 327, Kgs. Lyngby, DK-2800, Denmark

¹²Department of Physics and Astronomy, University College London, Gower Street, London, WC1E 6BT, UK

¹³Center for Computational Astrophysics, Flatiron Institute, 162 Fifth Avenue, New York, NY 10010, USA

¹⁴Département de Physique, Université de Montréal, 1375 Avenue Thérèse-Lavoie-Roux, Montréal, H2V 0B3, Canada

¹⁵Steward Observatory, University of Arizona, 933 North Cherry Avenue, Tucson, AZ 85721, USA

¹⁶Department of Astronomy, Yale University, 52 Hillhouse Avenue, New Haven, CT 06511, USA

¹⁷Department of Astronomy, University of Texas at Austin, 2515 Speedway, Stop C1400, Austin, TX 78712, USA

¹⁸NHFP Hubble Fellow

¹⁹Max-Planck-Institut für Radioastronomie, Auf dem Hügel 69, Bonn, D-53121, Germany

September 2021

ABSTRACT

The protocluster core SPT2349–56 at $z = 4.3$ is one of the most actively star-forming regions known, yet constraints on the total stellar mass of this system are highly uncertain. We have therefore carried out deep optical and infrared observations of this system, probing rest-frame ultraviolet to infrared wavelengths. Using the positions of the spectroscopically-confirmed protocluster members, we identify counterparts and perform detailed source deblending, allowing us to fit spectral energy distributions in order to estimate stellar masses. We show that the galaxies in SPT2349–56 have stellar masses proportional to their high star-formation rates, consistent with other protocluster galaxies and field submillimetre galaxies (SMGs) around redshift 4. The galaxies in SPT2349–56 have on average lower molecular gas-to-stellar mass fractions and depletion timescales than field SMGs, although with considerable scatter. We construct the stellar-mass function for SPT2349–56 and compare it to the stellar-mass function of $z = 1$ galaxy clusters, finding both to be best described by a Schechter function. We measure rest-frame ultraviolet half-light radii from our *HST*-F160W imaging, finding that on average the galaxies in our sample are similar in size to typical star-forming galaxies around the same redshift. However, the brightest *HST*-detected galaxy in our sample, found near the luminosity-weighted centre of the protocluster core, remains unresolved at this wavelength. Hydrodynamical simulations predict that the core galaxies will quickly merge into a brightest cluster galaxy, thus our observations provide a direct view of the early formation mechanisms of this class of object.

Key words: galaxies – formation: galaxies – evolution: submm – galaxies

1 INTRODUCTION

Today, the large-scale structure of our Universe is made up of filaments, nodes, and voids, a structure that is often described as the ‘cosmic web’. The nodes of this cosmic web are comprised of galaxy

clusters, which are the largest gravitationally bound objects in the Universe. Being such fundamental building blocks, galaxy clusters are well-studied objects; we know that they are seeded by small-amplitude density fluctuations of the sort observed in the cosmic

microwave background (CMB), which then grew and collapsed into the massive structures that we see today. While the CMB is very well understood (e.g. [Planck Collaboration I 2020](#)), and the details of present-day galaxy clusters are well-described (e.g., [Biviano 1998](#); [Giodini et al. 2013](#); [Bykov et al. 2015](#)), the intermediate phase of evolution, which has become known as the realm of galaxy ‘proto-clusters’, still lacks sufficient observations to pin down the models (e.g. [Overzier 2016](#)).

Traditional galaxy cluster searches have made use of the fact that these objects are virialized, allowing the intergalactic gas to heat up and be detected by X-ray facilities (e.g., [Rosati et al. 2009](#); [Gobat et al. 2011](#); [Andreon et al. 2014](#); [Wang et al. 2016](#); [Mantz et al. 2018](#)) or at millimetre wavelengths via the Sunyaev-Zeldovich (SZ) effect (e.g., [Planck Collaboration XXVII 2016](#); [Bleem et al. 2015](#); [Huang et al. 2020](#)). However, beyond redshifts of around 2, these signatures become too faint for practical detection. Protocluster-detection techniques now include searching large optical and infrared sky maps for overdensities of red galaxies (e.g., [Martinache et al. 2018](#); [Greenslade et al. 2018](#)), Lyman-break galaxies (LBGs; e.g., [Steidel et al. 2000](#); [Dey et al. 2016](#)), or Lyman- α emitters (LAEs; e.g., [Shimasaku et al. 2003](#); [Tamura et al. 2009](#); [Chiang et al. 2015](#); [Dey et al. 2016](#); [Harikane et al. 2019](#)), and searching the area surrounding rare and luminous sources or groups of sources such as radio-loud active galactic nuclei (AGN; e.g., [Steidel et al. 2005](#); [Venemans et al. 2007](#); [Dannerbauer et al. 2014](#)) or submillimetre galaxies (SMGs; e.g., [Chapman et al. 2009](#); [Umehata et al. 2015](#); [Casey et al. 2015](#); [Hung et al. 2016](#); [Oteo et al. 2018](#); [Lacaille et al. 2019](#); [Long et al. 2020](#)).

Another protocluster-selection technique that has recently been gaining attention comes from experiments designed to map the CMB. These experiments typically aim to cover huge areas of the sky at submillimetre and millimetre wavelengths with resolution on the order of a few arcminutes, and in the process find some of the brightest and rarest submillimetre and millimetre sources in the sky. After the application of various selection criteria to remove Galactic sources and quasars/blazars, follow-up observations with higher-resolution telescopes have subsequently revealed that many of the remaining sources are gravitational lenses ([Negrello et al. 2010](#); [Hezaveh et al. 2013](#); [Cañameras et al. 2015](#); [Spilker et al. 2016](#)), or genuine overdensities of luminous star-forming galaxies, representing ideal proto-cluster candidates ([Planck Collaboration XXVII 2015](#); [Flores-Cacho et al. 2016](#); [Miller et al. 2018](#); [Kneissl et al. 2019](#); [Hill et al. 2020](#); [Wang et al. 2020](#); [Koyama et al. 2020](#)).

One such source, SPT2349–56, was discovered in the South Pole Telescope’s extragalactic mm-wave point-source catalogue ([Vieira et al. 2010](#); [Mocanu et al. 2013](#); [Everett et al. 2020](#)), and is now known to contain dozens of spectroscopically-confirmed galaxies ([Miller et al. 2018](#); [Hill et al. 2020](#)), several LBGs ([Rotermund et al. 2021](#)), and a number of LAEs, alongside a Lyman- α blob ([Apostolovski et al. in prep.](#)). This protocluster lies at a redshift of 4.3 and has an integrated star-formation rate (SFR) of over $10,000 M_{\odot} \text{ yr}^{-1}$ within a diameter of about 500 proper kiloparsecs, well above what is seen in current simulations ([Lim et al. 2021](#)). Hydrodynamical simulations using the known galaxies in SPT2349–56 as the initial conditions predict that most of the galaxies in the centre of this object will merge into a single brightest cluster galaxy (BCG; [Rennehan et al. 2020](#)) over a timescale of a few hundred million years. SPT2349–56 is believed to be the core of a Mpc-scale protocluster, as evidenced by several infalling subhalos found around it ([Hill et al. 2020](#)).

Optical observations of SPT2349–56 were initially carried out using the GMOS and FLAMINGOS-2 instruments mounted on the Gemini South telescope, and *Spitzer*-IRAC was used to observe this protocluster core in the infrared ([Rotermund et al. 2021](#)). These data

were used to obtain rest-frame ultraviolet photometry for nine out of the 14 galaxies originally reported by [Miller et al. \(2018\)](#), as well as identifying four LBGs at the same redshift as the structure. While the photometric coverage was sparse, owing to the faintness of the known galaxies in the optical, initial spectral energy distribution (SED) fits suggested that the core has a stellar mass of at least $10^{12} M_{\odot}$, and the nine detected galaxies appeared to show significant scatter around the $z=4$ galaxy main sequence (MS). A search for an overdensity of LBGs out to about 1 Mpc found that the overdensity was too low to meet large-field optical survey criteria, meaning that SPT2349–56 would not be picked up by traditional optical surveys searching for distant protoclusters.

We have now significantly bolstered our optical and infrared coverage of SPT2349–56 using the *Hubble Space Telescope* (*HST*), and by increasing our *Spitzer*-IRAC integration time by a factor of 10. In addition, we now know of over 30 galaxy protocluster members. In this paper, we use these new data to analyse the ultraviolet and infrared properties of this much larger sample of protocluster members.

In Section 2 we describe these new observations in detail. In Section 3 we outline our data reduction procedure, including deblending, source matching, flux density extraction, SED fitting, and profile fitting. In Section 4 we show our results, in Section 5 we discuss the implications of these observations, and the paper is concluded in Section 6.

2 OBSERVATIONS

2.1 *HST*

HST observed SPT2349–56 with the WFC3 instrument in the F110W and F160W filters during Cycle 26 (proposal ID 15701, PI S. Chapman). Two orbits were carried out for the F110W filter, totalling 1.6 hours on-source, and three orbits were carried out for the F160W filter, totalling 2.4 hours on-source. Since the WFC3 detector pixels undersample the PSF (the plate scale is $0.13 \text{ arcsec pixel}^{-1}$, with a FWHM around 1 pixel), the observations utilized a standard sub-pixel dither pattern in order to fully sample the PSF. The field-of-view of the WFC3 instrument is about 4.7 arcmin^2 , sufficiently large to image all of the protocluster members in the core, as well as the northern component. We note that [Hill et al. \(2020\)](#) found CO(4–3) line emission at $z=4.3$ from three galaxies in a targeted ALMA Band 3 observation of a red *Herschel*-SPIRE source (named ‘SPIREc’) located about 1.5 Mpc from the main structure, but these three galaxies are not covered by the *HST* imaging.

The data were calibrated using `calwf3`, part of the standard *HST* WFC3 pipeline `wfc3tools` available in `python`.¹ The individual exposures were stacked using `astrodrizzle`; the stacking method used was the median, and sky subtraction was performed. We set the final pixel scale to be $0.075 \text{ arcsec pixel}^{-1}$, approximately Nyquist sampling (i.e. sampling by a factor of 2) the beam. The final rms reached in these images is 0.50 nJy for the F110W filter (corresponding to a 5σ AB magnitude limit of 30.4), and 0.79 nJy for the F160W filter (corresponding to a 5σ AB magnitude limit of 29.9). $2 \text{ arcmin} \times 2 \text{ arcmin}$ cutouts of the images, smoothed by a 3-pixel FWHM Gaussian, are shown in Fig. 1.

¹ <https://github.com/spacetelescope/wfc3tools>

2.2 IRAC

The *Spitzer* Space Telescope was used to observe SPT2349–56 at two wavelengths: $3.6\ \mu\text{m}$ (hereafter ‘ch1’) and $4.5\ \mu\text{m}$ (hereafter ‘ch2’). A total of four observations have now been carried out since 2009, the first two of which were presented in [Rotermund et al. \(2021\)](#), where further details can be found. The two subsequent observations used in this paper were carried out in January 2018 (proposal ID 13224, PI S. Chapman) and October 2019 (proposal ID 14216, PI S. Chapman), and uniformly covered ch1 and ch2 with $324 \times 100\text{ s}$ dithered exposures (162 exposures per observation for each channel). These new data provide a factor of 10 more exposure time, reducing the instrumental rms by a factor of about 3. Given IRAC’s very large field-of-view (about $27\ \text{arcmin}^2$), all protocluster members known to date (including the three SPIREc sources) were covered by these observations.

Data from all four observations were combined and set to a pixel scale of $0.6\ \text{arcsec pixel}^{-1}$. The final rms levels of the stacked data are $6.9\ \text{nJy}$ for ch1 (corresponding to a 5σ AB magnitude limit of 27.5), and $6.5\ \text{nJy}$ for ch2 (corresponding to a 5σ AB magnitude limit of 27.6). Cutouts showing the $2\ \text{arcmin} \times 2\ \text{arcmin}$ region around the main structure are shown in Fig. 1.

2.3 Gemini

The Gemini observations used in this paper were presented in [Rotermund et al. \(2021\)](#), where details of the imaging, calibration, and data reduction can be found. Here we only provide a brief summary. Since the data were taken before many new protocluster members had been confirmed, we also outline which of these new galaxies are covered by the observations.

Data were taken in the g , r , and i bands using the GMOS instrument ([Hook et al. 2004](#)), and similarly in the K_s band using the FLAMINGOS-2 instrument ([Eikenberry et al. 2004](#)), both of which are part of the Gemini South Observatory. The rms levels reached in these images are 0.2, 0.3, 0.6, and $15.0\ \text{nJy}$, respectively. For the GMOS instrument, the g -, r -, and i -band images have a field-of-view of $5.5\ \text{arcmin}^2$ and cover all of the core and northern sources, but not the three SPIREc galaxies located $1.5\ \text{Mpc}$ away from the core.

Apostolovski et al. (in prep.) also reports seven LAEs at $z=4.3$, four of which are in the central component of the protocluster, while the remaining three are found in the northern component. These seven galaxies are also covered by the GMOS imaging, and will be included in the analysis below. Finally, [Rotermund et al. \(2021\)](#) identified four LBGs around the core of SPT2349–56; they identify one of the LBGs (LBG1) with a galaxy from [Hill et al. \(2020\)](#) found in the ALMA data (C17), one (LBG4) with an LAE (LAE3), with the remaining two LBGs being unique. However, they note that one of their unique LBGs, LBG2, lies close to galaxy C2 from [Hill et al. \(2020\)](#), and could also be a counterpart. In this paper, we treat LBG2 as the counterpart to C2 as it lies within the $1\ \text{arcsec}$ search radius criteria we outline in Section 3.3, and we include the other unique LBG, LBG3, as a separate source in our analysis below.

For the FLAMINGOS-2 instrument, the field-of-view is circular with a diameter of $6.1\ \text{arcmin}$. While this field-of-view is large enough to cover all of the core and northern sources described above, due to a lack of nearby guide stars within the field, we were only able to cover the central sources down to a depth suitable for the detection of the target galaxies in our sample. These include the 23 galaxies from [Hill et al. \(2020\)](#) found through their [CII] emission, four LAEs, and the LBG. Fig. 1 shows $2\ \text{arcmin} \times 2\ \text{arcmin}$ cutouts for each of these four Gemini fields, smoothed by a 3-pixel FWHM Gaussian.

3 DATA ANALYSIS

3.1 Gemini and *HST* flux density measurements

We first matched our GEMINI GMOS, FLAMINGOS-2, and *HST* F110W astrometry to our *HST*-F160W astrometry using the python package `astroalign` ([Beroiz et al. 2020](#)), which identifies bright stars in source and target images and estimates a transformation matrix that aligns the stars in the target image with the same stars in the source image. We note that we are unable to apply this step to our ALMA data because there are no bright sources easily identifiable in both our *HST*-F160W imaging and our ALMA imaging; however, as shown below, after matching sources across both images we do not find any significant systematic offsets.

We ran `source-extractor` ([Bertin & Arnouts 1996](#)) on our GEMINI-GMOS and FLAMINGOS-2 images to extract a catalogue of sources and measure their flux densities. For the detection portion of the process, we smoothed the images with a 3 pixel (FWHM) Gaussian filter and extracted peaks where three adjacent pixels were above 0.8 times the background rms – in `source-extractor` this means setting `DETECT_MINAREA` to 3 and `DETECT_THRESH` to 0.8. These parameters are similar to the ones used by [Rotermund et al. \(2021\)](#), who set `DETECT_MINAREA` to 3 and varied `DETECT_THRESH` between 1.1 and 2.5, depending on the band.

Once sources were located, their flux densities were measured in the unfiltered images using the `FLUX_BEST` option in `source-extractor`, which selects either the flux measured in an adaptively-scaled elliptical aperture (`FLUX_AUTO`) or sums the pixels found above the chosen threshold, with a correction for missing flux in the wings of the objects (`FLUX_ISOCOR`). When crowding becomes an issue, the `FLUX_AUTO` apertures start double counting the flux densities in pixels. For a given source, if 10 per cent of the `FLUX_AUTO` measurement comes from other sources, `FLUX_ISOCOR` is chosen, otherwise `FLUX_AUTO` is chosen.

HST WFC3 source catalogues were produced using `source-extractor` as well, using the same input parameters described above, except we required nine adjacent pixels to be above 1.2 times the background rms. This setup is similar to the `source-extractor` parameters used in the CANDELS survey ([Galametz et al. 2013](#)) in the ‘hot’ mode, which is optimized to detect small and faint galaxies.

3.2 IRAC deblending and flux density measurements

Owing to *Spitzer*’s poor angular resolution compared to Gemini and *HST*, source blending can become a serious issue, especially in crowded regions like the centre of SPT2349–56. To tackle this issue, we use the publicly-available code `t-phot` ([Merlin et al. 2015, 2016](#)), which uses a high-resolution source catalogue as a prior to deblend a low-resolution, blended image.

To construct an optimal high-resolution catalogue, we stacked (as a weighted mean) both of our F110W and F160W *HST* images. We then ran `source-extractor` with a higher detection threshold (`DETECT_MINAREA` = 9 and `DETECT_THRESH` = 2.0), since having too many faint galaxies used as priors with `t-phot` leads to unrealistic deblending. We also turned off source deblending by setting `DEBLEND_MINCONT` to 1. This means that within a collection of pixels found above the predefined threshold, local maxima will not be classified as individual sources. This step is necessary because `t-phot` becomes unreliable when given blended priors. We output a segmentation map from `source-extractor`, which is used in conjunction with the catalogue in `t-phot`.

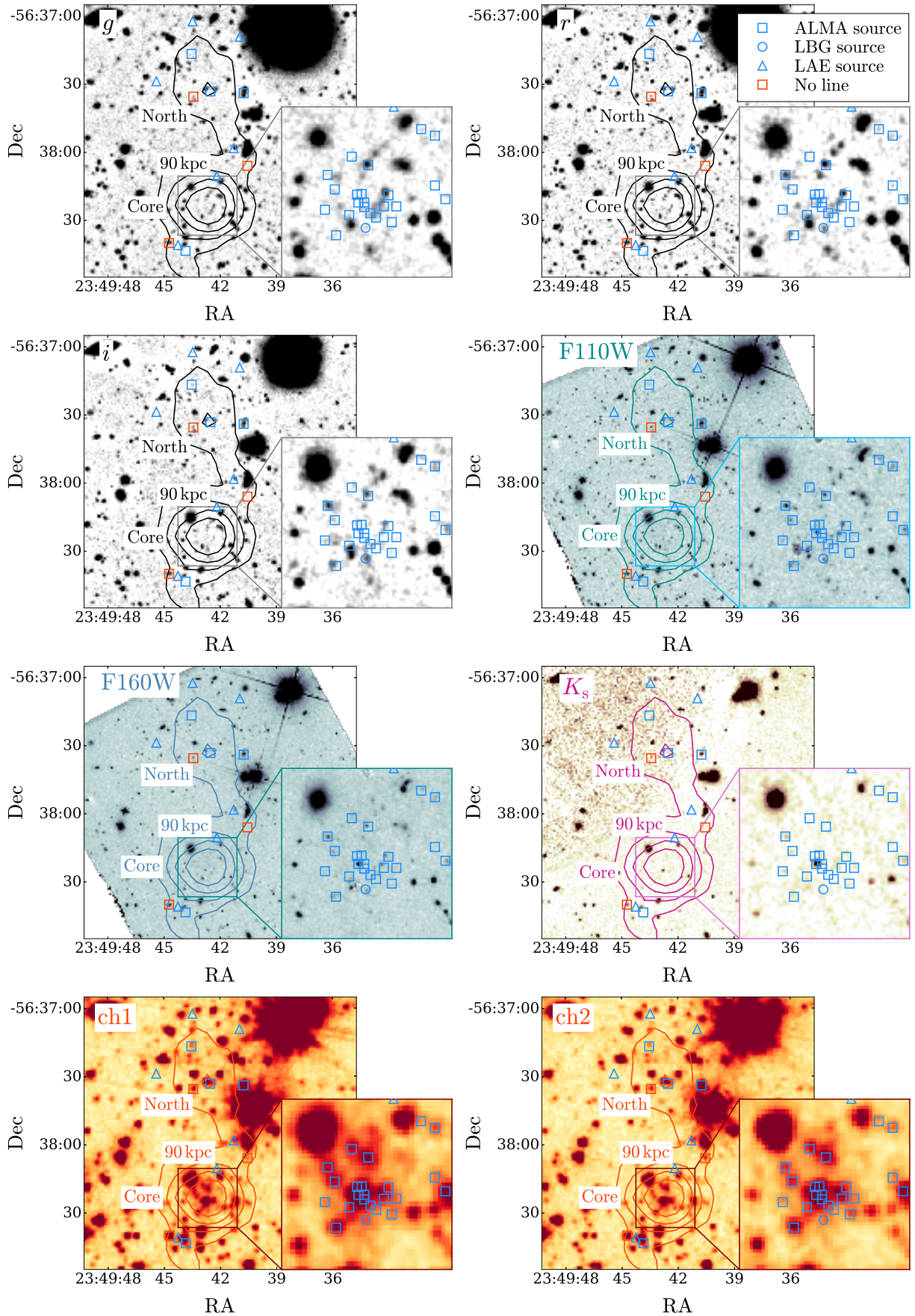


Figure 1. Optical and infrared images of SPT2349–56. ALMA sources are shown as blue squares, the LBG source as a blue circle, LAE sources as blue triangles, and submm-detected sources with no line emission (i.e. likely foreground/background sources) as red squares. The images are smoothed by a 3-pixel FWHM Gaussian, except for the IRAC images, which have not been smoothed. Single-dish submm imaging of SPT2349–56 at $870\ \mu\text{m}$ using the LABOCA instrument are shown as the background contours, starting at 4σ and increasing in steps of 5σ , and define the core and northern regions of this protocluster field (see [Hill et al. 2020](#); [Wang et al. 2020](#)).

The code `t-phot` requires that the pixel scale of the input prior catalogue is an integer multiple of the low-resolution image, and is also aligned to the same pixel grid. To satisfy these criteria, we used the same `astroalign` code to align our IRAC data to our high-resolution *HST* data, and then we used the `python` function `reproject_interp` from the module `reproject` to reproject our IRAC images onto our combined *HST* image, thus making the IRAC pixels a factor of 8 smaller.

`t-phot` also requires a convolution kernel that can be used with the high-resolution segmentation image to produce the low-resolution template. Assuming that the galaxies in our *HST* image are resolved, the appropriate kernel would simply be the IRAC PSF. However, owing to the variation in sensitivity across each IRAC pixel, a more complex point response function (PRF) is more appropriate. A set of 5×5 PRFs are available from the NASA/IPAC Infrared Science Archive,² where each PRF is the response from a point source illuminating a position on a pixel divided up into a 5×5 grid. For the convolution kernel, we selected the PRF corresponding to a point source illuminating the centre of a pixel. The provided PRFs have a pixel scale of $0.24 \text{ arcsec pixel}^{-1}$, and we used the same `reproject` function to reproject these pixels to the high-resolution pixel scale of $0.075 \text{ arcsec pixel}^{-1}$.

Some sources of interest are not detected in the combined *HST* image, but are clearly seen in the IRAC data. For these sources, `t-phot` enables one to provide a second catalogue of unresolved priors as a list of positions that will be treated as delta functions before being convolved with the kernel. Five galaxies from Hill et al. (2020) fit this category, and were provided to `t-phot` as unresolved priors, namely C4, C5, C9, C10, and NL1.

With these inputs in hand, we then ran `t-phot` in two passes. The first pass convolves the high-resolution segmentation image with the kernel, and fits an amplitude to each source to best match the low-resolution image. The second pass cross-correlates the model image with the low-resolution image in order to compute small positional shifts for each source, and then fits for the amplitudes a second time.

Since our high-resolution *HST* imaging did not cover the SPIREc sources, their flux densities were measured independently. We performed aperture photometry at the positions of the three SPIREc sources, using an aperture with a radius of 4 pixels (2.4 arcsec), and applied aperture corrections of 1.208 and 1.220 for ch1 and ch2, respectively (from the IRAC Instrument Handbook³). SPIREc1 and SPIREc3 are both clearly detected and we were able to measure their flux densities with high signal-to-noise ratio (SNR). SPIREc2 is not a clear detection by eye, and the flux density in the aperture in ch1 is consistent with noise, but in ch2 we were able to measure a 3σ signal.

3.3 Source matching

In order to perform a multiwavelength analysis of the SEDs of these galaxies, we need to match our sources detected in high-resolution (sub)millimetre imaging to their counterparts in our optical and infrared imaging. This becomes complicated due to the fact that the (sub)millimetre imaging is detecting emission from dust, while the ultraviolet to near-infrared imaging is detecting emission from starlight (including extinction by dust). A galaxy’s morphology can

be quite complicated in detail, with patches of dust and stars that will not necessarily overlap one another from our line of sight (e.g. Goldader et al. 2002).

Theoretically, the 1σ uncertainty of our ALMA-derived positions is given by

$$\Delta\text{RA} = \Delta\text{Dec} = \frac{1}{2\sqrt{\ln 2}} \frac{\text{FWHM}}{\text{SNR}}, \quad (1)$$

where FWHM is the size of the synthesized beam, and SNR is the signal-to-noise ratio of the peak pixel (Ivison et al. 2007). For our ALMA positions, the synthesized beam is about 0.5 arcsec (Hill et al. 2020), so we expect the 1σ radial uncertainty to be $\Delta r \approx 0.3 \text{ arcsec}/\text{SNR}$. Since the probability density of finding a source a distance r from its true position is proportional to $re^{-r^2/2\Delta r^2}$, one must go out to a distance of $3.42\Delta r$ in order to find a correct match with 99.7 per cent (or 3σ) certainty. For our ALMA positions, the lowest (spatial) SNR used to measure a position was about 4, meaning a 3σ search should go out to about 0.3 arcsec. However, this becomes more complicated in practice due to the fact that the (sub)millimetre and optical images could have different morphologies, especially for the case of mergers. Previous studies matching ALMA galaxies to *HST* counterparts have used radial searches around 0.6–1 arcsec (e.g., Dunlop et al. 2017; Long et al. 2020), and here we also adopt 1 arcsec, corresponding to about 6.9 proper kiloparsecs. For comparison, the typical submm size of the galaxies in our sample is about 4 proper kiloparsecs (twice the half-light radius, see Hill et al. 2020).

A source is thus considered a match if it lies within 1 arcsec from the ALMA-derived positions provided in Hill et al. (2020), and we allow the possibility of multiple matches; multiple optical counterparts to a submm source are possible if the submm source is a merging galaxy, for example. For cases where a counterpart is less than 1 arcsec from two ALMA galaxies, we assign the match to the closest ALMA galaxy. We note that despite the comparatively large beamsize of the IRAC imaging, we use the same 1 arcsec matching criteria, since the IRAC positions are nearly identical to the high-resolution *HST* imaging, which is simply a result of using `t-phot` for the photometry. Also, for reference, 1 arcsec corresponds to 6.3 pixels in the GMOS images, 13.4 pixels in our WFC3 images, 5.6 pixels in the FLAMINGOS-2 image, and 1.7 pixels in the IRAC images.

Next, we take advantage of our extensive wavelength coverage by imposing the additional constraint that a counterpart is not detected in the *g* band – this is simply because at $z = 4.3$, the *g* band probes a galaxy’s rest-frame SED at 900 \AA , where these galaxies should be much fainter than the sensitivity limit of our Gemini data because of neutral hydrogen’s efficiency at absorbing light at this wavelength. In other words, if we find a counterpart within 1 arcsec that is also bright in the *g* band, we assume that it is a line-of-sight interloper, and remove the match from our sample. This criteria removes the matches to C1, C11, C20, C23, and N3. For the LAEs, this criteria removes LAE1. A galaxy 0.4 arcsec east of LAE4 is also detected in the *g* band, but we see that in the *r* and *i* bands an extension appears 0.4 arcsec to the north of this source, which our *HST* data resolves as a second galaxy. Since the eastern galaxy is detected in the *g* band but the northern one is not, we only call the northern galaxy a match to LAE4.

The Gemini-detected source near C1 (bright in the *g* band and removed from our sample) was confirmed to be a foreground $z = 2.54$ galaxy by Rotermund et al. (2021) using spectroscopy with the VLT, validating our submm-matching criteria. However, the observed [OIII] line strength suggests a stellar mass much smaller than what the IRAC flux densities (2.6 and $2.9 \mu\text{Jy}$ at 3.6 and $4.5 \mu\text{m}$, respectively)

² <https://irsa.ipac.caltech.edu/data/SPITZER/docs/irac/calibrationfiles/psfprf/>

³ <https://irsa.ipac.caltech.edu/data/SPITZER/docs/irac/iracinstrumenthandbook/1/>

would imply. Quantitatively, [Rotermund et al. \(2021\)](#) place an upper limit on the stellar mass of the foreground galaxy of $< 1.6 \times 10^9 M_{\odot}$ based on an [OIII] linewidth of 53 km s^{-1} . [Zhu et al. \(2010\)](#) propose a scaling relation between stellar mass and IRAC continuum flux densities using $g-r$ colours as a proxy for star-formation history, which we use to place an upper limit to the contribution of the measured IRAC flux density from this foreground galaxy. We measure a colour of $g-r=0.10$, corresponding to upper limits of $\nu L_{\nu} < 7.2 \times 10^8 L_{\odot}$ and $\nu L_{\nu} < 5.0 \times 10^8 L_{\odot}$ at 3.6 and $4.5 \mu\text{m}$, respectively, or $S_{3.6} < 0.06 \mu\text{Jy}$ and $S_{4.5} < 0.05 \mu\text{Jy}$. Thus, since this foreground galaxy likely contributes less than 2 per cent to the measured IRAC flux density at the position of C1, we assign all of the measured IRAC flux density to C1.

Lastly, we look by eye for consistent matches across all the data and make sure sources are not double-matched. C3, C12, C13, C16, C21, C22, and C23 are very close to C6, which is clearly the dominant galaxy in the core of the protocluster at the wavelengths covered by *HST*. In the IRAC imaging, C6 and these seven sources are blended within a single beam, yet we expect that nearly all of the measured flux density can be attributed to only C6, as it is > 25 times brighter than its surrounding galaxies in the *HST* imaging. We thus assign all of the flux density within a larger 1.5 arcsec region to C6, while providing upper limits for the nearby galaxies.

In Appendix A, Fig. A1, we show the resulting positional differences between our matching criteria outlined above and the ALMA positions given in [Hill et al. \(2020\)](#), defined as the ALMA position minus the optical/infrared position. We find counterparts in at least one image to 21/29 ALMA-identified galaxies, as well as the single LBG, and 4/6 LAEs. Four galaxies are found to have two counterparts in our F110W image, three have two counterparts in our F160W image, and one has three counterparts in our F110W image. In Fig. A1 we show the mean offset found in each band surrounded by a circle whose semi-major and semi-minor axes are equal to the standard deviations of the offsets in each direction. We find a slight offset in the negative x direction of $\Delta\text{RA} \approx -0.1$ arcsec (consistent across all wavebands, since the astrometry has been tied to a single frame); this could mean that there is a slight mismatch between the *HST* astrometry and the ALMA astrometry, but an adjustment of this size would have no effect on our results.

We investigate the purity of our source matches by running our matching algorithm on random locations within each map, allowing us to calculate a false positive rate by taking the ratio of the matches to the number of random locations tested. Using 1000 random locations, we find false positive rates of 0.08, 0.06, 0.23, 0.20, and 0.12 for the r , i , F110W, F160W, and K_s bands, respectively. For reference, our detection rates are 0.28, 0.30, 0.55, 0.43, and 0.23 for the same bands, which are factors of 2–5 higher than the false positive rates. We note that these values are upper limits to the true false positive rates, since we are requiring an optical/infrared-detected galaxy to be less than 1 arcsec from a submm source (i.e. an ALMA-detected galaxy), which is much less common than a match between two optical/infrared-detected galaxies.

For cases where we found no counterpart match, we estimate upper limits by calculating the mean flux density measurement uncertainty within a given band. We also add the local background to these non-detection upper limits, calculated within a 3 pixel-diameter circular region centred on the source. This takes into account the fact that C1 is blocked by a foreground galaxy in the GMOS and *HST* imaging (see [Rotermund et al. \(2021\)](#)), so the only upper limit we can place is that it must be fainter than the interloping foreground galaxy. This is also necessary in the IRAC imaging where confusion and source blending is a reason for many non-detections around galaxy C6. In

Table 1 we provide the resulting flux densities and upper limits for each source, and in Appendix B we show 12×12 arcsec cutouts of each source at each wavelength. We note that there are known bad pixels in our *HST* data near C21 (in both the F110W and F160W filters as it is a property of the WFC3 detector), but they are outside of the aperture used to measure the flux density of this source.

We compare our resulting optical measurements to the flux densities reported in [Rotermund et al. \(2021\)](#), who used slightly different apertures (a fixed diameter of 1.6 arcsec for the g , r , and i images, and FLUX_AUTO for the K_s image) and source-extractor parameters. We find that we do not detect C2 in the K_s band, nor C6 in the i band, but that we detect sources C2 and C14 in the r image, and C2 and C14 in the i image. In terms of the overlapping detections, we find good agreement between the flux density measurements. In the IRAC infrared imaging, we identify counterparts to all the galaxies in [Rotermund et al. \(2021\)](#), except C3 and C13 that are blended with C6, which is expected because the data used here are significantly deeper. Upon comparing the flux density measurements, we find that the measurements reported in [Rotermund et al. \(2021\)](#) are systematically larger than those reported here, by average factors of 1.7 and 2.1 at 3.6 and $4.5 \mu\text{m}$, respectively. This is also expected, since [Rotermund et al. \(2021\)](#) did not attempt to deblend the IRAC sources while here we did, meaning that the flux inside their fixed apertures should be larger on average due to surrounding source leakage.

3.3.1 Galaxy N3

In Fig. B1 we see that the centroid of N3 lies right on top of a bright and fully resolved spiral galaxy. N3 was initially identified by [Hill et al. \(2020\)](#) using ALMA in Band 3 through the detection of a CO line at 86.502 GHz, consistent with the frequencies of the CO lines detected in the other protocluster galaxies, and it was assumed that the CO transition was 4–3, placing the redshift at 4.3. However, the coincident position of the CO emission with a resolved spiral galaxy could mean that the CO emission observed is actually from another transition at lower redshift. While an alternative explanation is that there is a genuine protocluster galaxy responsible for the CO emission behind this nearby spiral galaxy, here we investigate the photometric redshift of the spiral galaxy to see if it could in fact emit a CO line at the frequency where a line was observed.

To do this, we used all of our available photometry (Table 1 plus the photometry in [Hill et al. \(2020\)](#)) to estimate a photometric redshift using CIGALE (further details about the implementation of CIGALE can be found in the next section). The resulting photometric redshift is found to be 1.7 ± 0.3 ; the only CO transition consistent with this redshift is the 2–1 transition at 230.538 GHz, which would make the spectroscopic redshift of N3 1.665. Since this redshift matches the photometric redshift quite well, for the remainder of this paper we take this galaxy to be a foreground source at $z = 1.665$ and remove it from the subsequent analyses.

3.3.2 Submm sources with no line detection

Three galaxies were found in our ALMA observations of SPT2349–56 through their continuum only (designated NL in [Hill et al. \(2020\)](#)), making them potential line-of-sight interlopers. In order to verify this hypothesis, we ran CIGALE on the complete set of photometry available for these galaxies (Table 1, and the photometry provided in [Hill et al. \(2020\)](#)) in order to estimate photometric redshifts. For NL1, we found a photometric redshift of 4.3 ± 0.7 ; while this is consistent with the redshift of SPT2349–56, we do not include

Table 1. Gemini GMOS and FLAMINGOS-2, *HST* WFC3, and *Spitzer*-IRAC flux density measurements for all SPT2349–56 galaxies. The names are the same as in Hill et al. (2020), while the names from Miller et al. (2018) are given in brackets for reference. Upper limits are 1σ . Here ellipses indicate where data are not available for a given source.

Name	$S_{0.48}^a$ [μJy]	$S_{0.63}^a$ [μJy]	$S_{0.78}^a$ [μJy]	$S_{1.1}^b$ [μJy]	$S_{1.5}^b$ [μJy]	$S_{2.1}^c$ [μJy]	$S_{3.6}^d$ [μJy]	$S_{4.5}^d$ [μJy]
C1 (A)	<0.032	<0.043	<0.045	<0.057	<0.103	<0.19	2.6±0.3	2.9±0.3
C2 (J)	<0.010	0.071±0.013	0.183±0.020	0.295±0.009	0.381±0.020	<0.25	2.7±0.4	3.2±0.3
C3 (B)	<0.006	<0.006	<0.013	<0.034	<0.055	<0.26	<5.4	<5.6
C4 (D)	<0.002	<0.014	<0.019	<0.028	<0.052	<0.17	1.1±0.3	1.1±0.3
C5 (F)	<0.003	<0.003	<0.019	<0.031	<0.060	<0.22	0.9±0.3	1.0±0.3
C6 (C)	<0.006	0.061±0.011	<0.014	0.362±0.006	1.601±0.012	4.78±0.28	9.8±0.4	9.8±0.3
C7 (K)	<0.006	<0.009	<0.012	0.082±0.010	0.196±0.019	<0.10	2.1±0.3	2.2±0.3
C8 (E)	<0.006	0.024±0.008	0.146±0.020	0.261±0.014	0.242±0.015	1.37±0.34	3.9±0.4	4.2±0.3
C9 (I)	<0.006	<0.006	<0.014	<0.034	<0.054	<0.44	0.9±0.3	1.3±0.3
C10 (H)	<0.005	<0.006	<0.022	0.037±0.004	<0.060	0.51±0.18	0.7±0.3	0.7±0.3
C11 (L)	<0.013	<0.001	<0.017	<0.030	<0.054	<0.31	<1.2	<1.3
C12	<0.007	<0.019	<0.022	<0.034	<0.064	<0.22	<3.8	<4.0
C13 (G)	<0.007	<0.013	<0.024	0.028±0.004	<0.055	<0.57	<4.5	<4.3
C14 (N)	<0.012	0.037±0.008	0.051±0.011	0.164±0.013	0.167±0.015	0.45±0.13	2.1±0.3	1.8±0.3
C15	<0.011	<0.015	0.076±0.021	0.147±0.009	0.213±0.018	<0.27	1.3±0.3	1.1±0.3
C16	<0.013	<0.010	<0.021	<0.035	<0.063	<0.21	<3.0	<2.7
C17 (M)	<0.009	0.120±0.012	0.317±0.025	0.371±0.009	0.551±0.020	0.99±0.19	1.6±0.5	1.2±0.4
C18	<0.012	<0.017	<0.011	0.240±0.010	0.223±0.017	<0.17	<0.7	<0.8
C19	<0.006	<0.007	<0.022	<0.032	<0.062	<0.16	<0.9	<1.0
C20	<0.016	<0.010	<0.021	<0.028	<0.061	<0.23	<1.7	<1.8
C21	<0.013	<0.027	0.351±0.016	0.373±0.009	0.343±0.014	<0.32	1.3±0.4	1.1±0.4
C22	<0.011	<0.006	<0.012	<0.030	<0.055	<0.37	<1.0	<1.0
C23	<0.013	<0.016	<0.024	<0.034	<0.051	<0.19	<1.4	<1.3
NL1	<0.005	<0.012	<0.021	<0.028	<0.058	<0.30	0.9±0.3	1.6±0.3
NL3	0.230±0.012	0.415±0.019	0.542±0.033	1.628±0.018	3.308±0.029	5.15±0.36	8.8±0.4	10.4±0.3
N1	<0.009	<0.006	<0.015	0.115±0.007	0.199±0.017	...	2.2±0.3	3.0±0.3
N2	<0.009	<0.003	0.112±0.019	0.094±0.007	0.093±0.014	...	1.0±0.3	0.7±0.3
N3	1.176±0.018	1.561±0.027	1.924±0.039	5.644±0.027	8.289±0.044	...	18.8±0.4	22.3±0.4
NL2	0.061±0.006	0.072±0.009	0.180±0.016	0.337±0.012	0.442±0.018	...	1.9±0.4	1.7±0.3
SPIREc1	13.0±0.3	19.4±0.3
SPIREc2	<0.8	0.7±0.3
SPIREc3	4.9±0.3	6.8±0.3
LBG3	<0.011	0.077±0.011	0.437±0.024	0.251±0.014	0.329±0.020	<0.36	<1.1	<1.1
LAE1	<0.031	<0.040	<0.056	<0.052	<0.088	<0.37	<0.8	<0.7
LAE2	<0.007	<0.005	<0.026	<0.032	<0.047	<0.31	<1.0	<0.9
LAE3	<0.005	0.054±0.011	<0.016	0.050±0.005	<0.061	<0.12	<0.3	<0.3
LAE4	<0.021	<0.028	<0.043	0.044±0.006	0.066±0.008	0.53±0.17	<0.5	<0.4
LAE5	<0.010	0.107±0.010	0.057±0.011	0.078±0.006	0.089±0.009	...	<0.4	<0.3
LAE6	<0.013	<0.006	<0.010	0.030±0.004	<0.057	...	<0.5	<0.5
LAE7	<0.008	<0.006	<0.013	0.052±0.007	<0.052	...	<0.5	<0.4

^aGemini GMOS continuum flux densities at 0.48 μm (the g band), 0.63 μm (the r band), and 0.78 μm (the i band).

^b*HST*-WFC3 continuum flux densities at 1.1 μm (the F110W filter) and 1.5 μm (the F160W filter).

^cGemini FLAMINGOS-2 continuum flux densities at 2.1 μm (the K_s band).

^d*Spitzer* IRAC continuum flux densities at 3.6 μm (ch1) and 4.5 μm (ch2).

it in any subsequent analyses because the uncertainties are still large. Further follow-up will be needed to confirm the membership of this source. For the remaining two galaxies, NL2 has a photometric redshift of 2.7 ± 0.7 , and for NL3 the photometric redshift is 2.2 ± 0.5 , so these are indeed most likely galaxies in the foreground of the protocluster.

3.4 SED fitting

To estimate the physical properties of the galaxies belonging to the SPT2349–56 protocluster system, we used CIGALE (Burgarella et al. 2005; Noll et al. 2009; Boquien et al. 2019) to fit SEDs to the available photometry. This includes all of the photometric data provided in

Table 1, as well as the 850 μm , 1.1 mm, and 3.2 mm photometry from Hill et al. (2020). We also input 1σ upper limits to the photometry for non-detections, and include *Herschel*-SPIRE 250, 350, and 500 μm constraints from Miller et al. (2018).

CIGALE models a galaxy’s rest-frame optical and ultra-violet spectrum using simple stellar population models with variable star-formation histories, including nebular emission lines, and incorporates a flexible dust attenuation curve that allows the slope and strength of the ultraviolet bump to vary. The thermal dust emission is modeled assuming a power-law dust temperature distribution, and energy balance is imposed such that the energy absorbed by dust, primarily at rest-frame ultraviolet and optical wavelengths, is approximately equal to that re-radiated in the infrared, allowing for discrepancies due to non-isotropy from the ultraviolet and optical emission. In our fits we assumed a delayed star-formation history with a single exponential timescale. The SFR as a function of time is parameterized by

$$\text{SFR} \propto \frac{1}{\tau_{\text{SFH}}^2} e^{t/\tau_{\text{SFH}}}, \quad (2)$$

where τ_{SFH} is the timescale, effectively the time at which the star-formation peaks, and a free parameter of the model. The total current stellar mass, M_* , in this model is found by varying the duration of the star-formation, assuming a Chabrier initial mass function (IMF; Chabrier 2003) with solar metallicity. We note that the assumed star-formation history can have an effect on the resulting stellar mass (up to a factor of 2, see Michałowski et al. 2012), although we did not find a large variation in the results after testing several of the available models. Another free parameter is the dust attenuation, given by the amount of extinction present in the V band in magnitudes, A_V , which we model using the Calzetti et al. (2000) attenuation curve with a variable power-law slope. The dust is modeled following Draine et al. (2014), where the dust is separated into a diffuse component heated by the interstellar radiation field, and a compact component linked to star-forming regions and heated by a variable radiation field. The total dust mass sets the overall normalization.

To obtain posterior distributions for the parameters in the fits, CIGALE generates a grid of possible SEDs, and calculates χ^2 for each SED. These χ^2 values are then translated to a global likelihood function, assuming the likelihood is proportional to $e^{-\chi^2/2}$. Marginalized posterior distributions are then calculated for the free parameters, and CIGALE returns the mean values and standard deviations of these distributions. The resulting stellar masses are given in Table 2, and the best-fit SEDs are shown in Appendix C. Where parameter uncertainties overlap with 0, we provide 1σ upper limits. For galaxies C12, C16, C20, C22, C23, LAE1, and LAE2, only upper limits are available for their photometry across all wavelengths (both submm and optical/infrared), so we do not attempt to fit SEDs and derived stellar masses.

We find stellar masses ranging from about 10^{10} – $10^{11} M_{\odot}$. For reference, we compare these stellar masses to those estimated by Rotermund et al. (2021), who used the same SED-fitting code and procedure but with less photometric coverage. We find that the masses from Rotermund et al. (2021) are larger than the masses estimated here by the same factors as their reported IRAC flux densities discussed in the previous section, which is expected as a deblending algorithm was not used in their work. As a final check, from the fits we calculated the SFR averaged over the past 100 Myrs, and compared these to the SFRs estimated from fitting modified blackbody functions to the far-infrared photometry in Hill et al. (2020); the two estimates are in good agreement considering the simple SFH

adopted by our SED models, with a median ratio of far-infrared SFR-to-CIGALE SFR of 1.1.

3.5 Rest-frame ultraviolet profile fitting

We next investigate the morphological profiles of some of the brighter galaxies detected in our F160W image (observed-frame 1.54 μm , or 290 nm in the rest-frame). We are interested in the characteristic sizes of the unobscured stellar emission, compared to their sizes as seen in the submm, where the emission is due to dust and star-formation, thus we choose the longest wavelength covered by our *HST* data. However, we note that 290 nm is still in the ultraviolet, where most of the flux density is due to young O and B stars.

We created 2 arcsec \times 2 arcsec cutouts around each protocluster member galaxy in our sample (except for NL3 and LAE1, which we include in this size analysis even though they are excluded from our protocluster galaxy analysis, where we made 3 arcsec \times 3 arcsec cutouts), and fit elliptical 2D Sérsic profiles (allowing the Sérsic index to vary) convolved with the *HST* beam to the sources with optical counterparts containing pixels greater than 5 times the background rms; the relevant sources are C2, C6, C8, C17, N1, and LBG3. We note that while C21 reaches >5 times the background rms as well, we remove it from this analysis due to the nearby bad pixels. We use the *HST* F160W PSF available from the Space Telescope Science Institute (STScI) instrumentation website,⁴ taking the PSF corresponding to the response from a point source illuminating the centre of a pixel. The available PSF model supersamples the pixel plate scale of 0.13 arcsec by a factor of 4, and we regrid the PSF model to match the pixel scale of our F160W imaging. This PSF is convolved with each galaxy’s profile to produce our models; this is the same modelling technique used in popular profile-fitting packages such as *galfit* (Peng et al. 2002, 2010). The resulting beam-deconvolved half-light radii (the length of the semi-major axes of an ellipse containing half the total flux density) are provided in Table 2, and our models are shown in Appendix D. We find half-light radii ranging from 0.85 kpc to 2.05 kpc, and Sérsic indices ranging from 0.3 to 2.6.

Since most of our *HST* detections are faint and cannot be fit on an individual basis, we performed a stacking analysis in order to evaluate the average rest-frame ultraviolet profile. As we ultimately want to compare this to the average submm profile, we focused on the subset of our sample with corresponding high-resolution ALMA data at 850 μm (as detailed in the section below). These include all of the galaxies in the core region of SPT2349–56 (C1–C23). We removed C1 from the analysis as the *HST* detection at its position is a foreground galaxy, and we removed C21 due to the nearby bad pixels. We also excluded C6 since it is clearly an outlier in terms of brightness at this wavelength, and this galaxy will be subject to its own separate analysis.

The position at which to centre each cutout for the stack is crucial. In order to obtain an unbiased image of the rest-frame ultraviolet light of submm sources, one should centre the rest-frame ultraviolet images on the positions of the submm sources. However, in practice there are physical offsets between rest-frame ultraviolet light and submm light, so this may not be the best choice. Here we choose to centre the cutouts at the position of the peak *HST* counterpart for cases where one is detected, and otherwise at the position of the peak pixel in each galaxy’s average [CII] map, which provides the highest positional accuracy owing to the brightness of the line (see Hill et al.

⁴ <https://www.stsci.edu/HST/instrumentation/wfc3/data-analysis/psf>

Table 2. Best-fit properties of the galaxies in our sample. Here dashes indicate non-detections, while ellipses indicate where data are not available for a given source.

Name	$R_{1/2,UV}^a$ [kpc]	$R_{1/2,CII}^b$ [kpc]	M_*^c [$10^{10} M_\odot$]	μ_{gas}^d	τ_{dep}^e [Gyr]
C1 (A)	–	2.91±0.02	22.2±21.3	0.34±0.32	0.074±0.018
C2 (J)	1.18±0.45	2.56±0.03	4.5±1.9	0.46±0.21	0.100±0.026
C3 (B)	–	1.32±0.04	<112.6	–	0.046±0.011
C4 (D)	–	1.90±0.01	<24.0	–	0.053±0.013
C5 (F)	–	2.22±0.02	<21.8	–	0.024±0.007
C6 (C)	0.47±0.05	1.30±0.04	10.9±3.4	0.31±0.10	0.058±0.014
C7 (K)	–	2.04±0.03	3.0±1.9	0.33±0.22	0.120±0.033
C8 (E)	1.45±0.58	1.21±0.03	11.1±4.1	0.21±0.08	0.051±0.013
C9 (I)	–	1.42±0.03	<18.0	–	0.049±0.014
C10 (H)	–	1.14±0.03	1.5±1.1	0.77±0.57	0.060±0.016
C11 (L)	–	1.40±0.04	<6.7	–	0.084±0.043
C12	–	–	–	–	–
C13 (G)	–	1.00±0.09	7.5±6.8	0.11±0.10	0.043±0.011
C14 (N)	–	0.37±0.11	3.4±1.3	0.06±0.04	0.046±0.030
C15	–	–	1.2±0.6	–	–
C16	–	–	–	–	–
C17 (M)	1.76±0.73	2.04±0.08	1.2±0.5	–	–
C18	–	–	0.6±0.4	–	–
C19	–	–	<4.8	–	–
C20	–	–	–	–	–
C21	–	–	1.0±0.5	–	–
C22	–	–	–	–	–
C23	–	–	–	–	–
NL1	–	–	–	–	–
NL3	–	–	–	–	–
N1	1.05±0.63	...	4.7±1.7	2.56±0.96	0.075±0.019
N2	–	...	1.0±0.6	4.84±2.68	0.067±0.022
N3	–	...	–	–	–
NL2	–	...	–	–	–
SPIREc1	39.3±34.0	0.17±0.15	–
SPIREc2	<4.5	–	–
SPIREc3	12.3±11.0	0.20±0.18	–
LBG3	1.09±0.17	...	0.6±0.4	–	–
LAE1	–	...	–	–	–
LAE2	–	...	–	–	–
LAE3	–	...	<0.1	–	–
LAE4	–	...	0.5±0.4	–	–
LAE5	–	...	0.1±0.1	–	–
LAE6	–	...	<0.8	–	–
LAE7	–	...	0.4±0.3	–	–

^aBest-fit rest-frame ultraviolet half-light radius, obtained by fitting Sérsic profiles to all sources detected in our *HST* F160W imaging with sufficient SNR (see Section 3.5).

^bBest-fit [CII] profile half-light radius, obtained by fitting Sérsic profiles to [CII]-detected sources after staking all channels containing line emission (see Hill et al. 2020 and Section 3.6).

^cBest-fit stellar mass from fitting SEDs using the photometry in Table 1 and from Hill et al. (2020), obtained using CIGALE.

^dMolecular gas-to-stellar mass ratio, $\mu_{gas} = M_{gas} / M_*$, with M_{gas} values taken from Hill et al. (2020).

^eDepletion timescale, $\tau_{dep} = M_{gas} / SFR$, with M_{gas} and SFR values taken from Hill et al. (2020).

2020). We also masked pixels above 25σ to remove bright nearby objects not associated with the galaxies in the stack.

The resulting image is shown in Fig. 2. Following the same steps as above, we fit a Sérsic profile to the stack, and our best-fit model and residual are shown alongside the data. We find a half-light radius of 1.24 ± 0.29 kpc and a Sérsic index of 0.75 ± 0.30 , consistent with the sizes found for the individual galaxies. Similarly, we find an axis ratio of 1.0 ± 0.3 , as expected for stacking random orientation angles.

3.6 [CII] sizes

Following the method outlined above and in Hill et al. (2020), we also fit Sérsic profiles to cutouts of each galaxy’s extended [CII] emission. Line emission channels were determined from lower-resolution, deeper ALMA data by fitting Gaussian profiles to the spectra, from which we averaged the high-resolution channels from -3σ to 3σ (where σ is the standard deviation of the best-fitting linewidth), or for cases where two Gaussians was a better fit, from $-3\sigma_L$ to $+3\sigma_R$, where σ_L and σ_R are from the left and right Gaussian fits, respectively. $2 \text{ arcsec} \times 2 \text{ arcsec}$ cutouts were made around each source, and models were fit to sources with pixels detected above 5 times the background rms by convolving a Sérsic profile with the data’s synthesized beam. We allowed the position, position angle, ellipticity, half-light radius, and Sérsic index to vary in our fits. The results are provided alongside our ultraviolet profile fits in Table 2, and the models are shown in Appendix E. We find half-light radii in the range of 0.48 to 2.91 kpc, and Sérsic indices in the range of 0.34 to 2.01.

We next determined the average submm-continuum profile following the same stacking procedure done for our *HST* data. High resolution continuum maps were already presented in Hill et al. (2020), obtained by stacking the line-free channels. We selected the same galaxies as in the *HST* analysis (i.e. each core galaxy except for C1, C6, and C20), and centred the cutouts on the peak of the average [CII] map. We then fit a Sérsic profile to the stack, and found a half-light radius of 1.18 ± 0.01 kpc with a Sérsic index of 1.22 ± 0.03 . Similarly, we find an axis ratio of 0.9 ± 0.1 , overlapping with 1 as expected for stacking random orientation angles. The stack, along with the fit, is shown in Fig. 2.

4 RESULTS

4.1 The galaxy main sequence

A primary quantity of interest is the galaxy main-sequence (MS), which is the SFR of a galaxy as a function of its stellar mass (e.g. Elbaz et al. 2011), and is commonly used to identify starbursts and quenched galaxies and therefore can place these protocluster galaxies in the context of galaxy evolution. Recently, Rotermund et al. (2021) estimated stellar masses for 14 member galaxies of SPT2349–56 using SED fits to Gemini and *Spitzer* photometry, albeit shallower than presented here, and compared these to the $z = 4.3$ MS. With our improved optical, infrared, and mm-wavelength coverage, as well as a more detailed IRAC deblending algorithm and an expanded catalogue of protocluster galaxies, we are able to expand on this work in much greater detail.

In Fig. 3 (top left panel) we show the stellar masses derived in this paper as a function of SFR. The SFRs shown here were derived in Hill et al. (2020) by fitting modified blackbody distributions to the far-infrared photometry observed by ALMA. In the fits, β was fixed to 2, and the dust temperature, T_d , was fixed to 39.6 K (the temperature consistent with the mean ratio of the measured 850 μm

flux density to the measured 3.2 mm flux density of the sample). In Hill et al. (2020) the best-fit SEDs were then integrated between 42 and 500 μm to obtain far-infrared luminosities, but here we integrate from 8 to 1000 μm to obtain more complete infrared luminosities in order to be consistent with comparison samples; this increases the luminosities by a factor of 1.17. These values were converted to SFRs using a factor of $0.95 \times 10^{10} \text{ M}_\odot \text{ yr}^{-1} \text{ L}_\odot^{-1}$ (from Kennicutt 1998, modified for a Chabrier initial mass function; see Chabrier 2003). The core galaxies of SPT2349–56 (defined as those lying within a 90 kpc-radius of the far-infrared luminosity-weighted centre, where the primary-beam response of the ALMA observation used to find protocluster members falls to 0.5, see Hill et al. 2020) are of interest because simulations predict that they will merge into a BCG on a timescale of a few hundred Myrs (Rennehan et al. 2020). We have highlighted these galaxies in black in Fig. 3. We also show the LAEs and LBGs of this sample as squares in order to distinguish them from the primary submm-selected galaxies making up the core of this protocluster.

For comparison, we also show in Fig. 3 the galaxies found in a similar star-forming protocluster, the Distant Red Core (DRC; Oteo et al. 2018; Long et al. 2020), found at redshift 4. For these protocluster galaxies, the stellar masses were also obtained through optical and infrared SED fitting, while infrared luminosities were derived by scaling the mean template from the ALMA follow-up programme of the LABOCA ECDF-S Submillimetre Survey (ALESS; Simpson et al. 2014) to match their continuum observations at 2 mm; we applied the same scale factor used in our work to obtain SFRs.

To see how these protocluster galaxies compare with field galaxies, we focus on samples of high-redshift SMGs, since the SFRs of SMGs typically exceed 100 M_\odot , which accounts for the majority of our sample. We show the $z > 3.5$ SMGs from the ALESS survey, originally selected as bright 870- μm point sources in the Extended *Chandra* Deep Field South (ECDF-S; Simpson et al. 2015), with stellar masses derived by da Cunha et al. (2015) by fitting SEDs to optical and infrared photometry, and for the SFRs we converted the infrared luminosities from Swinbank et al. (2014) (obtained by fitting a modified blackbody SED to the available far-infrared photometry) to SFRs using a conversion factor of $0.95 \times 10^{-10} \text{ M}_\odot \text{ yr}^{-1} \text{ L}_\odot^{-1}$. We also show a sample of field SMGs around $z = 4.4$ from Scoville et al. (2016) that were initially selected in a representative fashion from the COSMOS field; for these galaxies, stellar masses were also estimated from SED fits to optical and infrared photometry, and the SFRs were derived from rest-frame ultraviolet and infrared continuum measurements, adopting a factor of 2 uncertainty as recommended in the paper. While we cannot entirely rule out the possibility that some of these field galaxies are in fact in protocluster environments, none of them are in known protoclusters, nor are any of them located in environments as overdense in the submm as SPT2349–56 or the DRC.

Next, we show galaxies from the ALPINE survey (Le Fèvre et al. 2020; Béthermin et al. 2020; Faisst et al. 2020) between $z = 4.4$ and $z = 4.7$; for the ALPINE galaxies, stellar masses were obtained by fitting SEDs to optical and infrared photometry, and we have taken their infrared luminosities (scaled from 850 μm continuum detections assuming a model template of $z \approx 4$ MS galaxies) and converted these to SFRs using the same factor of $0.95 \times 10^{10} \text{ M}_\odot \text{ yr}^{-1} \text{ L}_\odot^{-1}$. We then show the best-fit $z = 4.5$ MS obtained from the ALPINE survey (Khusanova et al. 2020); we note that the parameterization found by the ALPINE survey is consistent with previously-derived MS parameterizations from e.g. Speagle et al. (2014) at $z = 4.3$. For reference, we show a scatter of a factor of 2 around the MS, the intrinsic scatter proposed by Schreiber et al. (2015).

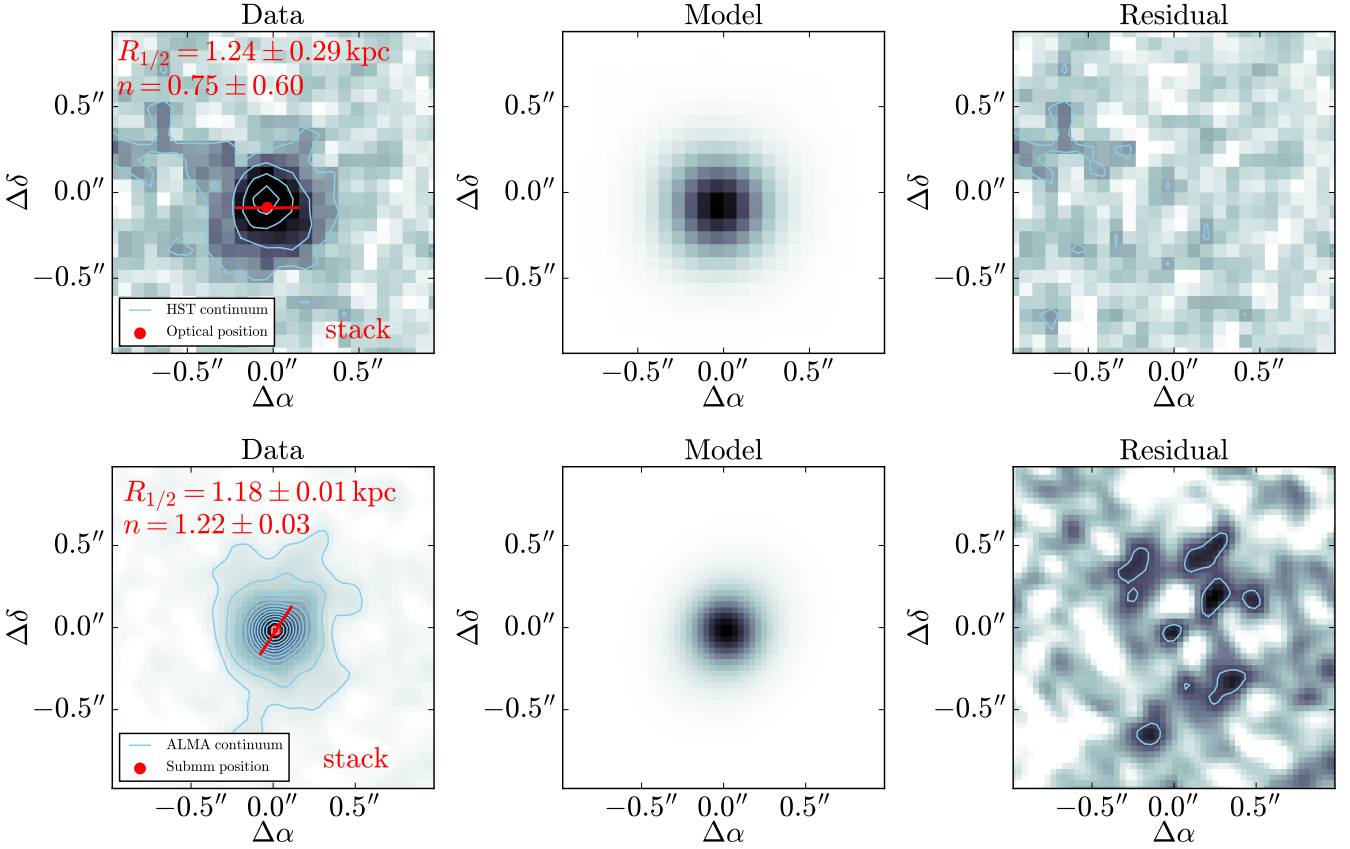


Figure 2. *Top row:* Stacked F160W image of all the core galaxies in our sample (except C1, C6, and C21; see the text for details). Contours start at 2σ and increase in steps of 4σ . The red dot indicates the position of the best-fit centre, and the red line shows the length and position angle of the best-fit half-light diameter. The middle panel shows the best-fit Sérsic profile, after convolution with the beam and the pixel window function. The residual map is shown at right, with the same contour levels as the left panel. *Bottom row:* Same as the top row, but stacking our high-resolution 850- μm ALMA continuum images. Contours again start at 2σ and increase in steps of 4σ .

We see that the galaxies in SPT2349–56 follow the $z=4.5$ MS derived by the ALPINE survey, although with considerable scatter, along with the other samples of field SMGs and the star-forming galaxies from the ALPINE survey. To investigate this in detail, in Fig. 3 (top right panel) we show the SFRs in SPT2349–56 divided by the SFRs predicted by the ALPINE MS for each galaxy’s measured stellar mass. We include the field SMGs from the samples described above, as well as the individual star-forming galaxies from the ALPINE survey.

In order to assess the difference between protocluster galaxies to field galaxies around $z=4$, we combine our sample of protocluster galaxies with those from the DRC, and compare them to the ALESS and COSMOS SMGs. Since the SFR is log-normally distributed at a given stellar mass (e.g. Speagle et al. 2014; Schreiber et al. 2015), we compute the weighted mean and weighted standard deviation of the logarithm of the two samples; we find that the weighted mean $\log \text{SFR} / \text{SFR}_{\text{MS}}$ for the protocluster galaxies is 0.13, with a weighted standard deviation of 0.46, while for the field SMGs the weighted mean $\log \text{SFR} / \text{SFR}_{\text{MS}}$ is -0.12 , with a weighted standard deviation of 0.35. These values are plotted on Fig. 3 for reference.

We therefore find mild evidence that the protocluster galaxies in these samples have on average slightly higher SFRs than expected from the MS, although the scatter is large, and indeed the means of the protocluster galaxies and field galaxies lie within the expected population scatter of a factor of 2. A two-sample t -test performed on

the $\log \text{SFR} / \text{SFR}_{\text{MS}}$ values of each sample results in a p -value of 0.54, which can be interpreted as the probability that the means are the same. However, we emphasize that there could be large systematic errors present, owing from differences in modelling the SEDs used to fit the available photometry to obtain stellar masses; for example, different functional forms for the SFH can be assumed, and there are numerous models of dust extinction available.

4.2 Molecular gas-to-stellar mass ratios

Another mass measurement available for the protocluster galaxies in SPT2349–56 is the molecular mass, and a useful evolutionary diagnostic is to see if the molecular gas-to-stellar mass ratio scales with the total stellar mass built-up so far. We define the molecular gas-to-stellar mass ratio as

$$\mu_{\text{gas}} = \frac{M_{\text{gas}}}{M_*}, \quad (3)$$

where M_{gas} is the molecular gas mass and M_* is the stellar mass.

We use the molecular gas masses derived in Hill et al. (2020). Briefly, the CO(4–3) transition was observed by ALMA, and line strengths were measured for sources where the line was detected. The CO(4–3) line strength was converted to a CO(1–0) line strength using a factor of 0.60 (the mean line strength ratio of the SPT-SMG sample from Spilker et al. 2014), and then this was converted to a molecular

gas mass using a conversion factor of $\alpha_{\text{CO}} = 1 M_{\odot}/(\text{K km s}^{-1} \text{pc}^2)$, similar to other studies of SMGs (see e.g., [Aravena et al. 2016](#); [Bothwell et al. 2017](#)). The resulting molecular gas-to-stellar mass ratios are given in Table 2; we find values ranging from about 0.04 to 5. Interestingly, since our stellar masses are lower than the values provided by [Rotermund et al. \(2021\)](#), we estimate larger values of μ_{gas} , which is in better agreement with the simulations analyzed by [Lim et al. \(2021\)](#).

Figure 3 (bottom left panel) shows our molecular gas-to-stellar mass ratios as a function of stellar mass (with the core galaxies again highlighted), compared with the galaxies from the DRC ([Oteo et al. 2018](#); [Long et al. 2020](#)), where we have converted their CO(6–5) line intensities to molecular gas masses using an $L'_{(6-5)}/L'_{(1-0)}$ factor of 0.46 (the mean ratio found for the SPT-SMG sample, see [Spilker et al. 2014](#)) and an α_{CO} of $1 M_{\odot}/(\text{K km s}^{-1} \text{pc}^2)$ (the same scale factor used for our sample).

To compare protocluster galaxies with field galaxies around $z = 4$, we require a sample with molecular gas masses estimated with similar CO transition tracers. A recent CO survey of SMGs selected from the COSMOS field, the UDS field, and the ALESS sample spanning $z = 1-5$ was carried out by [Birkin et al. \(2021\)](#), and we have selected the galaxies from this survey with $z > 3.5$ to use as a field comparison here. Half of the galaxies were selected to have the brightest $870 \mu\text{m}$ continuum flux densities, while the other half were selected as having secure spectroscopic redshifts. CO($J_{\text{up}}-J_{\text{up}} - 1$) line emission detections ranged from $J_{\text{up}} = 2-5$, and we use the mean line ratios of the sample to convert these line intensities to the $J_{\text{up}} = 1$ line (for reference, the mean $J_{\text{up}} = 4$ ratio was found to be 0.32, compared to 0.60 used for the SPT2349–56 galaxies). We then adopt an α_{CO} of $1 M_{\odot}/(\text{K km s}^{-1} \text{pc}^2)$ for this reference sample. Stellar masses are provided for each source, derived by fitting SEDs to the extensive photometry available in these fields. For comparison with a sample of high- z galaxies that are not SMGs, we include the galaxies from the ALPINE survey here by deriving molecular gas masses from the published [CII] luminosities, following the prescription outlined in [Dessauges-Zavadsky et al. \(2020\)](#).

We again combine our sample of protocluster galaxies with the DRC, and compare this to the sample from [Birkin et al. \(2021\)](#). Looking at Fig. 3 (bottom left panel) we see that the molecular gas-to-stellar mass also appears log-normally distributed, so we calculate the weighted mean and weighted standard deviation of the logarithm of each sample. We find that the weighted mean $\log \mu_{\text{gas}}$ of protocluster galaxies is -0.45 , with a weighted standard deviation of 0.54, while for the field galaxies we find a weighted mean $\log \mu_{\text{gas}}$ of -0.05 , with a weighted standard deviation of 0.72 (see Fig. 3). Thus we find that the protocluster galaxies are more gas poor than field galaxies at this redshift, although the scatter between the two groups contains significant overlap. For reference, the star-forming galaxies from the ALPINE survey have larger molecular gas-to-stellar mass ratios than all of the SMGs in this comparison. A similar two-sample t -test on the $\log \mu_{\text{gas}}$ values results in a p -value of 0.04, providing further evidence for a difference in the means of the samples.

4.3 Depletion timescales

A similar quantity of interest is the gas depletion timescale, which is a measure of the amount of time required to convert all of the available mass in gas into mass in stars if the current star-formation rate were to remain constant. This quantity is defined as

$$\tau_{\text{dep}} = \frac{M_{\text{gas}}}{\text{SFR}}, \quad (4)$$

where this time M_{gas} is divided by the SFR.

In Table 2 we provide estimates of the depletion timescale for each galaxy with a measurement of molecular gas mass (via CO(4–3) line detection) and SFR (via far-infrared photometry). We find that the galaxies in SPT2349–56 have depletion timescales ranging from 0.05 to 0.1 Gyr.

In Fig. 3 (bottom right panel) we show our depletion timescales as a function of stellar mass. In order to compare with the same $z > 3.5$ field SMGs from [Birkin et al. \(2021\)](#), we take their provided far-infrared luminosities, obtained by fitting SEDs with the available photometry, and multiply them by the usual factor of $0.95 \times 10^{10} M_{\odot} \text{yr}^{-1} L_{\odot}^{-1}$. We also show the protocluster galaxies from the DRC, and we include the same ALPINE galaxies for reference to a sample of non-SMGs.

Just as with the gas fractions, we find that the depletion timescales appear on average smaller in protocluster galaxies than in field SMGs. We take the same log-normal approach to quantify this difference, finding that the weighted mean $\log(\tau_{\text{dep}} / [\text{Gyr}])$ for the protocluster galaxies (again combining SPT2349–56 and the DRC) is -1.28 , with a weighted standard deviation of 0.18, and the weighted mean $\log(\tau_{\text{dep}} / [\text{Gyr}])$ for the field galaxies from [Birkin et al. \(2021\)](#) is -0.85 , with a weighted standard deviation of 0.26 (see Fig. 3). We therefore find that the depletion timescales for protocluster galaxies are smaller than for field galaxies, as there is very little overlap between the two distributions. The resulting p -value from a two-sample t -test is 1.7×10^{-5} , thus we conclude that the means of the samples are not the same. Lastly, we find that the star-forming galaxies from the ALPINE survey have longer depletion timescales than all of the SMGs in this comparison.

4.4 The stellar mass function

Our large sample of protocluster galaxies with stellar mass estimates allows us to compute the stellar mass function of SPT2349–56 in several different ways. Of most interest is what the stellar mass function of the whole protocluster looks like in comparison to lower- z clusters. However, we know that the core galaxies in SPT2349–56 will merge into a single BCG within a few hundred megayears ([Rennehan et al. 2020](#)), so we would also like to know what the stellar mass function will look like after the merger by summing their masses.

To start, most of the galaxies in SPT2349–56 were found via their [CII] emission (23 galaxies in the core, plus one in the northern region), with the faintest galaxy having a line luminosities of $1.6 \times 10^8 L_{\odot}$ (see [Hill et al. 2020](#)). Adopting the same prescription to convert [CII] line luminosities to molecular gas masses used in the ALPINE survey ([Dessauges-Zavadsky et al. 2020](#)), we find that this translates to a molecular gas mass of about $5 \times 10^9 M_{\odot}$. For comparison, the region surrounding SPT2349–56 was uniformly observed by ALMA in Band 3, with a sensitivity to CO(4–3) emission translating to about $2 \times 10^{10} M_{\odot}$ in molecular gas mass. Next, the mean log molecular gas-to-stellar mass ratio we found after combining our sample with the galaxies from the DRC protocluster was -0.45 , or $\langle \mu_{\text{gas}} \rangle = 0.35$, albeit with considerable spread; therefore, to within an order of magnitude, we can assume that our [CII] sample is sensitive to galaxies of stellar mass down to roughly $1 \times 10^{10} M_{\odot}$. However, our sample also includes LBGs and LAEs with different selection criteria, making any completeness corrections difficult, and so below we present the number counts of our complete sample, followed by a discussion of the limitations.

Figure 4 (top panels) shows the differential and cumulative number counts of the stellar masses of all the galaxies in our sample (exclud-

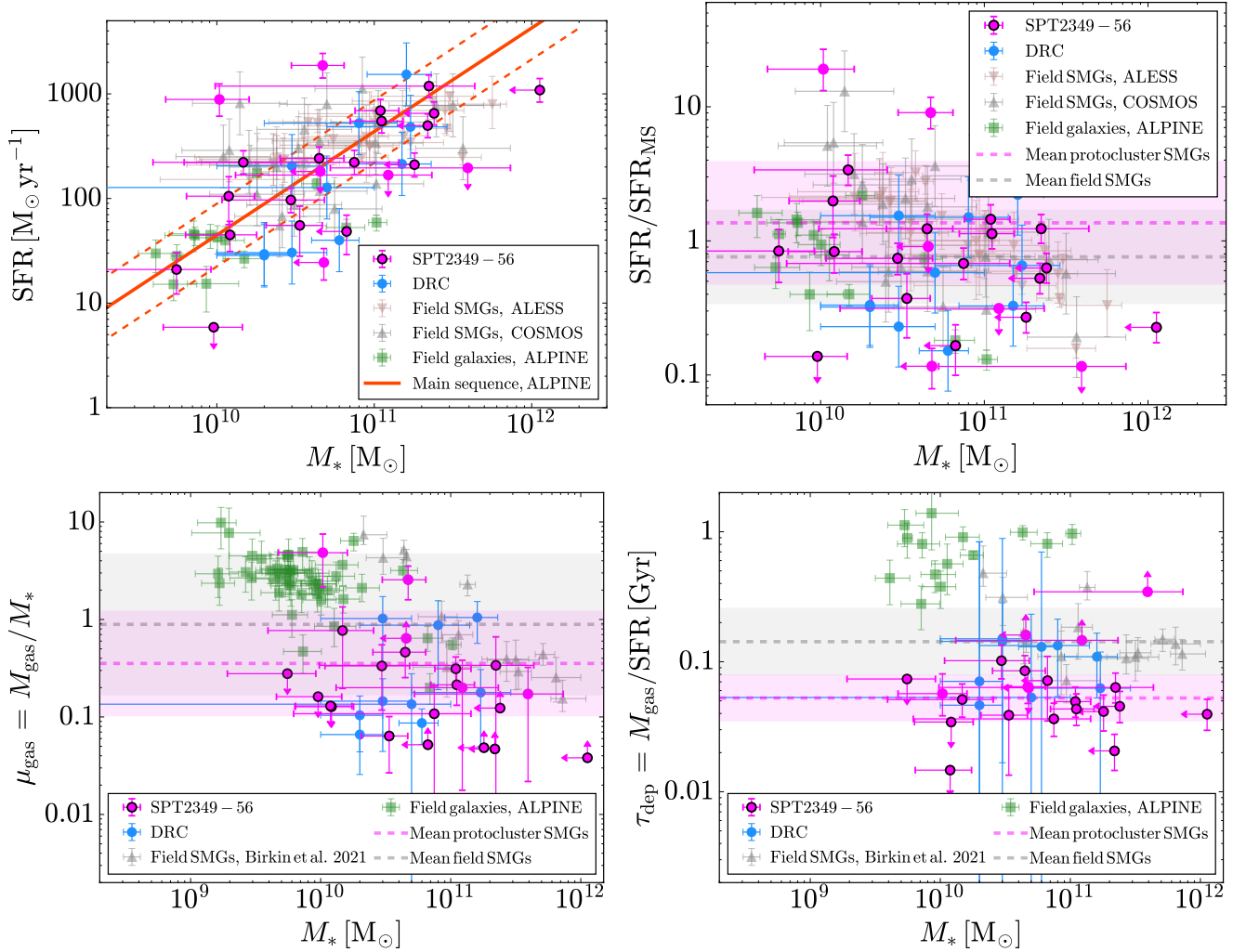


Figure 3. *Top left:* Stellar mass as a function of SFR (i.e. the galaxy main sequence) for all galaxies in the SPT2349–56 protocluster with sufficiently good photometry. The SFRs shown here were estimated in Hill et al. (2020). Galaxies highlighted in black are part of the core of the structure, defined as those lying within a radius of 90 kpc of the far-infrared luminosity-weighted centre (see Hill et al. 2020). Also shown are $z > 3.5$ SMGs from the ALESS survey (da Cunha et al. 2015), a sample of SMGs around $z = 4.4$ from the COSMOS field (Scoville et al. 2016), $z = 4.4$ – 5.9 galaxies from the ALPINE survey (B  thermin et al. 2020), and a fit of the MS at $z = 4.5$ from the ALPINE survey (Khusanova et al. 2020), including an intrinsic scatter of ± 0.3 dex proposed by Schreiber et al. (2015). We show a similar star-forming $z = 4$ protocluster known as the DRC (Long et al. 2020). *Top right:* Measured SFRs divided by the SFR expected for a given stellar mass (SFR_{MS}), assuming the MS relation from the ALPINE survey (Khusanova et al. 2020), shown for the same galaxies in the top-left panel. Since SFR is distributed log-normally for a given stellar mass, the pink horizontal line and shaded region shows the weighted mean and standard deviation of $\log \text{SFR} / \text{SFR}_{\text{MS}}$ for the protocluster galaxies, respectively (combining our sample with the galaxies from the DRC), while the grey horizontal line and shaded region shows the weighted mean and standard deviation of $\log \text{SFR} / \text{SFR}_{\text{MS}}$ for field SMGs, respectively (combining the galaxies from the ALESS and COSMOS surveys). *Bottom left:* Molecular gas-to-stellar mass fraction, μ_{gas} (Eq. 3), as a function of stellar mass, using molecular gas masses from Hill et al. (2020). Our protocluster sample is compared with the field SMGs from Birkin et al. (2021), where molecular gas masses have been derived from CO observations similar to our sample, and the DRC. We also include the galaxies from the ALPINE survey by converting their published [CII] luminosities to molecular gas masses following the prescription outlined in Dessauges-Zavadsky et al. (2020). The weighted mean and standard deviation of $\log \mu_{\text{gas}}$ for all the protocluster galaxies is shown as the horizontal pink line and shaded region, respectively, and the weighted mean and standard deviation of $\log \mu_{\text{gas}}$ for the field galaxies is shown as the horizontal grey line. *Bottom right:* Depletion timescale, τ_{dep} (Eq. 4), as a function of stellar mass, for the same galaxies shown in the top-left panel, along with the same weighted means and standard deviations of the logarithms of the subsamples as horizontal lines and shaded regions, respectively.

ing the three SPIREc sources, since they are at a large projected distance where our imaging is not complete). We have normalized our counts by the volume of a sphere of radius 360 kpc, which is the distance between the core and northern components of SPT2349–56 (see Hill et al. 2020). We note that the true normalization is highly uncertain, but in this analysis we are only interested in the shape of the mass function. We compare this protocluster stellar mass func-

tion to the stellar mass function of a typical $z \approx 1$ galaxy cluster (van der Burg et al. 2013), obtained by stacking cluster galaxies from a sample of 10 clusters (including their BCGs) within 1 Mpc of the cluster cores. We set the normalizing volume to be the volume of 10 spheres of radius 1 Mpc, and again emphasize that the absolute normalization here is uncertain but has no effect on the shape of the counts. While this reference sample contains galaxies within a

larger proper volume than probed by our ALMA data (1 Mpc versus 360 kpc), previous studies of $z < 1$ galaxy clusters have found that best-fit parameterizations of stellar mass number counts do not vary considerably when calculated within radii ranging from $0.5 R_{500}$ to $2 R_{500}$ (where R_{500} is around 1 Mpc, see [van der Burg et al. 2018](#)); the slope, α , ranges from -0.8 to -1.0 , while the characteristic mass, M^* , remains constant within the uncertainties. Therefore, we expect our conclusions would remain unchanged if the $z \approx 1$ comparison sample were limited to galaxies within 360 kpc, as with our sample. Qualitatively, we see that the shapes of the number counts are in agreement with one another for masses above $10^{10} M_{\odot}$.

Next, we compute the differential and cumulative number counts of the molecular gas masses in SPT2349–56 using the values provided in [Hill et al. \(2020\)](#) for the same galaxies in our sample. These functions are shown alongside the stellar mass function in Fig. 4 (top panels). We find that the molecular gas mass function effectively tracks the stellar mass function.

We then assess the state of the number counts after the merger of the BCG galaxies by summing the masses of all the galaxies within 90 kpc of the far-infrared luminosity-weighted centre (i.e. the region simulated by [Rennehan et al. 2020](#) where the mergers will take place), and treating this as a single point. These are shown alongside our other number counts in Fig. 4 (bottom panels) for comparison. We see that the shapes become more linear (in log-log space), and the final mass of the merged galaxies matches the masses of the largest galaxies in the $z = 1$ sample. The amplitude of our counts is also larger than the $z = 1$ cluster counts at these high-mass bins, although since the normalizations are highly uncertain, we cannot draw any conclusions from this excess.

We next fit our protocluster mass functions to functional forms using a maximum-likelihood approach (e.g., [Marshall et al. 1983](#); [Wall et al. 2008](#); [Hill et al. 2020](#)), where we minimize the negative log-likelihood of our stellar mass measurements assuming that all sources were selected from data of equal depth:

$$S = -2 \ln \mathcal{L} = -2 \sum_{i=1}^N \ln \phi(M_i) + 2V \int_{M_a}^{M_b} \phi(M) dL + C. \quad (5)$$

In this equation N is the sample size, $\phi(M)$ is the model differential stellar mass number count (in units of $M_{\odot}^{-1} \text{Mpc}^{-3}$), V is the volume of the survey, M_a and M_b are the mass limits of the sample (which we take to be between the smallest and largest masses in the sample), and C is a constant independent of the model. We investigate two models, a single power-law and a Schechter function. The single power-law has two free parameters, a normalization and a power-law index; explicitly,

$$\phi(M) = \phi^* \left(\frac{M}{M^*} \right)^{\alpha}, \quad (6)$$

where α is the slope of the power law, ϕ^* is the overall normalization, and M^* is fixed to $10^{10} M_{\odot}$ and is not a free parameter of the model. For the Schechter function, M^* is not fixed but treated as a free parameter, describing the point at which the number counts transition from a power law to an exponential:

$$\phi(M) = \phi^* \left(\frac{M}{M^*} \right)^{\alpha} e^{-M/M^*}. \quad (7)$$

We use a Markov chain Monte Carlo (MCMC) approach to minimize the log-likelihood, and calculate the odds ratio between a single power-law fit and a Schechter fit (simply $\mathcal{L}_{\text{Schechter}}/\mathcal{L}_{\text{Power-law}}$) to assess which model better-describes the data. We find that a Schechter function is more appropriate for the total protocluster number counts,

and that a single power-law function is more appropriate for the protocluster containing a BCG. The resulting fit parameters are provided in Table 3 (where the values are the means of the posterior distributions, and the uncertainties are 68 per cent confidence intervals), and in Fig. 4 we show the best-fit functions, where the shaded regions were calculated by varying the best-fit parameters within their 68 per cent confidence intervals and taking the largest difference.

We would now like to quantitatively compare our number counts to the stellar mass function of $z = 1$ clusters found by [van der Burg et al. \(2013\)](#). To do this, we note that [van der Burg et al. \(2013\)](#) provide a best-fit Schechter function to the stellar mass number counts measured for a $z = 1$ cluster. They find a characteristic stellar mass of $(5.2^{+1.1}_{-0.2}) \times 10^{10} M_{\odot}$ and a slope of $-0.46^{+0.08}_{-0.26}$ (we ignore the normalization here because we have arbitrarily scaled their counts). For reference, in Fig. 4 we show their best-fit Schechter function as a shaded region encompassing the uncertainties of their best-fit parameters. The characteristic stellar mass found for our total protocluster is $(6.2^{+0.8}_{-3.9}) \times 10^{10} M_{\odot}$ and the slope found is $-0.3^{+0.3}_{-0.3}$, in excellent agreement. However, as mentioned at the beginning of this Section, incompleteness below stellar masses of $10^{10} M_{\odot}$ could be an issue, which could steepen the slope and lower the characteristic stellar mass, thus it is unclear if this agreement is intrinsic.

4.5 Ultraviolet versus far-infrared sizes

Many studies have looked at the physical extent of stellar emission compared to dust emission in SMGs (e.g. [Simpson et al. 2015](#); [Lang et al. 2019](#)), finding that the dust emission (and hence the star formation), probed by rest-frame far-infrared observations, is typically more smooth and compact, while the optical stellar emission is clumpy and extended, likely due to patchy dust attenuation (e.g. [Cochrane et al. 2019](#)). Although our data *HST* are probing a slightly different population of stars in the ultraviolet, we emphasize that *HST* is still currently the best facility for performing these measurements on objects at such high redshift. The forthcoming *James Webb Space Telescope (JWST)* will operate at the longer wavelengths needed to resolve the average stellar populations in SPT2349–56, and we will carry out the measurements when the facility becomes available. On the other hand, our 850- μm ALMA observations probe the rest-frame at 160 μm where the dust is expected to be bright.

To test this result for the galaxies in SPT2349–56, in Fig. 5 (top left panel) we first plot our derived rest-frame ultraviolet sizes as a function of their SFR, compared to a sample of $z \approx 2$ field SMGs from [Swinbank et al. \(2010\)](#) (with corresponding SFR estimates from [Chapman et al. 2005](#)), which were observed by the ACS instrument onboard *HST* in the F775W filter (observed wavelength 770 nm). These SMGs were selected from SCUBA surveys of various other cosmological fields, and the rest wavelengths probed by the observations range from 170 to 450 nm, comparable to our coverage of 290 nm. We next show a sample of three $z \approx 2.5$ field dusty star-forming galaxies from [Barro et al. \(2016\)](#) that were observed by the ACS F850LP filter (910 nm in the observed frame, 260 nm in the rest frame). These galaxies were selected from the CANDELS survey of the GOODS-S field ([Grogin et al. 2011](#)) for their compact nature and brightness at far-infrared wavelengths, thus follow-up observations found them to be reasonably bright at submm wavelengths (> 1 mJy at 870 μm) and have large SFRs ($> 100 M_{\odot} \text{yr}^{-1}$), so we simply refer to them as SMGs. In these comparison samples, the Sérsic index was allowed to vary, and the half-light radii are the semi-major axes of an ellipse containing half the total flux density, consistent with our definition of the half-light radius.

We also include star-forming galaxies in the range $z = 4$ –5 from the

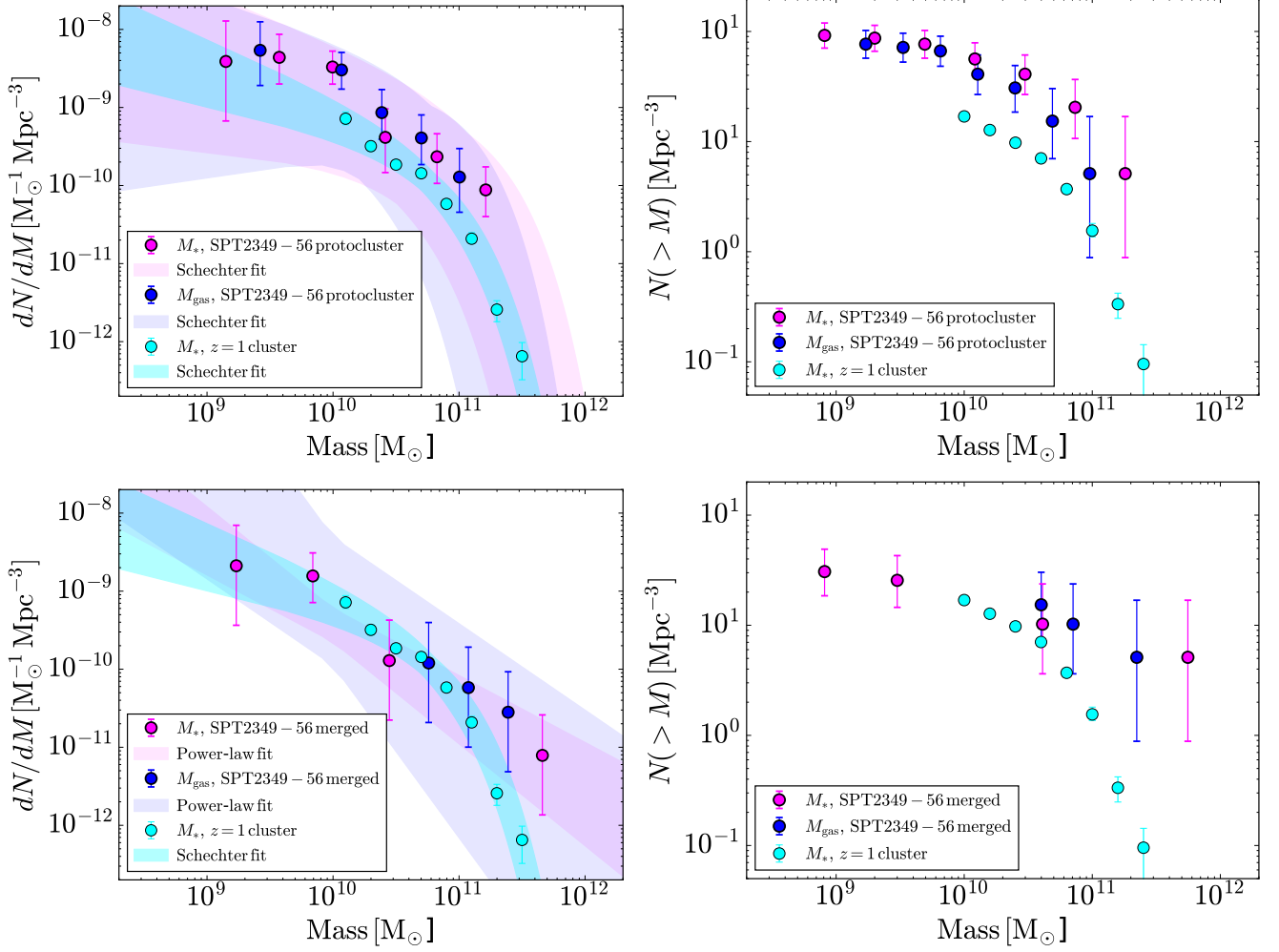


Figure 4. *Top:* Molecular gas mass and stellar mass differential (left panel) and cumulative (right panel) number counts for SPT2349–56. The stellar mass number counts for $z \sim 1$ clusters from [van der Burg et al. \(2013\)](#) is shown in cyan for comparison. Best-fit Schechter functions are shown for our differential counts, where the shaded regions are calculated by varying the best-fit parameters within their 68 per cent confidence intervals and taking the largest difference. The best-fit Schechter function from [van der Burg et al. \(2013\)](#) is shown as well, with the shaded region calculated in the same way. *Bottom:* Since the core galaxies will merge into a single BCG in a few hundred Myrs ([Rennehan et al. 2020](#)), we show the molecular gas mass and stellar mass differential (left panel) and cumulative (right panel) number counts after summing the masses of the galaxies within 90 kpc of the far-infrared luminosity-weighted centre and treating this as a single point. We also show best-fit power-law functions as shaded regions, calculated in the same way as above, and the same best-fit Schechter function for $z \sim 1$ clusters from [van der Burg et al. \(2013\)](#).

Table 3. Best-fit mass function parameters (Eqs. 6 and 7) derived from the stellar mass and molecular gas mass number counts for all of the galaxies in SPT2349–56, and SPT2349–56 after the central galaxies merge into a BCG, estimated by summing the masses of the central galaxies and treating them as a single source.

Component	Function	ϕ^*	M^*	α
		$[10^{-10} M_{\odot}^{-1} \text{Mpc}^{-3}]$	$[10^{10} M_{\odot}]$	
Protocluster, stellar mass	$\phi^* \left(\frac{M}{M^*}\right)^{\alpha} e^{-M/M^*}$	19^{+4}_{-16}	$6.2^{+0.8}_{-3.9}$	$-0.3^{+0.3}_{-0.3}$
Protocluster, molecular gas mass	$\phi^* \left(\frac{M}{M^*}\right)^{\alpha} e^{-M/M^*}$	22^{+6}_{-18}	$5.0^{+1.1}_{-3.4}$	$-0.1^{+0.3}_{-0.5}$
BCG, stellar mass	$\phi^* \left(\frac{M}{M^*}\right)^{\alpha}$	5^{+1}_{-2}	1^a	$-1.0^{+0.2}_{-0.2}$
BCG, molecular gas mass	$\phi^* \left(\frac{M}{M^*}\right)^{\alpha}$	37^{+18}_{-36}	1^a	$-1.5^{+0.4}_{-0.7}$

^aThis parameter was fixed during the fitting.

ALPINE survey with reliable fits to imaging in both *HST*'s F160W filter and in ALMA moment-0 maps of [CII] line emission (Fujimoto et al. 2020); for these galaxies, the rest-wavelength observed ranged from 230 to 280 nm. For these measurements, the Sérsic index was fixed to $n = 1$, but the authors note that fixing $n = 0.5$ affected their size measurements only at the ≈ 5 per cent level. For comparison, the mean Sérsic index from our fits is 0.84. Fujimoto et al. (2020) also provides circularized sizes, defined with respect to our size measurements as $r_c = r_{1/2} \sqrt{q}$, where q is the semi minor-to-semi major axis ratio. The mean q found in our fits is 0.67, so we divide their size measurements by $\sqrt{q} = 0.82$.

For reference, we show the half-light radius of the *HST* F160W PSF (approximately half the FWHM of 0.151 arcsec) as a horizontal dashed line. In Fig. 5 (top right panel) we show the same size measurements as a function of redshift. We see that the galaxies in our sample fit within the overall scatter of the comparison samples.

We next turn to our rest-frame far-infrared sizes of galaxies in SPT2349–56, taken from Hill et al. (2020), which were calculated using the same procedure as the [CII] sizes outlined in Section 3.6, only in this case after averaging the line-free ALMA channels. In Fig. 5 (bottom left panel) we show these size measurements as a function of SFR, and compare them to the same field galaxies from Barro et al. (2016) (which measure the rest-frame far-infrared at 250 μm). In this comparison we have included the same galaxies from the ALPINE survey with [CII] size measurements from Fujimoto et al. (2020) (corrected by the mean [CII] axis ratio found in our fits, $\sqrt{q} = 0.80$), and we have converted these [CII] size measurements to rest-frame far-infrared size measurements using the mean $R_{1/2, \text{C[II]}}/R_{1/2, \text{FIR}}$ ratio from our sample (described below). Again, the fits to the ALPINE galaxies were done with the Sérsic index fixed to 1, while the mean Sérsic index from our fits is 0.83. This sample measures the rest-frame far-infrared at 160 μm .

We also include the size of the stacked image, arbitrarily placed at $100 M_{\odot} \text{ yr}^{-1}$. For reference, we show the half-light radius of the ALMA synthesized beam ($\sqrt{ab}/2 = 0.2$ arcsec, where a and b are the major and minor FWHM, respectively) as a horizontal dashed line. In Fig. 5 (bottom right panel) we show the same size measurements as a function of redshift. The galaxies in SPT2349–56 span a range of sizes comparable to the star-forming field galaxies from the ALPINE galaxy, with no discernable trend with SFR. This result is in agreement with the idea that not all SMGs are compact starbursts, and instead there is some heterogeneity in the SMG population (e.g., Hayward et al. 2012, 2013).

In Fig. 6 (right panel) we show the ratio of the rest-frame far-infrared size to the ultraviolet size, $R_{1/2, \text{FIR}}/R_{1/2, \text{UV}}$, for the galaxies in SPT2349–56, as well as the size ratio for the stacks. We note that all of the galaxies here are core galaxies of SPT2349–56, since our high-resolution submm imaging only covered this region. The field SMGs from Barro et al. (2016) and Fujimoto et al. (2020) are shown alongside our sources on this plot, but we note that the field SMGs from Swinbank et al. (2010) have not been observed at high resolution in the submm and so are omitted from this comparison. Unfortunately, there are only three sources (C2, C6, and C8) for which we could measure both a far-infrared size and an ultraviolet size. To improve the sample size, we can look at the [CII] sizes for some of our sources, where the emission is much brighter, and use this as a proxy for the dust sizes.

In Fig. 6 (left panel) we plot the ratio $R_{1/2, \text{C[II]}}/R_{1/2, \text{FIR}}$ as a function of SFR for all sources where both measurements are available. We find a relatively consistent ratio across all SFR values, with a mean of 1.3 ± 0.2 . Next, in Fig. 6 (right panel) we use the ratio $R_{1/2, \text{C[II]}}/R_{1/2, \text{UV}}$ divided by the mean ratio above to provide an

estimate of the underlying continuum size of sources where such a measurement is not available; this adds one more galaxy (C17) to the sample. We find that the far-infrared emission is comparable in size to the ultraviolet emission, with a weighted mean of 1.4 and a weighted standard deviation of 0.6. The corresponding ratio for our stacked images is 0.9 ± 0.2 , consistent (within the scatter) with the mean ratio of our sample, and we do not see any evidence for a difference between the comparison samples. This is consistent with simulations of high- z star-forming galaxies (e.g. Cochrane et al. 2019).

4.6 Radial surface brightness distributions

Since most of the galaxies in our sample are not well enough detected to measure ultraviolet sizes, we can instead investigate the average ultraviolet profile by looking at our stacked F160W image (Fig. 2). In Fig. 7 (left panel) we show the surface brightness of the stack as a function of radius, calculated in elliptical annuli with widths of 1 pixel, where the shape of the annuli was set to the best-fit ellipticity and position angle from the Sérsic profile fit. In this plot the points and the error bars are the means and standard deviations of the pixel values within each annulus, respectively. Here we have converted our surface brightness measurements to units of $\mu\text{Jy kpc}^{-2}$ by dividing by the number of kpc^2 in a pixel of our image. For the last point our measurement is consistent with zero, so we show the 1σ upper-limit. We also show the best-fit Sérsic function as a shaded region, where the width is obtained by varying the best-fit parameters within their 68 per cent confidence intervals.

In our stacking analysis we have omitted galaxy C6, by far the brightest source detected in our *HST* F160W imaging and clearly an outlier in our *HST* imaging. In order to compare the properties of this galaxy to the rest of the sample, in Fig. 7 (right panel) we show its surface brightness profile, calculated in the same way as with the stack. In order to assess whether or not we are seeing resolved emission in these surface brightness profiles, we compare them to the *HST* F160W PSF model described in Section 3.5. Figure 7 shows the surface profile of the model PSF for reference, normalized to the value of the central pixel of the stacked submm image (left panel) and galaxy C6 (right panel). We find that beyond about 2 pixels (or about 1 kpc) our stacked galaxy image shows significantly more emission compared to the stacked star, so we are indeed measuring extended emission, yet galaxy C6 is effectively indistinguishable from an unresolved point source.

A similar stacking analysis was performed for the $z \approx 2$ field SMGs of Swinbank et al. (2010), who analysed *HST*-F775W imaging of the sample of 25 spectroscopically-confirmed SMGs initially discovered in large single-dish submm surveys. Upon rescaling and stacking their detections, it was found that a Sérsic index of 2.6 ± 1.0 best described their data, in agreement with our value of 1.72 ± 0.30 . In Fig. 7 (left panel) we show their fit as a grey shaded region, where the width corresponds to the uncertainties in their best-fit parameters. We set the scale radius to be 2.7 ± 0.4 kpc, corresponding to the median half-light radius of their sample, and scale the amplitude to have the same integrated flux density as our stack, then convolve the 1-D profile with a Gaussian of width equal to the *HST* beam in the F160W filter. We see that the surface brightness profile of our stack is consistent out to where our data are sensitive.

We next turn to comparing galaxy C6 with the literature. The three GOODS-S galaxies at $z \approx 2.5$ from Barro et al. (2016) observed in the F850LP filter (rest-wavelength 260 nm) were selected for their small rest-frame optical sizes and high stellar-mass densities, similar to what we are seeing with galaxy C6. In Fig. 7 (right panel) we show their resulting best-fit Sérsic profiles, normalized by their

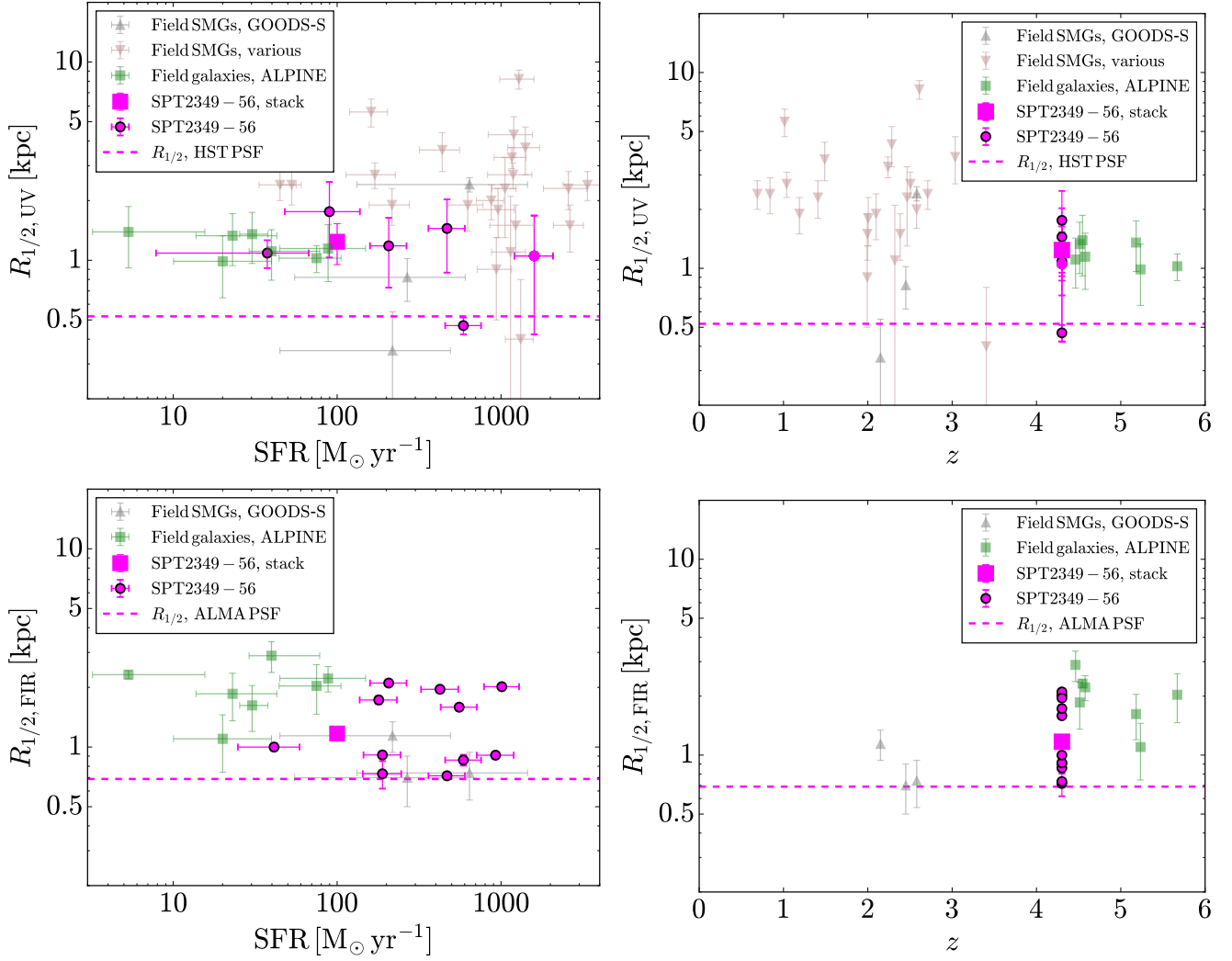


Figure 5. *Top left:* Ultraviolet half-light radius as a function of SFR for all galaxies in the SPT2349–56 protocluster detected in the F160W band with pixels above 5 times the local rms. Also shown are results for $z=1-3$ field SMGs from Swinbank et al. (2010) and Barro et al. (2016), and $z=4-5$ star-forming galaxies from the ALPINE survey (Fujimoto et al. 2020). For reference, the size measured in our *HST* F160W stack is shown as the pink square, arbitrarily placed at $100 M_{\odot} \text{ yr}^{-1}$, and the half-light radius of the *HST* F160W beam is shown as the horizontal dashed line. *Top right:* Ultraviolet half-light radius as a function of redshift for the same galaxies in SPT2349–56, compared to the same literature samples. The stacked size measurement and beam size is also shown for comparison. *Bottom left:* Far-infrared half-light radius as a function of SFR from Hill et al. (2020), for all galaxies detected by ALMA at $850 \mu\text{m}$ with pixels above 5 times the local rms, along with our stack shown as the pink square. Also shown are results for the field SMGs from Barro et al. (2016), and [CII] size measurements from the ALPINE survey (Fujimoto et al. 2020), converted to far-infrared sizes using the mean $R_{1/2, \text{C[II]}}/R_{1/2, \text{FIR}}$ ratio from our sample (see Fig. 6). The half-light radius of the ALMA synthesized beam is shown as the horizontal dashed line. *Bottom right:* Far-infrared half-light radius as a function of redshift for the same galaxies in SPT2349–56, compared to the same literature samples and the beam size.

stellar masses (around $10^{11} M_{\odot}$) relative to C6, and convolved with a Gaussian of width equal to the *HST* beam in the F160W filter; this assumes that each source is at the same redshift as SPT2349–56 in order to provide a direct comparison with our observations. We have highlighted the range in surface brightness they span for clarity. We see that the compact SMGs in this sample would all effectively appear unresolved in our *HST* imaging, similar to C6.

We can also compare the current profile of galaxy C6 to a prediction of its profile from the hydrodynamical simulation presented by Rennehan et al. (2020). We take the median stellar mass profiles from four independent runs initialized with gas fractions of 2.3 (for reference, the range measured for these galaxies is 0.1 to 4.8), and then we take the average between 700 and 800 Myr. The overall normalization of the profile is highly uncertain in the simulation as

it requires radiative transfer models to convert stellar mass into rest-frame ultraviolet flux density, so we simply normalize the profile by the peak pixel in our F160W imaging of C6. The resulting profile is shown in Fig. 7, and we see that after the merger, the BCG will remain quite compact. Nonetheless, we expect the dark matter halo to grow in size after the merger, so in Fig. 7 we also show the resulting shape of the dark matter halo, normalized in the same way for easy comparison with the stellar profile. We see that the shape of the dark matter halo after the merger is much more extended than the stellar mass profile.

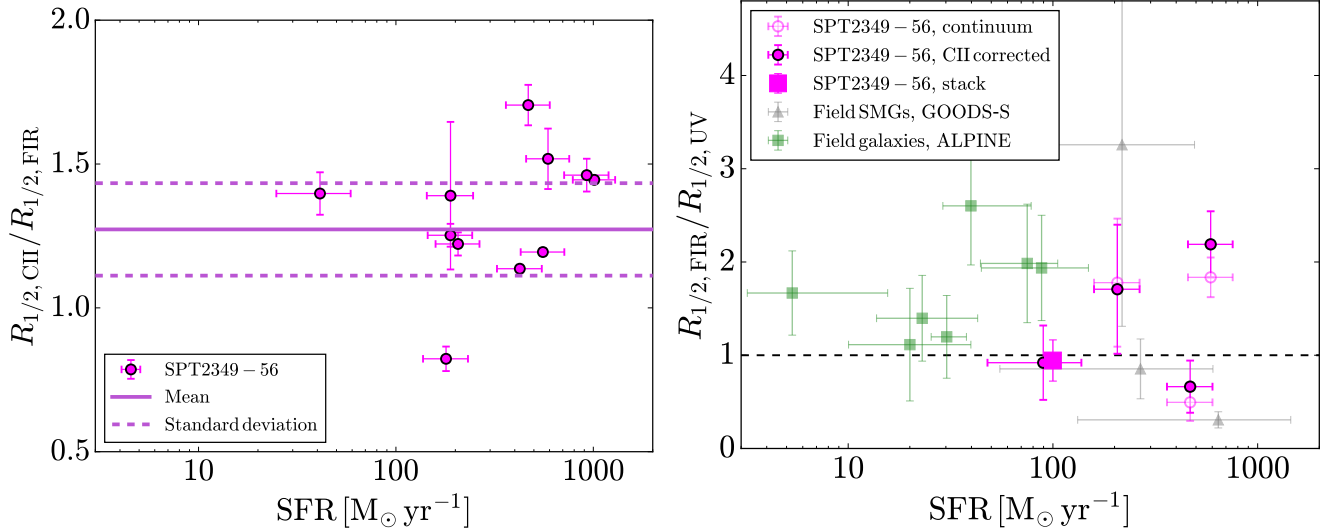


Figure 6. *Left:* Ratio of [CII] half-light radius to far-infrared half-light radius as a function of SFR for galaxies in SPT2349–56. The mean value is 1.3 (solid line) with a standard deviation of 0.2 (dotted line). *Right:* Ratio of far-infrared half-light radius to ultraviolet half-light radius; this is shown as the open circles for the four galaxies in SPT2349–56 for which both measurements are available. Since there are only four galaxies with both size measurements available, we show the ratio $R_{1/2, \text{CII}}/R_{1/2, \text{UV}}$ as solid circles and correct it using the mean ratio of [CII] to far-infrared size from the left panel in order to estimate $R_{1/2, \text{FIR}}/R_{1/2, \text{UV}}$. The pink square shows the same ratio for the size measurements of our stacked images. We compare our size ratio measurements to the sample of field SMGs from the GOODS-S field (Barro et al. 2016) and the star-forming galaxies from the ALPINE survey (Fujimoto et al. 2020). A dashed horizontal line is drawn where $R_{1/2, \text{F}} = R_{1/2, \text{UV}}$ for clarity.

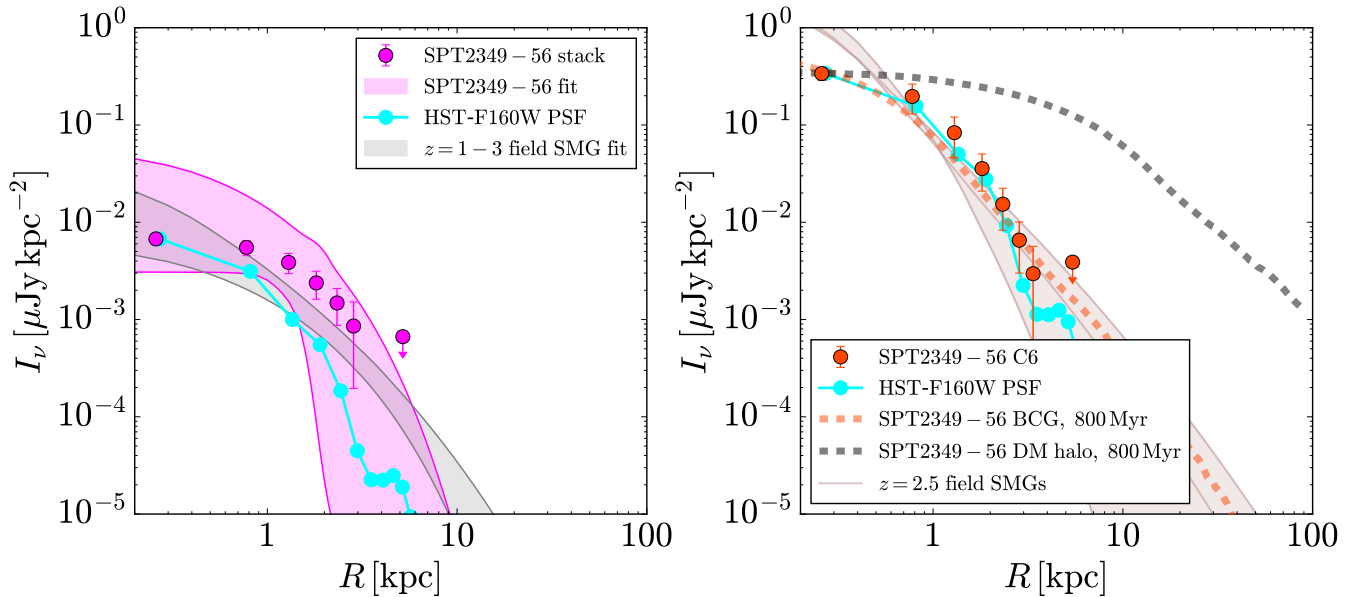


Figure 7. Surface brightness as a function of radius for the protocluster galaxies in SPT2349–56, determined within elliptical annuli of 1-pixel width. The points and the error bars are the means and standard deviations of the pixel values within each annulus. Where the standard deviation overlaps with zero, we provide 1σ upper-limit. *Left:* In magenta we show the surface-brightness profile for our stack of *HST*-detected galaxies (after removing C6, a bright outlier), with the best-fit Sérsic profile shown as the magenta shaded region, and in cyan we show the *HST*-F160W PSF. For comparison, we show the best-fit surface-brightness profile from a similar stacking analysis of 25 field SMGs (grey shaded region) observed by *HST* in the F775W filter by Swinbank et al. (2010), normalized to have the same integrated flux density as our stack. *Right:* In red we show the surface brightness profile for galaxy C6, and in cyan we show the same *HST*-F160W PSF. For comparison, in brown we show a set of three best-fit surface-brightness profiles of SMGs around $z=2.5$ from Barro et al. (2016), normalized by their stellar masses relative to C6. We have then convolved each profile with the *HST*-F160W PSF, assuming each source is at the same redshift as SPT2349–56, in order to provide a direct comparison with our observations. Here we have highlighted their total range for clarity. We show the expected stellar profile (as a dashed red curve) and dark matter profile (as a dashed black curve) of the BCG complex after 800 Myr, once the central galaxies have merged (Rennehan et al. 2020), also normalized by the peak pixel value of C6.

5 DISCUSSION

5.1 The stellar properties of SPT2349–56

The protocluster SPT2349–56 is a unique object when observed in the submm. We now know that the total SFR exceeds $10,000 M_{\odot} \text{ yr}^{-1}$, and its extreme nature in this regard is due to the fact that it was specifically selected as one of the brightest unlensed point sources in the SPT mm-wavelength survey. However, as we continue to study this protocluster in other wavelengths, it is becoming clear that the contrast of the system is not as striking in other wavelengths as it is in the submm. For example, due to the extremely dusty nature and high redshift of most of the galaxies in SPT2349–56, at rest-frame ultraviolet wavelengths this protocluster is not significantly brighter than the field.

Nonetheless, we have found that the stellar masses derived through SED fitting place these galaxies inconspicuously on the MS, as opposed to appearing as outliers above it; given their incredibly high SFRs, this means that they have correspondingly large stellar masses, which are simply hidden by dust. For reference, the total stellar mass of all the known galaxies in SPT2349–56 is $(1.5 \pm 0.3) \times 10^{12} M_{\odot}$, which is comparable to a large BCG at $z < 0.1$.

Another related observation is that the mean molecular gas-to-stellar mass ratio and depletion timescale for galaxies in SPT2349–56 and one other $z = 4$ protocluster are potentially lower than for field SMGs around the same redshift, although the scatter is considerable. Interestingly, similar studies of CO lines at moderate redshift ($z = 1-3$) have found that star-forming galaxies in cluster/protocluster environments at this epoch have systematically higher molecular gas-to-stellar mass ratios and depletion timescales compared to scaling relations derived from the field (e.g., Noble et al. 2017; Hayashi et al. 2018; Tadaki et al. 2019), while at $z < 1$ galaxy clusters have nearly depleted all of their gas and ceased forming stars (e.g., Young et al. 2011; Jablonka et al. 2013; Scott et al. 2013; Boselli et al. 2014; Zabel et al. 2019).

To quantify this, in Fig. 8 we show the molecular gas-to-stellar mass ratio (top panel) and depletion timescale (bottom panel) as a function of redshift for the galaxies in SPT2349–56, compared to other clusters and protoclusters with molecular gas mass estimations made through observations of CO, and with sufficient multiwavelength coverage to have stellar mass and SFR estimates. At $z = 4.0$ we show the DRC (Oteo et al. 2018; Long et al. 2020), and we have converted CO(6–5) line intensities to molecular gas masses using an $L'_{(6-5)}/L'_{(1-0)}$ factor of 0.46 (the mean ratio found for the SPT-SMG sample, see Spilker et al. 2014) and an α_{CO} of $1 M_{\odot}/(\text{K km s}^{-1} \text{ pc}^2)$ (the same scale factor used for our sample). At intermediate redshift ($z = 1-3$) we show results from observations of CO(3–2), CO(2–1), and CO(1–0) in members of three *Spitzer* Adaptation of the Redsequence Cluster Survey (SpARCS) clusters (Noble et al. 2017), XMMXCS J2215.9–1738 (Hayashi et al. 2018), three Ly α -selected protoclusters (Tadaki et al. 2019), and CLJ1001 (Wang et al. 2018). At low redshift ($z < 1$) we take observations of CO(3–2), CO(2–1), and CO(1–0) in members of the Fornax cluster (Zabel et al. 2019), Abell 2192 and Abell 963 (Cybulski et al. 2016), CL1411.1–1148 (Spérone-Longin et al. 2021), CL0024+16 (Geach et al. 2009, 2011), and MACS J0717.5+3745, Abell 697, 963, 1763, and 2219 (Castignani et al. 2020). We note that these comparison samples consistently used CO conversion factors of $L'_{(2-1)}/L'_{(1-0)} = 0.8$ and $L'_{(3-2)}/L'_{(1-0)} = 0.5$, and $\alpha_{\text{CO}} \approx 4 M_{\odot}/(\text{K km s}^{-1} \text{ pc}^2)$, with small corrections for metallicity made in some cases. This conversion factor is appropriate for normal star-forming galaxies, which were the targets of these literature studies, and a lower conversion factor

around $1 M_{\odot}/(\text{K km s}^{-1} \text{ pc}^2)$ is typically used for SMGs, as with SPT2349–56 and the DRC. Some galaxies in the sample of Castignani et al. (2020) approach the high SFRs in the SMG regime, and they have adopted a smaller conversion factor for those sources. For each cluster in this figure, we show the mean molecular gas-to-stellar mass ratio and depletion timescale as a square symbol, with error bars representing the standard deviation for clusters with more than two galaxies with sufficient data.

To incorporate the properties of field galaxies in this figure, we use the scaling relations for $\langle \mu_{\text{gas}} \rangle$ and $\langle \tau_{\text{dep}} \rangle$ (where $\langle \rangle$ denotes the average of the field population) estimated by Tacconi et al. (2018), derived from observations of CO lines and continuum flux densities up to millimetre wavelengths in over 1300 field galaxies between $z = 0$ and 4 (including the sample from Scoville et al. 2016). They provide equations for calculating $\langle \mu_{\text{gas}} \rangle$ and $\langle \tau_{\text{dep}} \rangle$ as a function of redshift, M_* , SFR, and the effective radius at rest-frame 500 nm; however, since we do not have access to size measurements for most of the galaxies in our comparison sample, we use their fits that do not include this parameter. Figure 8 shows several representative curves for $\langle \mu_{\text{gas}} \rangle$ and $\langle \tau_{\text{dep}} \rangle$ given different values of M_* and SFR. In the bottom panels of Fig. 8 we show the ratios $\mu_{\text{gas}} / \langle \mu_{\text{gas}} \rangle$ and $\tau_{\text{dep}} / \langle \tau_{\text{dep}} \rangle$, obtained by dividing each galaxy’s molecular gas-to-stellar mass ratio and depletion timescale by the prediction from Tacconi et al. (2018), taking into account each galaxy’s redshift, M_* , and SFR. We confirm that at $z = 1-3$ most cluster environments are gas-rich, as discussed in previous studies, and we see that the galaxies in SPT2349–56 and the DRC continue to fall below the expected molecular gas-to-stellar mass ratios and depletion timescales of field galaxies.

In our comparison of the stellar mass function of SPT2349–56 with the stellar mass function of $z = 1$ galaxy clusters, we found similar shapes well-described by Schechter functions. Since we know that the core galaxies will merge over a timescale of a few hundred Myrs, we also computed the stellar mass function of SPT2349–56 after summing up the stellar masses of these galaxies and treating them as a single source. In this case we found that the number counts are better-fit by a single power law, indicating that if this structure is to continue along an evolutionary path to become a $z = 1$ galaxy cluster, the remaining cluster stellar mass will come from lower-mass galaxies (e.g. Naab et al. 2009). However, we have not taken into account the observational biases inherent in our sample selection technique, which focused on star-forming galaxies, and so it is not clear from the current data whether these galaxies are already within the 1 Mpc environment of SPT2349–56 and have not been detected, or have yet to fall into the galaxy protocluster. It is worth noting that this behaviour is consistent with the notion of ‘down-sizing’, where the most massive galaxies formed the earliest times, which has been observed in numerous samples of galaxies (e.g., Cowie et al. 1996; Magliocchetti et al. 2013; Miller et al. 2015; Wilkinson et al. 2017).

Lastly, we have noted that the ratio of far-infrared size to ultraviolet size is comparable to star-forming galaxies found around the same redshift, and field SMGs at lower redshift ($z \approx 2.5$). A similar study at $z \approx 1$ also found that the stellar emission in cluster galaxies is more compact than in field galaxies (Matharu et al. 2019), which is not what we are seeing here, although the sample sizes we are investigating are small, and there could be systematic differences in the size measurements. Nonetheless, we might not expect to see many differences between field galaxies and protocluster galaxies at high redshift as there has not been enough time for the clustering environment to shape the residing galaxies.

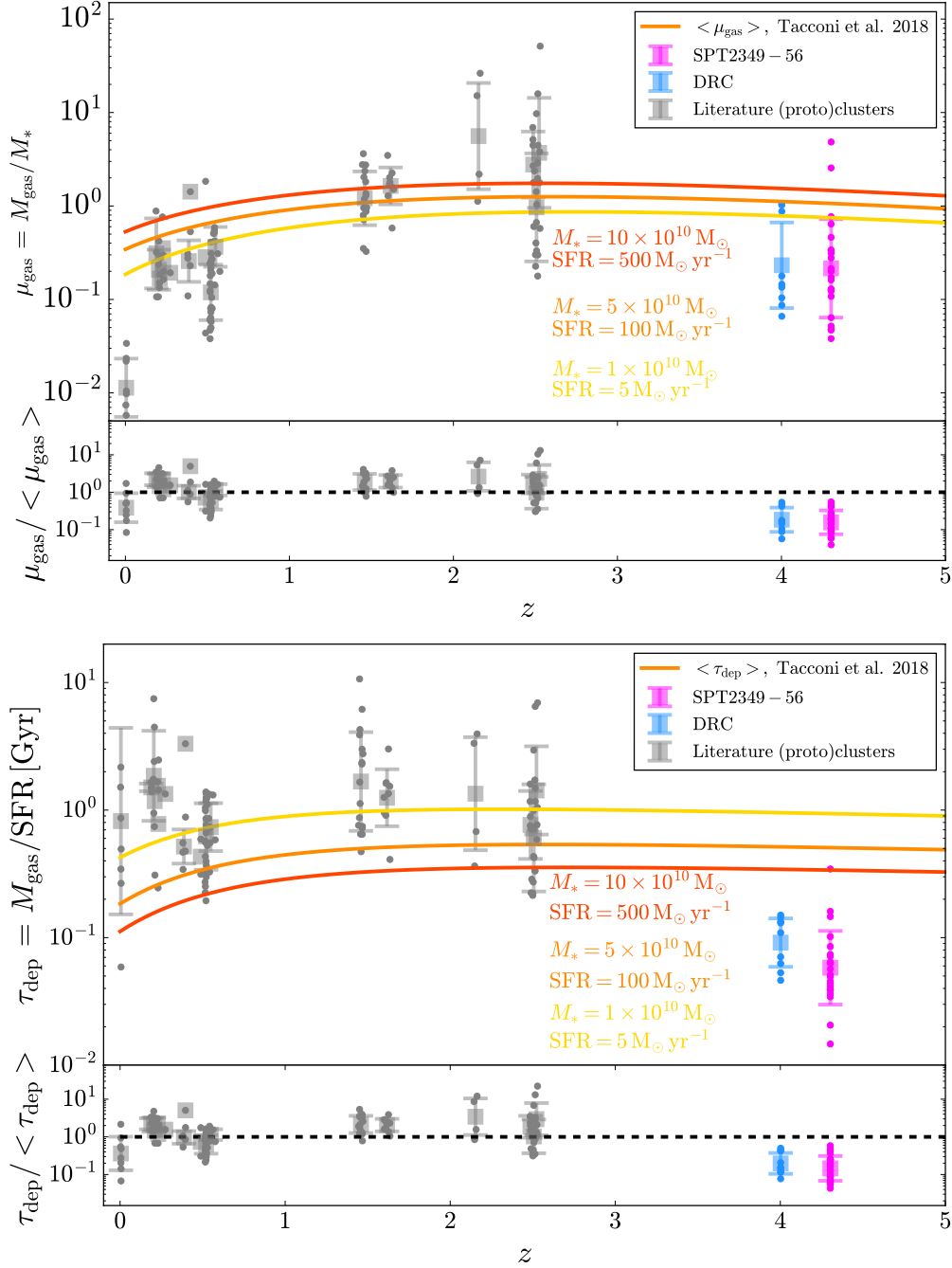


Figure 8. *Top:* Molecular gas-to-stellar mass ratio ($\mu_{\text{gas}} = M_{\text{gas}} / M_*$) as a function of redshift for SPT2349–56 (pink), the DRC (blue), and various clusters and protoclusters with similar CO-derived molecular gas mass data available (grey; references are provided in the text). Points indicate values for individual galaxies, while squares show the mean values for each (proto)cluster, and error bars show the standard deviations for (proto)clusters with more than two sources available. Representative models for the mean molecular gas-to-stellar mass ratio of field galaxies ($\langle \mu_{\text{gas}} \rangle$) from Tacconi et al. (2018) are shown as the red, orange, and yellow curves. The bottom panel shows the ratio $\mu_{\text{gas}} / \langle \mu_{\text{gas}} \rangle$, calculated for each galaxy given its redshift, M_* , and SFR, along with the means and standard deviations for each (proto)cluster. *Bottom:* Same as the top panel, only showing the depletion timescale ($\tau_{\text{dep}} = M_{\text{gas}} / \text{SFR}$).

5.2 The properties of a BCG in formation

In our analysis above, we have paid special attention to separating the central galaxies of SPT2349–56 from the wider protocluster. In Rennehan et al. (2020), hydrodynamical simulations using the positions of these central galaxies as the initial conditions predicted a complete merger on timescales of a few hundred Myrs, while in Hill et al. (2020) it was found that the velocity distribution within

this region was consistent with a Gaussian distribution, and that the velocity dispersion predicted a central mass of $(9 \pm 5) \times 10^{12} M_{\odot}$. Summing up the stellar masses of each of these central galaxies yields a value of $(9 \pm 2) \times 10^{11} M_{\odot}$, consistent (within the uncertainties) with the mass of $(12 \pm 3) \times 10^{11} M_{\odot}$ estimated by Rotermund et al. (2021).

Looking at Fig. 3, we see that these central galaxies lie close to

the MS found by [Khusanova et al. \(2020\)](#); although there are more galaxies below the MS than above it, given the uncertainties in our measurements of the SFRs and stellar masses in our sample we cannot rule this observation as statistically significant. Similarly, the two galaxies from the northern component of SPT2349–56 are significantly above the MS, but small number statistics again mean that we cannot draw any statistically significant conclusions from this observation. The MS distribution of SPT2349–56 overall matches well with what is seen with the DRC, a similar star-forming protocluster from the literature, along with other samples of field SMGs at high redshift.

In Fig. 9 we explore the concept of environmental dependence further by plotting the cumulative mass enclosed within a circular aperture as a function of the area of the aperture, separating out the stellar mass and the molecular gas mass. In this plot the centre of SPT2349–56 is the luminosity-weighted centre, as in [Hill et al. \(2020\)](#). We see that the molecular gas mass and stellar mass track one another across all scales probed by our data, from the region of the forming BCG (90 kpc, or about 0.03 Mpc^2) out to the northern component (about 0.5 Mpc away, or at 1 Mpc^2). To quantify this, in the bottom panel of Fig. 9 we show the total enclosed gas fraction, and we can see that it remains roughly constant at a level of about 0.8 (except for near the centre, but these fluctuations suffer from small-number statistics). For comparison, we show the same curve-of-growth for the DRC ([Oteo et al. 2018](#); [Long et al. 2020](#)); the behaviour of this protocluster is similar.

We then compare the stellar mass profiles of these high- z protoclusters to the stellar profile of a typical $z \approx 1$ galaxy cluster from [van der Burg et al. \(2014\)](#), obtained from the stack of the same sample of 10 clusters discussed in Section 4. The authors found a best-fit Navarro-Frenk-White (NFW) profile concentration parameter of $7^{+1.53}_{-0.99}$, which we use to plot the mass projected within a cylinder of a given area (see e.g. [Lokas & Mamon 2001](#)), taking the scale stellar mass to be $M_{200,*} = 2 \times 10^{12} M_{\odot}$, the median of their sample. We see that the shapes of the stellar mass curves between the protoclusters and the $z \approx 1$ clusters are similar, although the slope of the protoclusters becomes shallower than the slope of the $z = 1$ clusters at large radii. It is interesting to note that a similar study ([Albets et al. 2021](#)) investigating stacks of galaxy clusters between $z = 0.5$ and 1.6 in the near-infrared ($3\text{--}8 \mu\text{m}$ in the rest-frame) found similarly-concentrated light profiles, with NFW concentration parameters around 7; this near-infrared light is expected to trace stellar mass. They also investigated stacks in the far-infrared ($250\text{--}500 \mu\text{m}$ in the rest-frame), tracing dust emission and SFR, and found concentration parameters comparable to the near-infrared light. It was found that 20–30 per cent of the integrated cluster far-infrared emission comes from high-mass galaxies, while in [Hill et al. \(2020\)](#) about 50 per cent of the low-resolution single-dish far-infrared emission resolved into massive galaxies.

Despite the fact that the galaxies on-track to merge into a BCG are not altogether distinguishable from the rest of the protocluster (or indeed, from most SMGs at these redshifts), galaxy C6 does stand out from our core sample as having the brightest flux density at all optical-through-infrared wavelengths. Our SED modelling found that this galaxy’s stellar mass is $(4 \pm 1) \times 10^{11} M_{\odot}$, or roughly half of the total stellar mass expected to make up the BCG after the mergers are complete, and our brightness profile analysis of this galaxy suggests that it is incredibly compact.

The region around galaxy C6 is clearly at the centre of this BCG-in-formation. [Rotermund et al. \(2021\)](#) already discussed a plausible evolutionary track for the growth of the stellar mass of C6. Around $z = 0.5$, BCG stellar masses range from $5\text{--}10 \times 10^{11} M_{\odot}$ (e.g., [Hilton](#)

[et al. 2013](#)), so C6 is already nearly there, and once the merging is complete, it will be at the upper end of BCG masses known. In Fig. 7 we see that C6 is expected to remain compact after the merger, and so if C6 is to continue to grow in stellar mass, we might also expect it to grow by a considerable amount in size. This could happen through dry mergers (mergers between galaxies with little gas, and thus little star formation), which has been found to play an important role in the growth of BCGs (e.g., [Liu et al. 2009](#); [Lin et al. 2010](#); [Liu et al. 2015](#)), and simulations predict that this process will increase a BCGs size and make it less compact (e.g., [Khochfar & Silk 2006](#); [Oogi & Habe 2012](#)). This would need to occur after C6 merges with the core galaxies in its current vicinity, as these mergers will be gas-rich. From our simulation we see that the post-merger dark matter halo will have a large and extended profile, and this could become populated by further accretions and dry mergers if C6 grows following an inside-out scenario, where the slope of the outer profile becomes shallower with increasing mass (e.g., [van Dokkum et al. 2010](#); [Bai et al. 2014](#); [Whitney et al. 2019](#)). While we stress that the precise final mass and size of a BCG depends strongly on its detailed merger history, something we cannot know from system to system, we see that C6 is at least consistent with the picture that it is the progenitor of one of the most massive BCGs seen today, and that it has nearly formed all of its stars at this early epoch of formation.

These observations of a BCG in formation provide a direct measure of the ingredients that built up these massive galaxies in the early Universe. There are many studies of the stellar populations of BCGs that try to piece together their formation histories, which broadly points to an initial early phase of star-formation (e.g., [De Lucia & Blaizot 2007](#); [Collins et al. 2009](#); [Barbosa et al. 2016](#); [Cooke et al. 2019](#); [Edwards et al. 2020](#)). Here we provide a direct observation of this formation in progress, where we have access to information that will likely be lost after the merger of the core galaxies in SPT2349–56 into a BCG. In particular, we see that the ingredients of this BCG are numerous galaxies with very high star-formation rates that, once merged, will already have formed most of the stars that make up a typical BCG. Furthermore, stellar population studies are only able to trace BCG histories back to their early star-forming phase, which in the case of SPT2349–56, will begin after the merger. But by observing these galaxies before they merge into a BCG, we now have access to information about the stellar history of a BCG back to a much earlier time, as traced by the stellar populations of the pre-merger galaxies.

6 CONCLUSION

SPT2349–56 was selected as the brightest protocluster candidate from the SPT-SZ 2500 deg^2 mm-wavelength survey. This object has since been spectroscopically confirmed to be a true protocluster, containing over 30 submm-bright galaxies and dozens more LBGs and LAEs. In this paper we have described our results from an extensive optical-through-infrared follow-up campaign using Gemini GMOS and FLAMINGOS-2, *HST*-F110W and F160W, and *Spitzer* IRAC 3.6 and $4.5 \mu\text{m}$.

Owing to the ≈ 2 arcsec spatial resolution of the IRAC images, source blending is an issue that needs to be dealt with. We deblended our IRAC data using *t*-phot, which used galaxy positions from our *HST* imaging as a prior and subsequently convolved their profiles with the IRAC PRF to develop a catalogue of the underlying source distribution as seen by IRAC. Source catalogues for our Gemini and *HST* imaging were extracted using standard source-extractor routines.

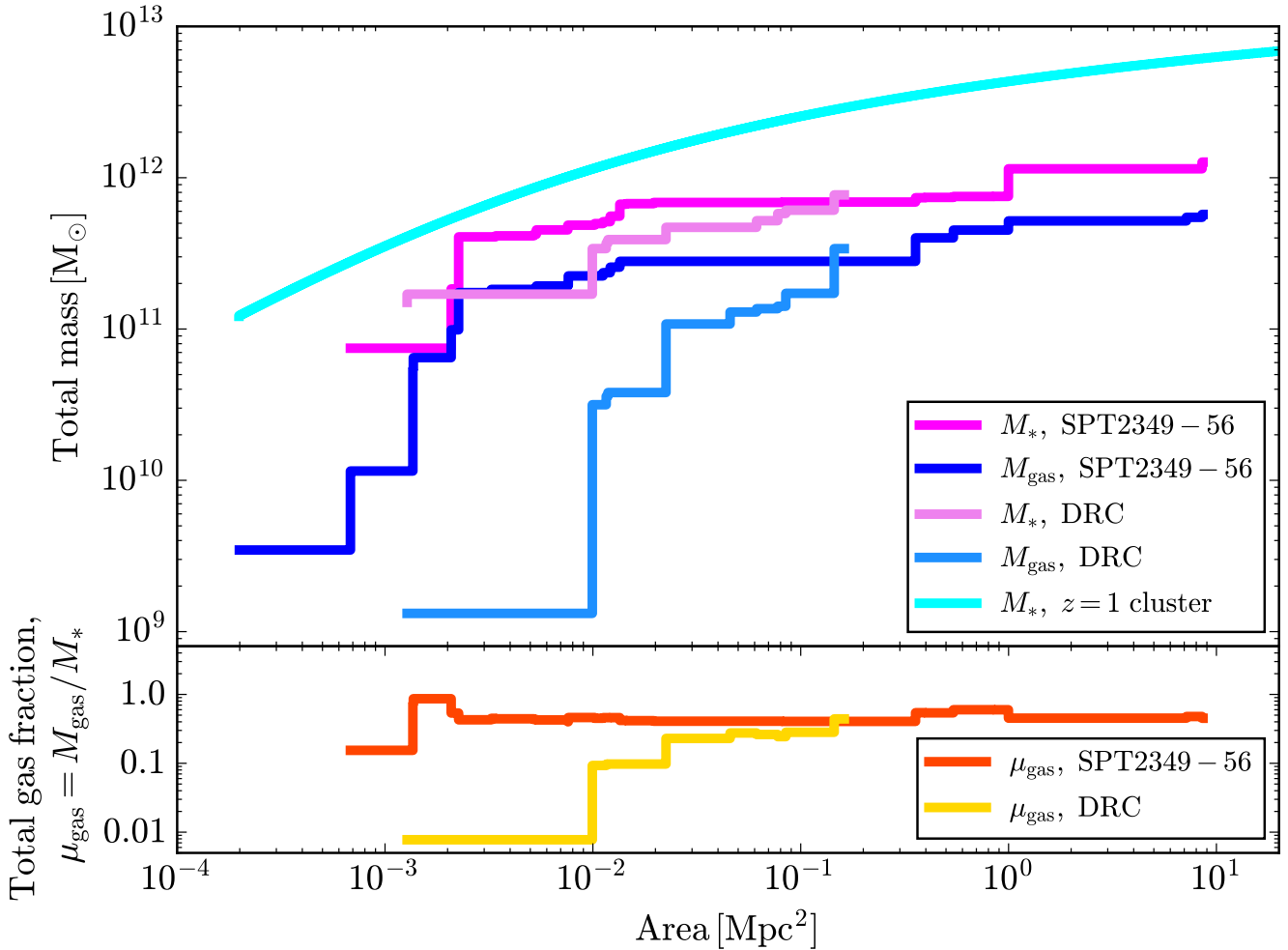


Figure 9. *Top:* Cumulative mass enclosed within a circular aperture as a function of the area of the aperture, centred on the infrared luminosity-weighted centre of SPT2349–56 (see Hill et al. 2020 for details). In blue we show the molecular gas mass, and in magenta we show the stellar mass. We find that the masses track each other well, implying that the inner region of the protocluster has not had a chance to differentiate from the outer regions. Also shown are the stellar and molecular gas masses of the DRC (Oteo et al. 2018; Long et al. 2020), and the best-fit NFW profile to the stellar mass profile of a stack of $z = 1$ clusters from van der Burg et al. (2014). *Bottom:* Total gas fraction μ_{gas} (Eq. 3) enclosed within the same apertures as a function of area.

We matched the known protocluster galaxies in SPT2349–56 discovered by ALMA to our optical and infrared catalogues using a simple radial cut of 1 arcsec. We found a match in at least one of the eight optical/infrared filters for all but six galaxies. In addition, we searched for ALMA counterparts to a small sample of LBGs and LAEs, and found matches for all but one galaxy.

Taking the photometry measured in these data, and combining it with existing mm-wavelength photometry from *Herschel*-SPIRE and ALMA, we used CIGALE to fit SEDs to each galaxy, allowing stellar masses, dust extinctions, ages, star-formation timescales, and star-formation rates to vary.

We found that the galaxies in SPT2349–56 follow the galaxy main sequence, consistent with other samples of $z \approx 4$ protocluster galaxies and field SMGs. In addition, we find a wide range of molecular gas-to-stellar mass ratios, but short depletion timescales. Field SMGs at similar redshifts are seen to have on average higher molecular gas-to-stellar mass ratios and depletion timescales than SPT2349–56 and other protocluster galaxies, although the scatter in both populations is large. We find the same result using known scaling relations calibrated from large samples of field galaxies up to redshift 4. This

could mean that protocluster galaxies in SPT2349–56 are at a late stage in their star-formation phase and have already nearly depleted their gas reservoirs as they build up their stars.

We computed the stellar-mass function and gas-mass function of SPT2349–56 in two ways: first, for the entire sample of galaxies; and second, by collapsing the core galaxies into a single source, reflecting the fact that they are expected to merge within a timescale of a few hundred Myrs. We find that the stellar- and gas-mass functions track each other well. Comparing the total protocluster stellar mass function to the stellar-mass function of typical $z = 1$ galaxy clusters, we find that the samples are consistent with one another and are well-fit by Schechter functions. The best-fit characteristic mass for the $z = 1$ galaxy clusters is $(5.2^{+1.1}_{-0.2}) \times 10^{10} M_{\odot}$, and the slope is $-0.46^{+0.08}_{-0.26}$, compared to SPT2349–56, where we find a best-fit characteristic mass of $(6.2^{+0.8}_{-3.9}) \times 10^{10} M_{\odot}$ and a slope of $-0.3^{+0.3}_{-0.3}$. On the other hand, the protocluster with a merged BCG is better-fit by a single power-law. Thus if SPT2349–56 is to follow a similar trajectory as the $z = 1$ galaxy clusters, then it must accrete numerous less-massive galaxies, or these less-massive galaxies must already be present but remain undetected in our observations. Due to the observational

biases in our sample selection, which targeted star-forming galaxies, we are unable to distinguish between these two scenarios.

We measured the physical sizes of the galaxies in SPT2349–56 in our deep *HST*-F160W data, which probe rest-frame ultraviolet wavelengths. Upon comparing these measurements with typical star-forming galaxies between redshift 4 and 5, we found that our sample has comparable ultraviolet sizes. We stacked our *HST* data at the positions of the detected galaxies and compared this with a stack of the same galaxies at submm wavelengths imaged by ALMA, finding a consistent result. Galaxy C6, the brightest protocluster galaxy in our *HST* data, is the most compact rest-frame ultraviolet source and remains unresolved by our *HST* imaging. Hydrodynamical simulations predict that this galaxy is at the centre of a major merger, yet after the merger the emission will still remain compact.

Lastly, we investigated the total projected stellar and molecular gas mass of SPT2349–56 as a function of projected area. We found that the molecular gas mass and stellar mass track each other well, with no clear trend in the molecular gas-to-stellar mass ratio as a function of radius (the mean value being about 0.3). The stellar mass distribution of SPT2349–56 also does not appear to be markedly different from $z = 1$ galaxy clusters, although we note that so far we have only probed the central ≈ 1 Mpc of the structure, which is much smaller than the extent of $z = 1$ clusters.

SPT2349–56 is a galaxy protocluster in a remarkable phase of its evolution, reaching a total SFR of over $10,000 M_{\odot} \text{ yr}^{-1}$ within a volume of approximately 0.1 Mpc^3 . Having been selected specifically for its star-forming properties, it is interesting that at optical and infrared wavelengths, the galaxies making up SPT2349–56 are not very luminous and have fairly typical stellar masses, highlighting the importance of submm and mm target selection. Galaxy C6 is however an exception; this source is at the centre of a massive merger of over 20 galaxies, and is a likely proto-BCG. The transition of galaxy C6 into a BCG is consistent with the ‘downsizing’ scenario of galaxy formation, and provides a direct observation of the constituents and formation mechanism of a BCG in the early Universe.

ACKNOWLEDGEMENTS

This paper makes use of the following ALMA data: ADS/JAO.ALMA#2017.1.00273.S; and ADS/JAO.ALMA#2018.1.00058.S. ALMA is a partnership of ESO (representing its member states), NSF (USA) and NINS (Japan), together with NRC (Canada), MOST and ASIAA (Taiwan), and KASI (Republic of Korea), in cooperation with the Republic of Chile. The Joint ALMA Observatory is operated by ESO, AUI/NRAO, and NAOJ. *Herschel* is an ESA space observatory with science instruments provided by European-led Principal Investigator consortia and with important participation from NASA. This paper is based on observations made with ESO Telescopes at the La Silla Paranal Observatory under programme ID 299.A-5045(A). The National Radio Astronomy Observatory is a facility of the National Science Foundation operated under cooperative agreement by Associated Universities, Inc. The SPT is supported by the National Science Foundation through grant PLR-1248097, with partial support through PHY-1125897, the Kavli Foundation, and the Gordon and Betty Moore Foundation grant GBMF 947. This work was supported by the Natural Sciences and Engineering Research Council of Canada. The Flatiron Institute is supported by the Simons Foundation. M.A. has been supported by the grant “CONICYT+PCI+REDES 190194”. D.P.M., J.D.V., K.C.L., and K.P. acknowledge support from the US NSF under grants AST-

1715213 and AST-1716127. K.C.L. acknowledges support from the US NSF NRAO under grants SOSPAS-001 and SOSPAS-007, respectively. J.D.V. acknowledges support from an A. P. Sloan Foundation Fellowship. M.A. and J.D.V. acknowledge support from the Center for AstroPhysical Surveys at the National Center for Supercomputing Applications in Urbana, IL. The authors wish to thank Dr. Adam Muzzin for a useful discussion about the stellar mass function of galaxy clusters around redshift 1. S.J. acknowledges support from the US NSF NRAO under grants SOSPAS-001 and SOSPAS-006.

DATA AVAILABILITY

All of the data presented in this paper are publicly available. The *HST* data can be found under the programme 15701 (PI S. Chapman), the *Spitzer*-IRAC data can be found under the four programmes 60194 (PI J. Vieira), 80032 (PI S. Stanford), 13224 (PI S. Chapman), and 14216 (PI S. Chapman), the Gemini-South data can be found under the programme GS-2017B-Q-7 (PI A. Chapman), and the ALMA data can be found under the two programmes 2017.1.00273.S (PI S. Chapman) and 2018.1.00058.S (PI S. Chapman).

REFERENCES

- Alberts S., et al., 2021, *MNRAS*, 501, 1970
 Andreon S., Newman A. B., Trinchieri G., Raichoor A., Ellis R. S., Treu T., 2014, *A&A*, 565, A120
 Aravena M., et al., 2016, *MNRAS*, 457, 4406
 Bai L., et al., 2014, *ApJ*, 789, 134
 Barbosa C. E., Arnaboldi M., Coccato L., Hilker M., Mendes de Oliveira C., Richtler T., 2016, *A&A*, 589, A139
 Barro G., et al., 2016, *ApJ*, 827, L32
 Beroiz M., Cabral J. B., Sanchez B., 2020, *Astronomy and Computing*, 32, 100384
 Bertin E., Arnouts S., 1996, *A&AS*, 117, 393
 Béthermin M., et al., 2020, *A&A*, 643, A2
 Birkin J. E., et al., 2021, *MNRAS*, 501, 3926
 Biviano A., 1998, in Mazure A., Casoli F., Durret F., Gerbal D., eds, *Untangling Coma Berenices: A New Vision of an Old Cluster*. p. 1 ([arXiv:astro-ph/9711251](https://arxiv.org/abs/astro-ph/9711251))
 Bleem L. E., et al., 2015, *ApJS*, 216, 27
 Boquien M., Burgarella D., Roehly Y., Buat V., Ciesla L., Corre D., Inoue A. K., Salas H., 2019, *A&A*, 622, A103
 Boselli A., Cortese L., Boquien M., Boissier S., Catinella B., Gavazzi G., Lagos C., Saintonge A., 2014, *A&A*, 564, A67
 Bothwell M. S., et al., 2017, *MNRAS*, 466, 2825
 Burgarella D., Buat V., Iglesias-Páramo J., 2005, *MNRAS*, 360, 1413
 Bykov A. M., Churazov E. M., Ferrari C., Forman W. R., Kaastra J. S., Klein U., Markevitch M., de Plaa J., 2015, *Space Sci. Rev.*, 188, 141
 Cañameras R., et al., 2015, *A&A*, 581, A105
 Calzetti D., Armus L., Bohlin R. C., Kinney A. L., Koornneef J., Storchi-Bergmann T., 2000, *ApJ*, 533, 682
 Casey C. M., et al., 2015, *ApJ*, 808, L33
 Castignani G., et al., 2020, *A&A*, 640, A64
 Chabrier G., 2003, *PASP*, 115, 763
 Chapman S. C., Blain A. W., Smail I., Ivison R. J., 2005, *ApJ*, 622, 772
 Chapman S. C., Blain A., Ivison R. J., Smail I., Morrison G., 2009, *ApJ*, 691, 560
 Chiang Y.-K., et al., 2015, *ApJ*, 808, 37
 Cochrane R. K., et al., 2019, *MNRAS*, 488, 1779
 Collins C. A., et al., 2009, *Nature*, 458, 603
 Cooke K. C., Kartaltepe J. S., Tyler K. D., Darvish B., Casey C. M., Le Fèvre O., Salvato M., Scoville N., 2019, *ApJ*, 881, 150
 Cowie L. L., Songaila A., Hu E. M., Cohen J. G., 1996, *AJ*, 112, 839

- Cybulski R., et al., 2016, *MNRAS*, **459**, 3287
- Dannerbauer H., et al., 2014, *A&A*, **570**, A55
- De Lucia G., Blaizot J., 2007, *MNRAS*, **375**, 2
- Dessauges-Zavadsky M., et al., 2020, *A&A*, **643**, A5
- Dey A., Lee K.-S., Reddy N., Cooper M., Inami H., Hong S., Gonzalez A. H., Jannuzi B. T., 2016, *ApJ*, **823**, 11
- Draine B. T., et al., 2014, *ApJ*, **780**, 172
- Dunlop J. S., et al., 2017, *MNRAS*, **466**, 861
- Edwards L. O. V., et al., 2020, *MNRAS*, **491**, 2617
- Eikenberry S. S., et al., 2004, in Moorwood A. F. M., Iye M., eds, Society of Photo-Optical Instrumentation Engineers (SPIE) Conference Series Vol. 5492, Ground-based Instrumentation for Astronomy. pp 1196–1207, doi:10.1117/12.549796
- Elbaz D., et al., 2011, *A&A*, **533**, A119
- Everett W. B., et al., 2020, *ApJ*, **900**, 55
- Faisst A. L., et al., 2020, *ApJS*, **247**, 61
- Flores-Cacho I., et al., 2016, *A&A*, **585**, A54
- Fujimoto S., et al., 2020, *ApJ*, **900**, 1
- Galametz A., et al., 2013, *A&A*, **559**, A2
- Geach J. E., Smail I., Coppin K., Moran S. M., Edge A. C., Ellis R. S., 2009, *MNRAS*, **395**, L62
- Geach J. E., Smail I., Moran S. M., MacArthur L. A., Lagos C. d. P., Edge A. C., 2011, *ApJ*, **730**, L19
- Giodini S., Lovisari L., Pointecouteau E., Ettori S., Reiprich T. H., Hoekstra H., 2013, *Space Sci. Rev.*, **177**, 247
- Gobat R., et al., 2011, *A&A*, **526**, A133
- Goldader J. D., Meurer G., Heckman T. M., Seibert M., Sanders D. B., Calzetti D., Steidel C. C., 2002, *ApJ*, **568**, 651
- Greenslade J., et al., 2018, *MNRAS*, **476**, 3336
- Grogin N. A., et al., 2011, *ApJS*, **197**, 35
- Harikane Y., et al., 2019, *ApJ*, **883**, 142
- Hayashi M., et al., 2018, *ApJ*, **856**, 118
- Hayward C. C., Jonsson P., Kereš D., Magnelli B., Hernquist L., Cox T. J., 2012, *MNRAS*, **424**, 951
- Hayward C. C., Narayanan D., Kereš D., Jonsson P., Hopkins P. F., Cox T. J., Hernquist L., 2013, *MNRAS*, **428**, 2529
- Hezaveh Y. D., et al., 2013, *ApJ*, **767**, 132
- Hill R., et al., 2020, *MNRAS*, **495**, 3124
- Hilton M., et al., 2013, *MNRAS*, **435**, 3469
- Hook I. M., Jørgensen I., Allington-Smith J. R., Davies R. L., Metcalfe N., Murowinski R. G., Crampton D., 2004, *PASP*, **116**, 425
- Huang N., et al., 2020, *AJ*, **159**, 110
- Hung C.-L., et al., 2016, *ApJ*, **826**, 130
- Ivison R. J., et al., 2007, *MNRAS*, **380**, 199
- Jablonka P., Combes F., Rines K., Finn R., Welch T., 2013, *A&A*, **557**, A103
- Kennicutt Jr. R. C., 1998, *ARA&A*, **36**, 189
- Khochfar S., Silk J., 2006, *ApJ*, **648**, L21
- Khusanova Y., et al., 2020, arXiv e-prints, p. arXiv:2007.08384
- Kneissl R., et al., 2019, *A&A*, **625**, A96
- Koyama Y., et al., 2020, arXiv e-prints, p. arXiv:2008.13614
- Lacaille K. M., et al., 2019, *MNRAS*, **488**, 1790
- Lang P., et al., 2019, *ApJ*, **879**, 54
- Le Fèvre O., et al., 2020, *A&A*, **643**, A1
- Lim S., Scott D., Babul A., Barnes D. J., Kay S. T., McCarthy I. G., Rennehan D., Vogelsberger M., 2021, *MNRAS*, **501**, 1803
- Lin L., et al., 2010, *ApJ*, **718**, 1158
- Liu F. S., Mao S., Deng Z. G., Xia X. Y., Wen Z. L., 2009, *MNRAS*, **396**, 2003
- Liu F. S., Lei F. J., Meng X. M., Jiang D. F., 2015, *MNRAS*, **447**, 1491
- Lokas E. L., Mamon G. A., 2001, *MNRAS*, **321**, 155
- Long A. S., et al., 2020, arXiv e-prints, p. arXiv:2003.13694
- Magliocchetti M., et al., 2013, *MNRAS*, **433**, 127
- Mantz A. B., et al., 2018, *A&A*, **620**, A2
- Marshall H. L., Tananbaum H., Avni Y., Zamorani G., 1983, *ApJ*, **269**, 35
- Martinache C., et al., 2018, *A&A*, **620**, A198
- Matharu J., et al., 2019, *MNRAS*, **484**, 595
- Merlin E., et al., 2015, *A&A*, **582**, A15
- Merlin E., et al., 2016, *A&A*, **595**, A97
- Michałowski M. J., Dunlop J. S., Cirasuolo M., Hjorth J., Hayward C. C., Watson D., 2012, *A&A*, **541**, A85
- Miller T. B., Hayward C. C., Chapman S. C., Behroozi P. S., 2015, *MNRAS*, **452**, 878
- Miller T. B., et al., 2018, *Nature*, **556**, 469
- Mocanu L. M., et al., 2013, *ApJ*, **779**, 61
- Naab T., Johansson P. H., Ostriker J. P., 2009, *ApJ*, **699**, L178
- Negrello M., et al., 2010, *Science*, **330**, 800
- Noble A. G., et al., 2017, *ApJ*, **842**, L21
- Noll S., Burgarella D., Giovannoli E., Buat V., Marcellac D., Muñoz-Mateos J. C., 2009, *A&A*, **507**, 1793
- Oogi T., Habe A., 2012, in Umemura M., Omukai K., eds, American Institute of Physics Conference Series Vol. 1480, First Stars IV - from Hayashi to the Future - pp 406–408 (arXiv:1208.5039), doi:10.1063/1.4754402
- Oteo I., et al., 2018, *ApJ*, **856**, 72
- Overzier R. A., 2016, *A&ARv*, **24**, 14
- Peng C. Y., Ho L. C., Impey C. D., Rix H.-W., 2002, *AJ*, **124**, 266
- Peng C. Y., Ho L. C., Impey C. D., Rix H.-W., 2010, *AJ*, **139**, 2097
- Planck Collaboration I 2020, *A&A*, **641**, A1
- Planck Collaboration XXVII 2015, *A&A*, **582**, A30
- Planck Collaboration XXVII 2016, *A&A*, **594**, A27
- Rennehan D., Babul A., Hayward C. C., Bottrell C., Hani M. H., Chapman S. C., 2020, *MNRAS*, **493**, 4607
- Rosati P., et al., 2009, *A&A*, **508**, 583
- Rotermund K. M., et al., 2021, *MNRAS*, **502**, 1797
- Schreiber C., et al., 2015, *A&A*, **575**, A74
- Scott T. C., Usero A., Brinks E., Boselli A., Cortese L., Bravo-Alfaro H., 2013, *MNRAS*, **429**, 221
- Scoville N., et al., 2016, *ApJ*, **820**, 83
- Shimasaku K., et al., 2003, *ApJ*, **586**, L111
- Simpson J. M., et al., 2014, *ApJ*, **788**, 125
- Simpson J. M., et al., 2015, *ApJ*, **799**, 81
- Speagle J. S., Steinhardt C. L., Capak P. L., Silverman J. D., 2014, *ApJS*, **214**, 15
- Sperone-Longin D., et al., 2021, *A&A*, **647**, A156
- Spilker J. S., et al., 2014, *ApJ*, **785**, 149
- Spilker J. S., et al., 2016, *ApJ*, **826**, 112
- Steidel C. C., Adelberger K. L., Shapley A. E., Pettini M., Dickinson M., Giavalisco M., 2000, *ApJ*, **532**, 170
- Steidel C. C., Adelberger K. L., Shapley A. E., Erb D. K., Reddy N. A., Pettini M., 2005, *ApJ*, **626**, 44
- Swinbank A. M., et al., 2010, *MNRAS*, **405**, 234
- Swinbank A. M., et al., 2014, *MNRAS*, **438**, 1267
- Tacconi L. J., et al., 2018, *ApJ*, **853**, 179
- Tadaki K.-i., et al., 2019, *PASJ*, **71**, 40
- Tamura Y., et al., 2009, *Nature*, **459**, 61
- Umehata H., et al., 2015, *ApJ*, **815**, L8
- Venemans B. P., et al., 2007, *A&A*, **461**, 823
- Vieira J. D., et al., 2010, *ApJ*, **719**, 763
- Wall J. V., Pope A., Scott D., 2008, *MNRAS*, **383**, 435
- Wang T., et al., 2016, *ApJ*, **828**, 56
- Wang T., et al., 2018, *ApJ*, **867**, L29
- Wang G., et al., 2020, arXiv e-prints, p. arXiv:2010.02909
- Whitney A., Conselice C. J., Bhatavdekar R., Duncan K., 2019, *ApJ*, **887**, 113
- Wilkinson A., et al., 2017, *MNRAS*, **464**, 1380
- Young L. M., et al., 2011, *MNRAS*, **414**, 940
- Zabel N., et al., 2019, *MNRAS*, **483**, 2251
- Zhu Y.-N., Wu H., Li H.-N., Cao C., 2010, *Research in Astronomy and Astrophysics*, **10**, 329
- da Cunha E., et al., 2015, *ApJ*, **806**, 110
- van Dokkum P. G., et al., 2010, *ApJ*, **709**, 1018
- van der Burg R. F. J., et al., 2013, *A&A*, **557**, A15
- van der Burg R. F. J., Muzzin A., Hoekstra H., Wilson G., Lidman C., Yee H. K. C., 2014, *A&A*, **561**, A79
- van der Burg R. F. J., McGee S., Aussel H., Dahle H., Arnaud M., Pratt G. W., Muzzin A., 2018, *A&A*, **618**, A140

APPENDIX A: OPTICAL COUNTERPART OFFSETS

Positional differences between our rest-frame optical and ALMA positions are defined as the ALMA position minus the optical/infrared position. In Fig. A1 we show the mean offset found in each band surrounded by a circle whose semi-major and semi-minor axes are equal to the standard deviations of the offsets in each direction. We find a slight offset in the negative x direction of $\Delta RA \approx -0.1$ arcsec (consistent across all wavebands, since the astrometry has been tied to a single frame).

APPENDIX B: OPTICAL IMAGING CUTOUTS

In Fig. B1 we show all 32 12×12 arcsec source cutouts from our multiwavelength coverage. This includes GEMINI-GMOS in the g , r , and i bands, GEMINI-FLAMINGOS-2 imaging in the K_s band, *HST* imaging with the F110W and F160W filters, and *Spitzer*-IRAC imaging in ch1 ($3.6 \mu\text{m}$) and ch2 ($4.5 \mu\text{m}$). In each frame, the ALMA position is shown as the blue point, with ALMA 850- μm continuum and [CII] line emission contours overlaid. Positions of sources found using `source_extractor` (or `t-phot` for IRAC) are shown as red crosses, with matched ALMA counterparts circled in green. Panels are blank where we do not have data at a given wavelength for a given source.

APPENDIX C: BEST FIT SEDS

In Fig. C1 we show best-fit SEDs for all galaxies in our sample, obtained from CIGALE using the photometry in Table 1 and in Hill et al. (2020). Detected flux densities are shown as circles, and flux density upper limits are shown as downward-pointing arrows. In these fits we allowed the stellar mass, dust extinction, age, and star-formation timescale to vary. The best-fit stellar masses are provided in Table 2. For galaxies C12, C16, C20, C22, C23, LAE1, and LAE2, only upper limits are available for their photometry across all wavelengths (both submm and optical/infrared), so we do not attempt to fit SEDs or derive stellar masses.

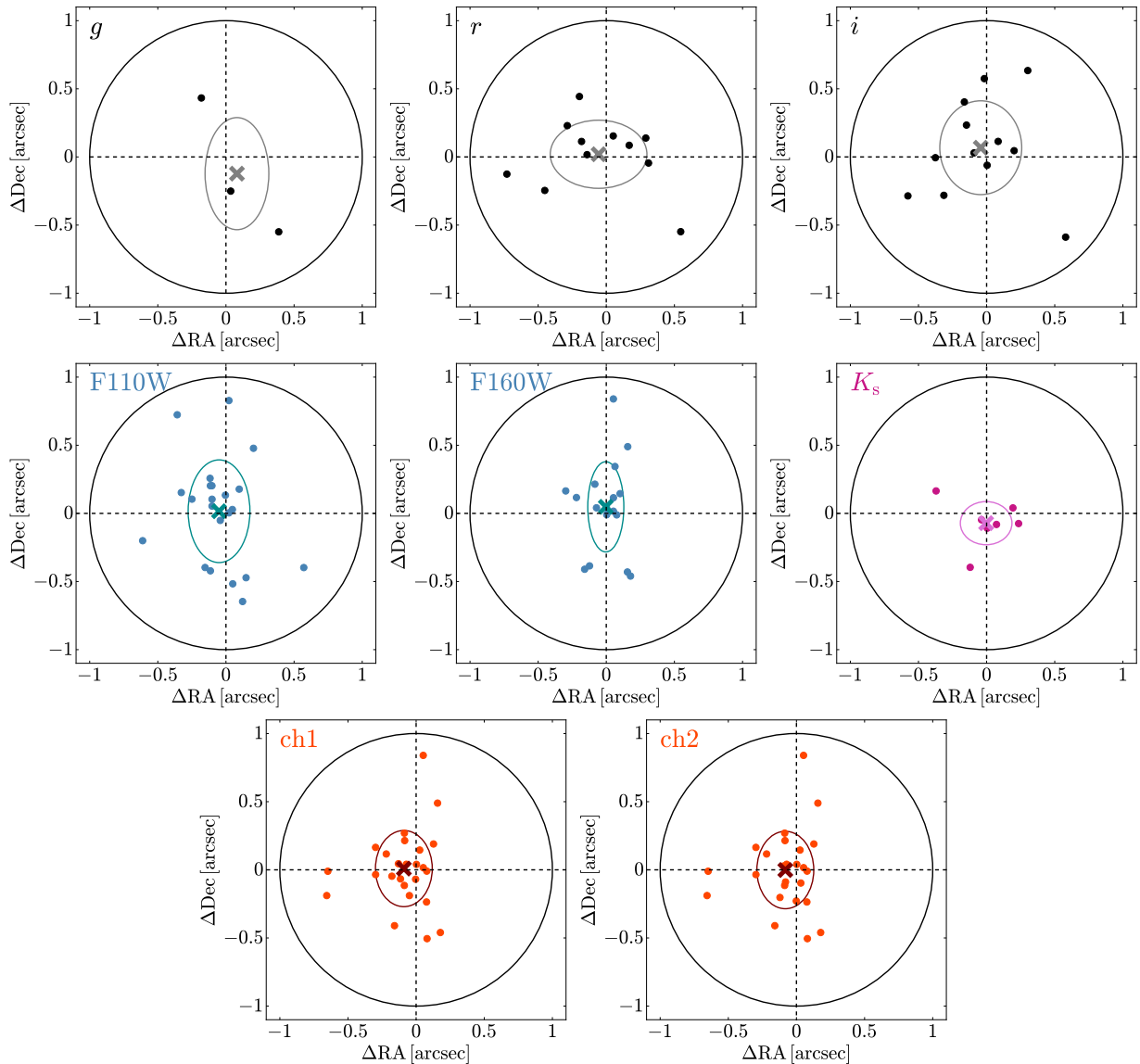


Figure A1. Offset in right ascension and declination between the ALMA positions reported in Hill et al. (2020) and the counterparts identified in each of the bands used in this work. The mean offset in each band is indicated by a cross, surrounded by an ellipse whose semi-major and semi-minor axes are equal to the standard deviation of the offsets in each direction. In each case we find that the ellipse overlaps with the origin, indicating that there are no systematic offset errors present at a significant level in our data.

APPENDIX D: OPTICAL PROFILE FITS

In Fig. D1 we provide rest-frame optical (observed-frame $1.5 \mu\text{m}$) cut-outs of our sources obtained from our *HST* F160W imaging. Sérsic profiles were fit to all sources detected in the images above 3σ , including convolution with the beam, and half-light radii were estimated from the fits.

The left panels show these stacked images with 2 and 3σ contours, then increasing in steps of 3σ , with positions found in the Cycle 5 data shown as blue points and positions found from the Sérsic profiles shown as red points. The red bars indicate the sizes of the half-light radii resulting from the Sérsic profiles, with best-fitting half-light radii and Sérsic indices shown in the top left. For sources NL2, NL3, and N3 we provide the best-fitting half-light radii in units of arcseconds (as the redshifts have not been confirmed), otherwise the best-fitting half-light radii are in units of kiloparsecs. The middle panels show our Sérsic profile models, and the right panels show

the residuals. For sources below 5σ , where we did not attempt to fit Sérsic profiles, we leave the middle panel blank.

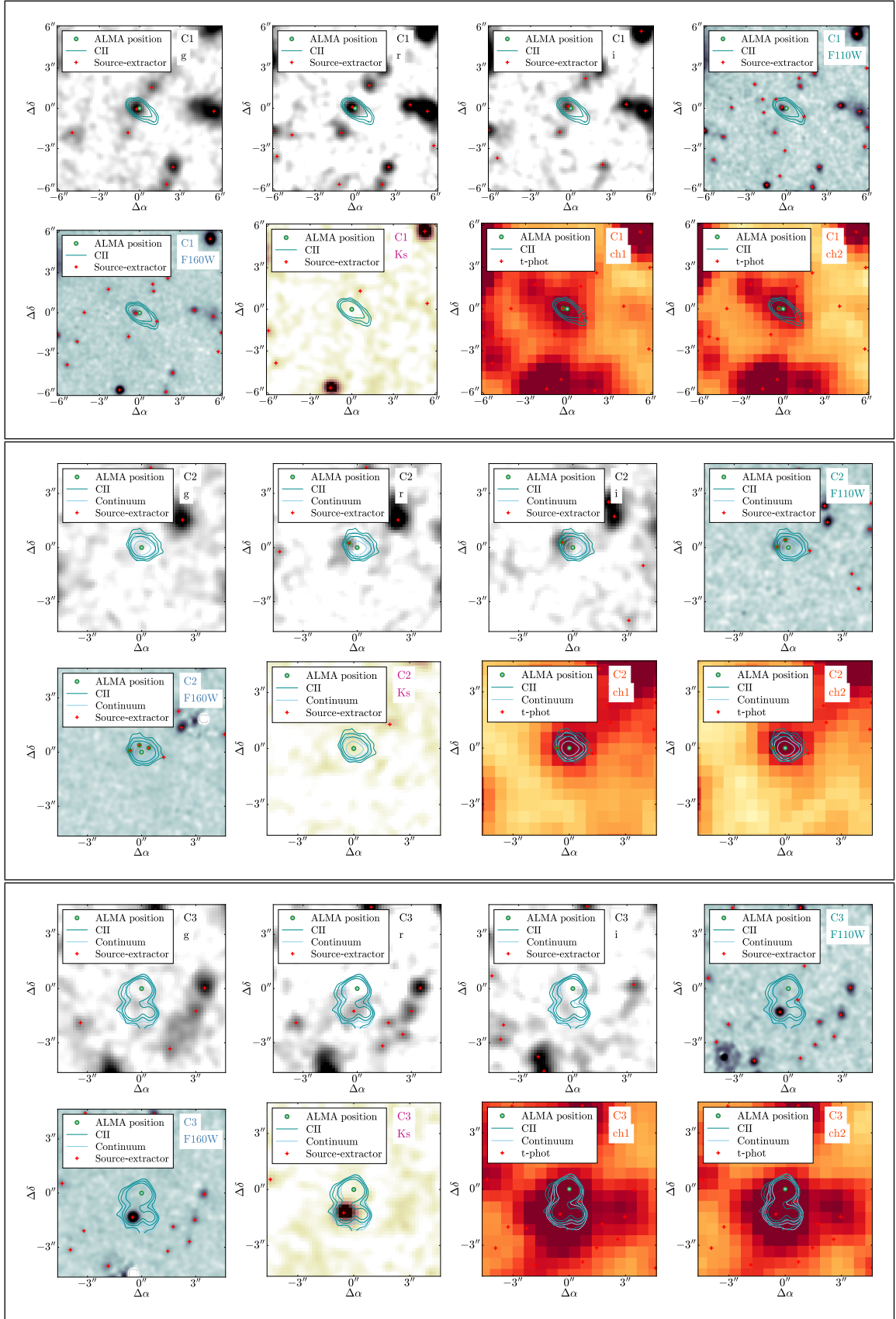


Figure B1. Multiwavelength cutouts for each source in our protocluster sample. In each panel, the ALMA position is shown as the blue point, with ALMA 850- μm continuum and [CII] line emission contours overlaid. Positions of sources found using source-extractor (or t-phot for IRAC) are shown as red crosses, with matched ALMA counterparts as circles in green. *Clockwise, top-left to bottom-right*: GEMINI-GMOS g band; GEMINI-GMOS r band; GEMINI-GMOS i band; *HST*-F110W; *HST*-F160W; GEMINI-FLAMINGOS-2 K_s band; *Spitzer*-IRAC ch1; and *Spitzer*-IRAC ch2. Panels are blank where we do not have data at a given wavelength for a given source.

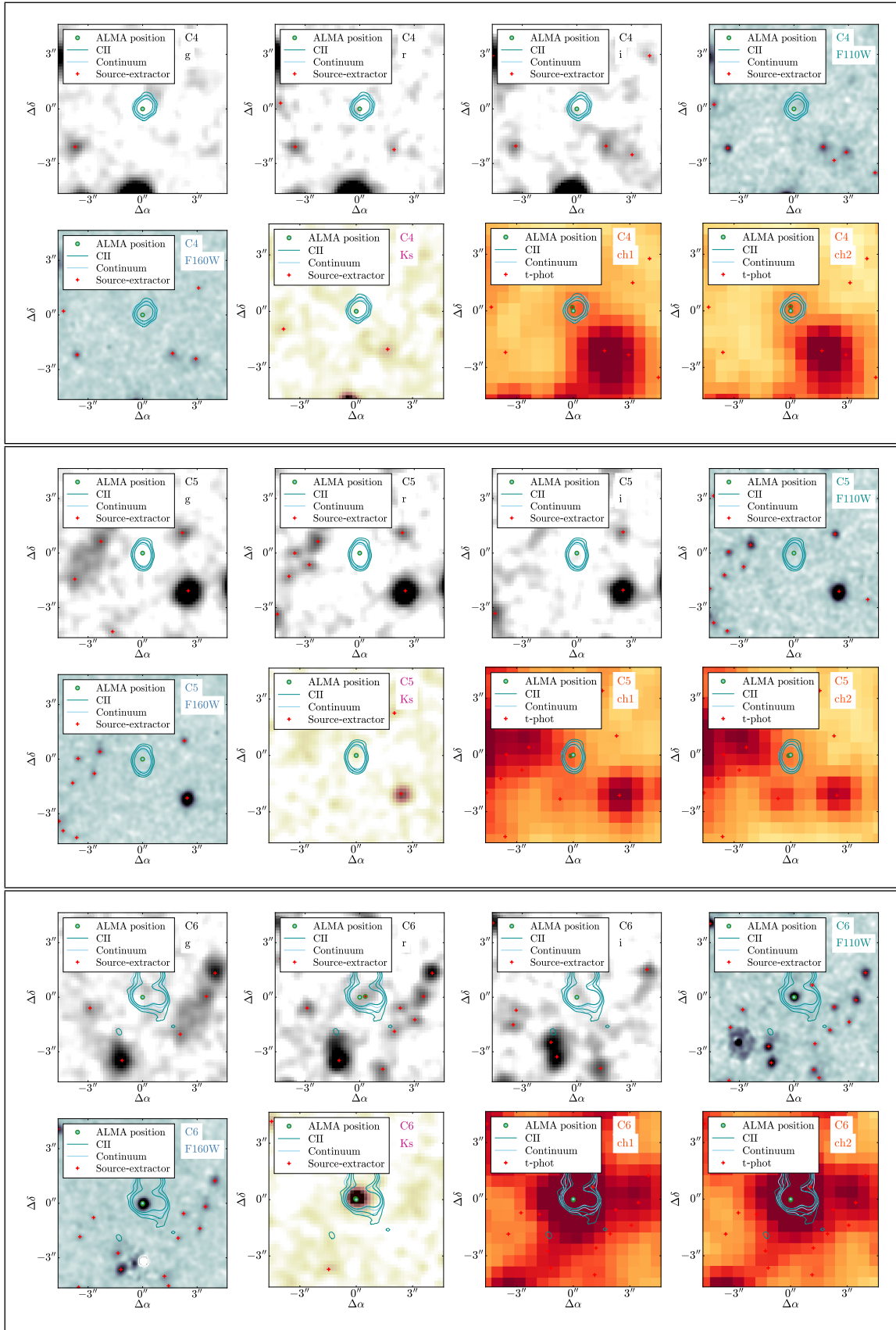


Figure B1 (Cont.).

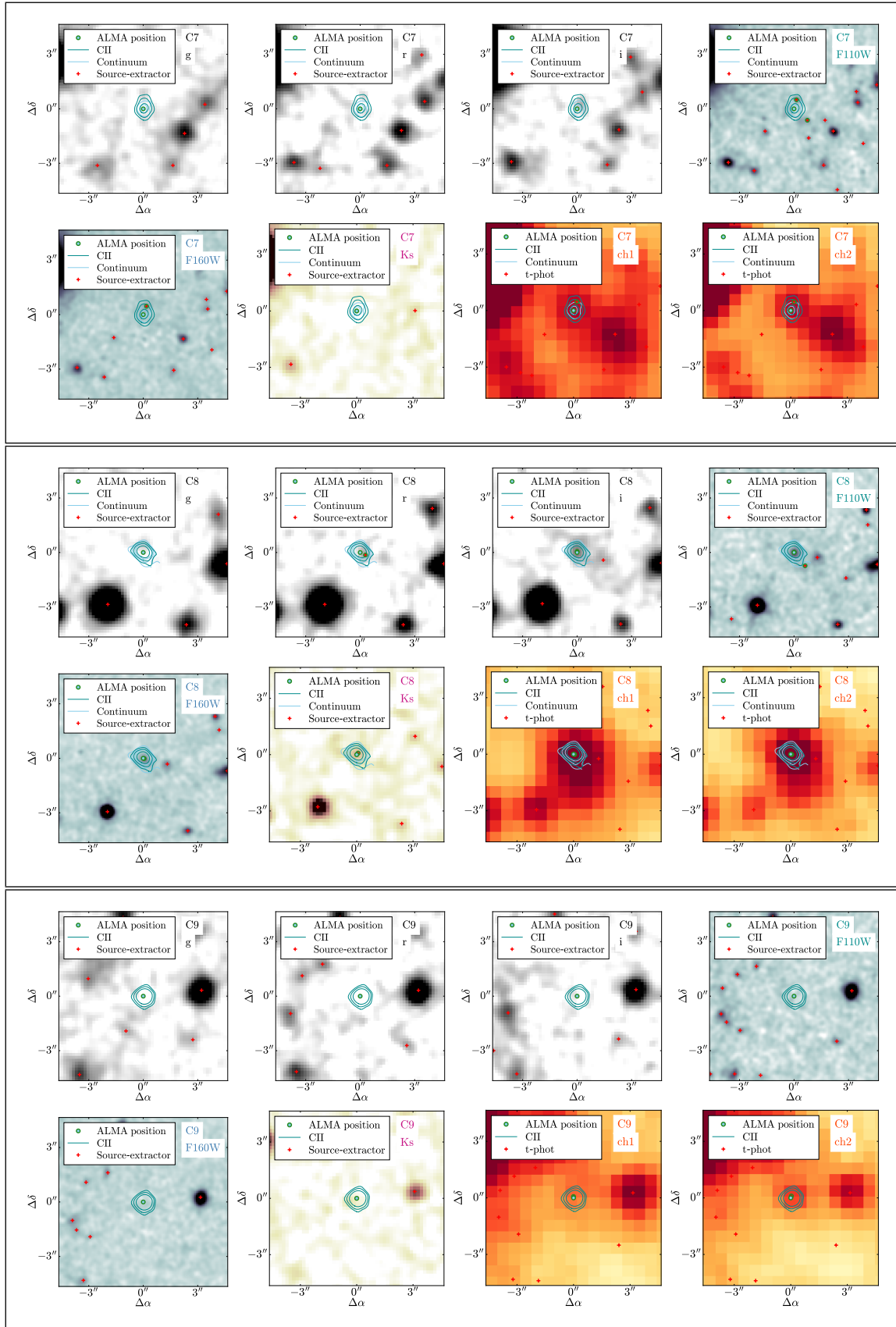


Figure B1 (Cont.).

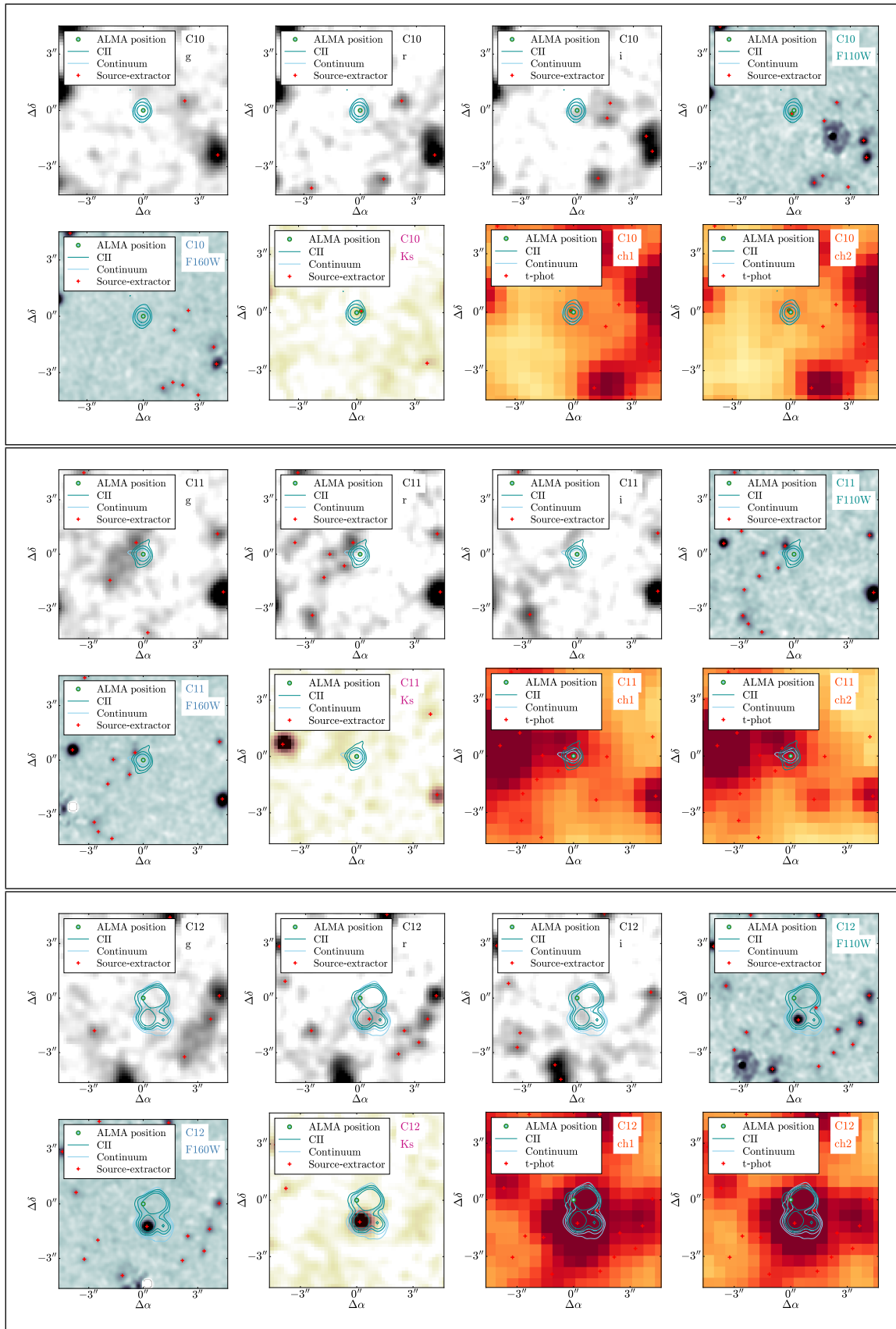


Figure B1 (Cont.).

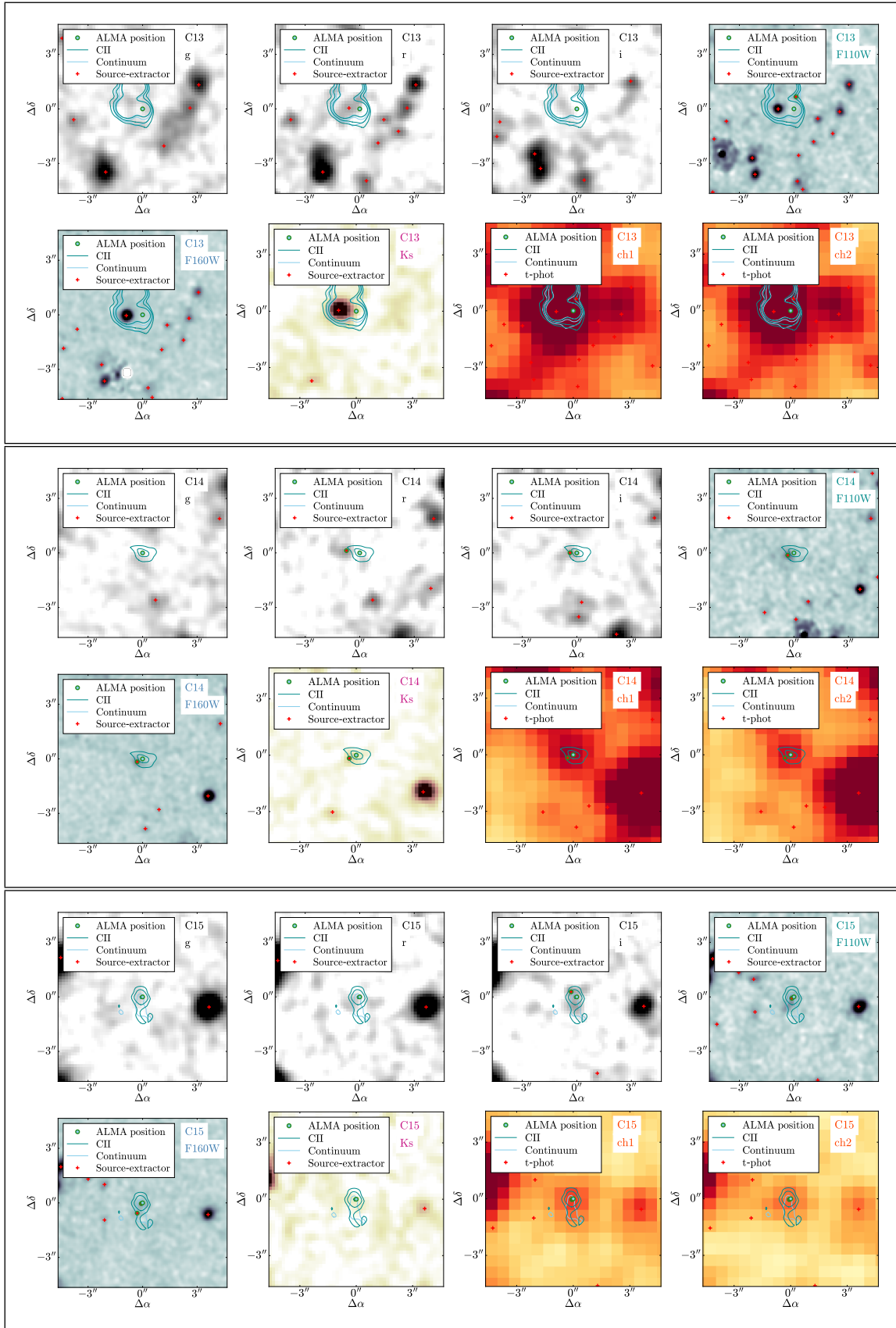


Figure B1 (Cont.).

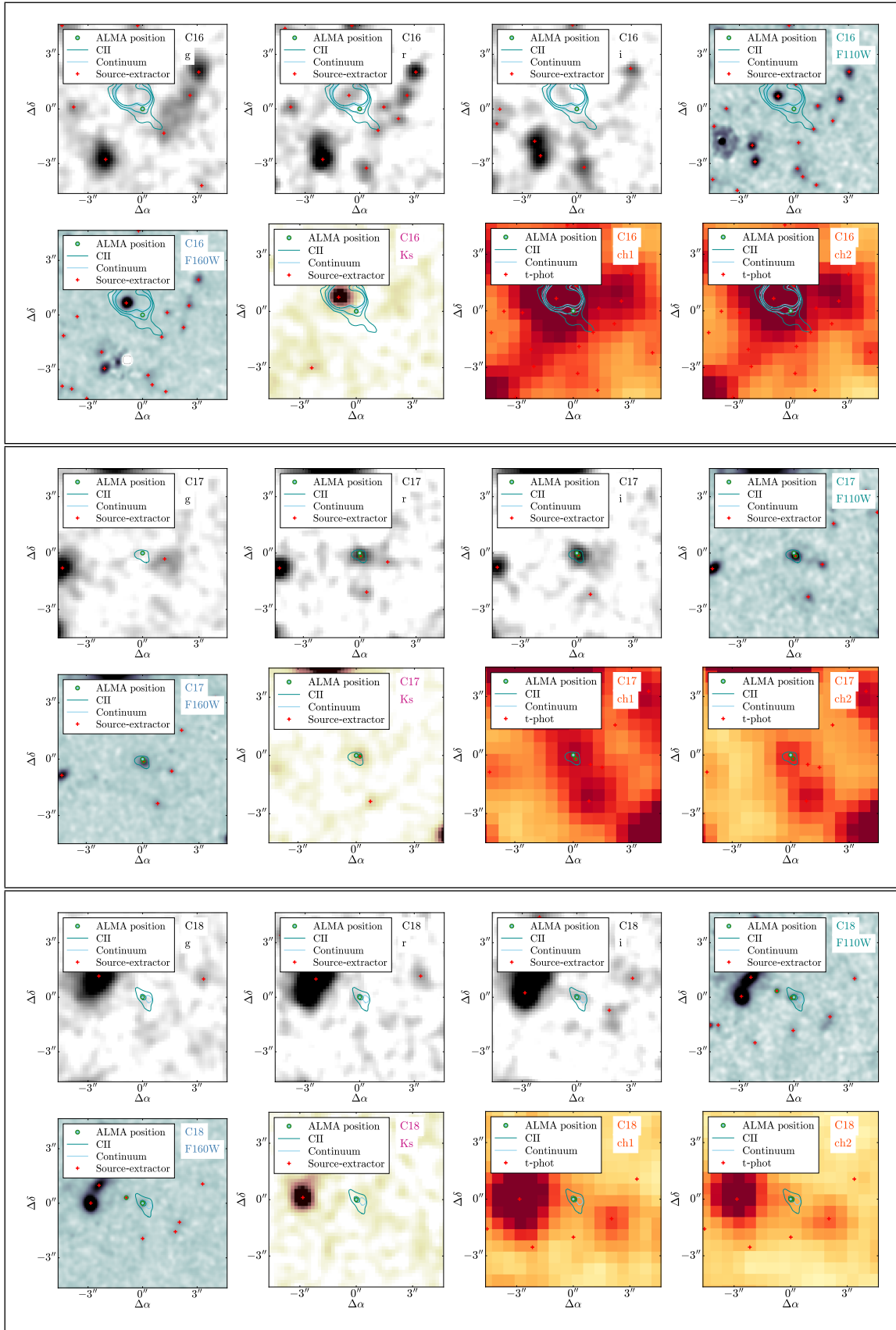


Figure B1 (Cont.).

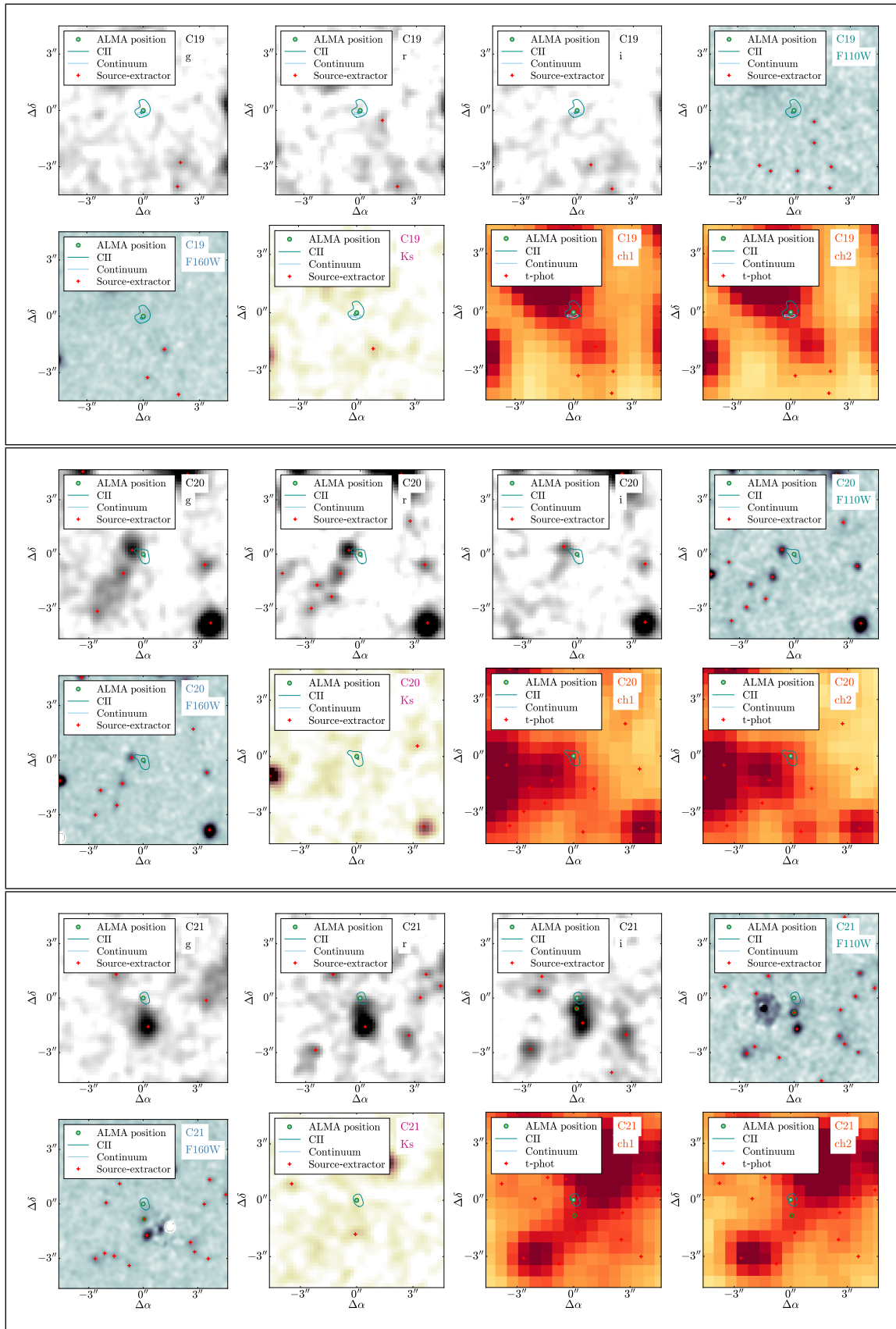


Figure B1 (Cont.).

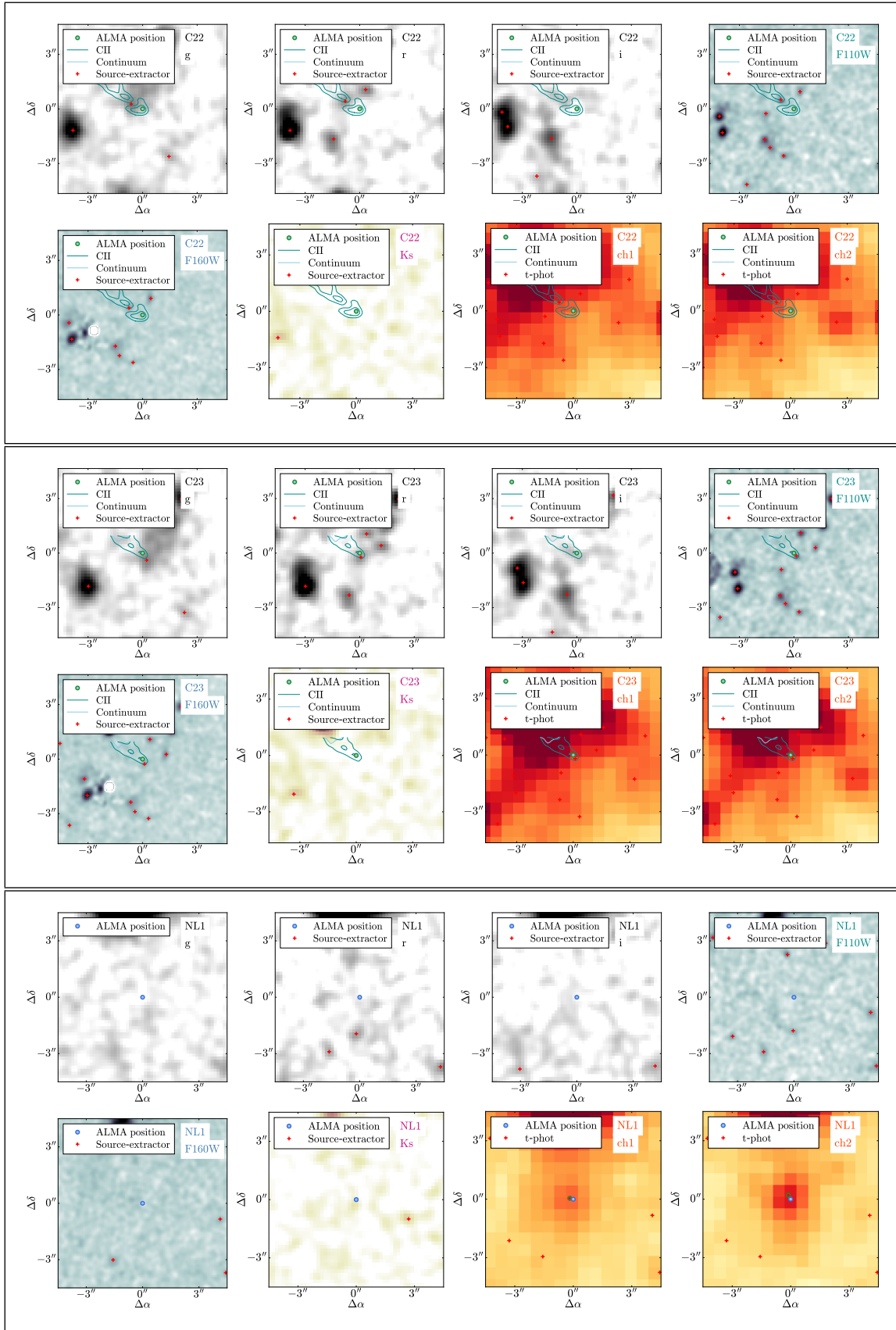


Figure B1 (Cont.).

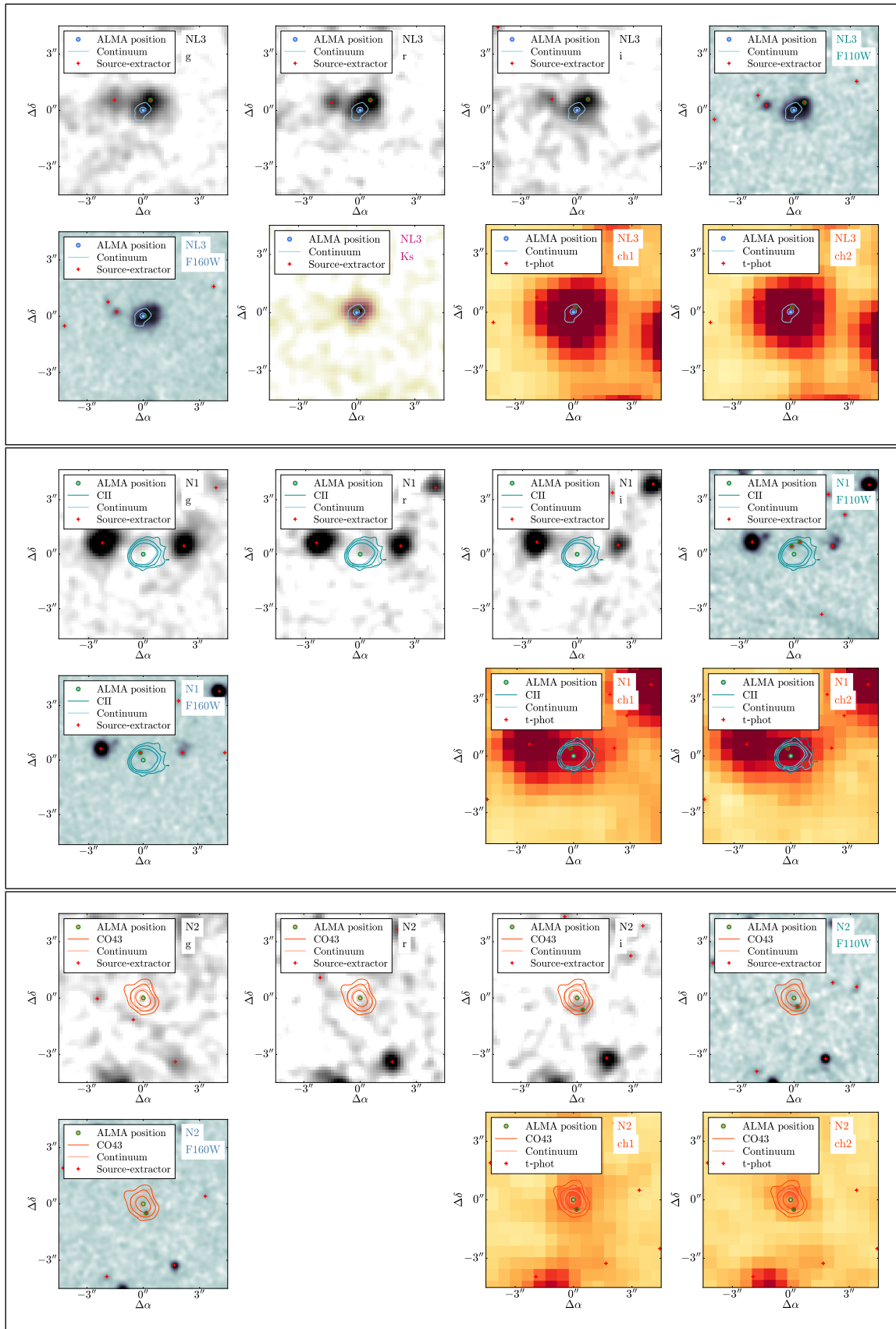


Figure B1 (Cont.).

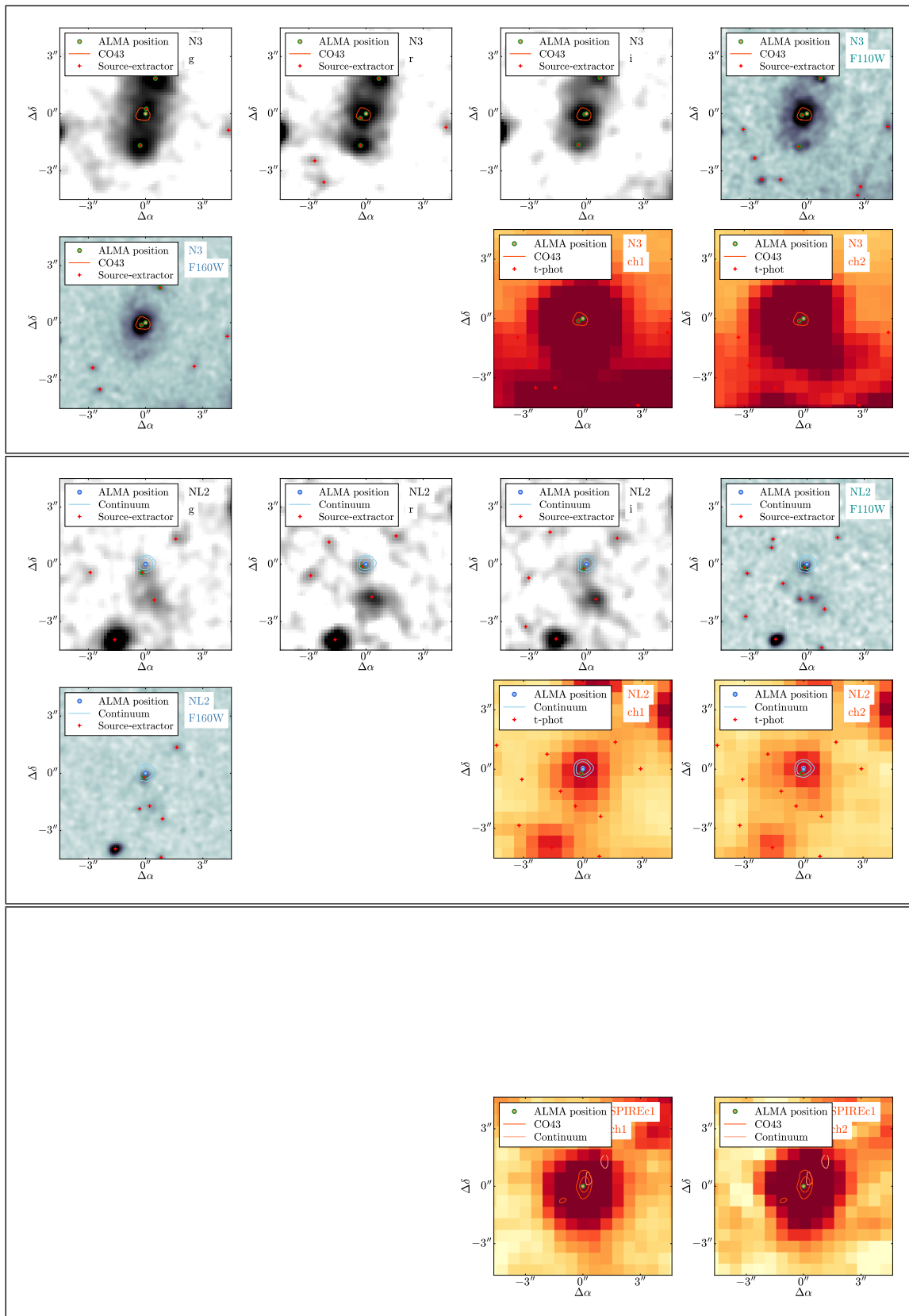


Figure B1 (Cont.).

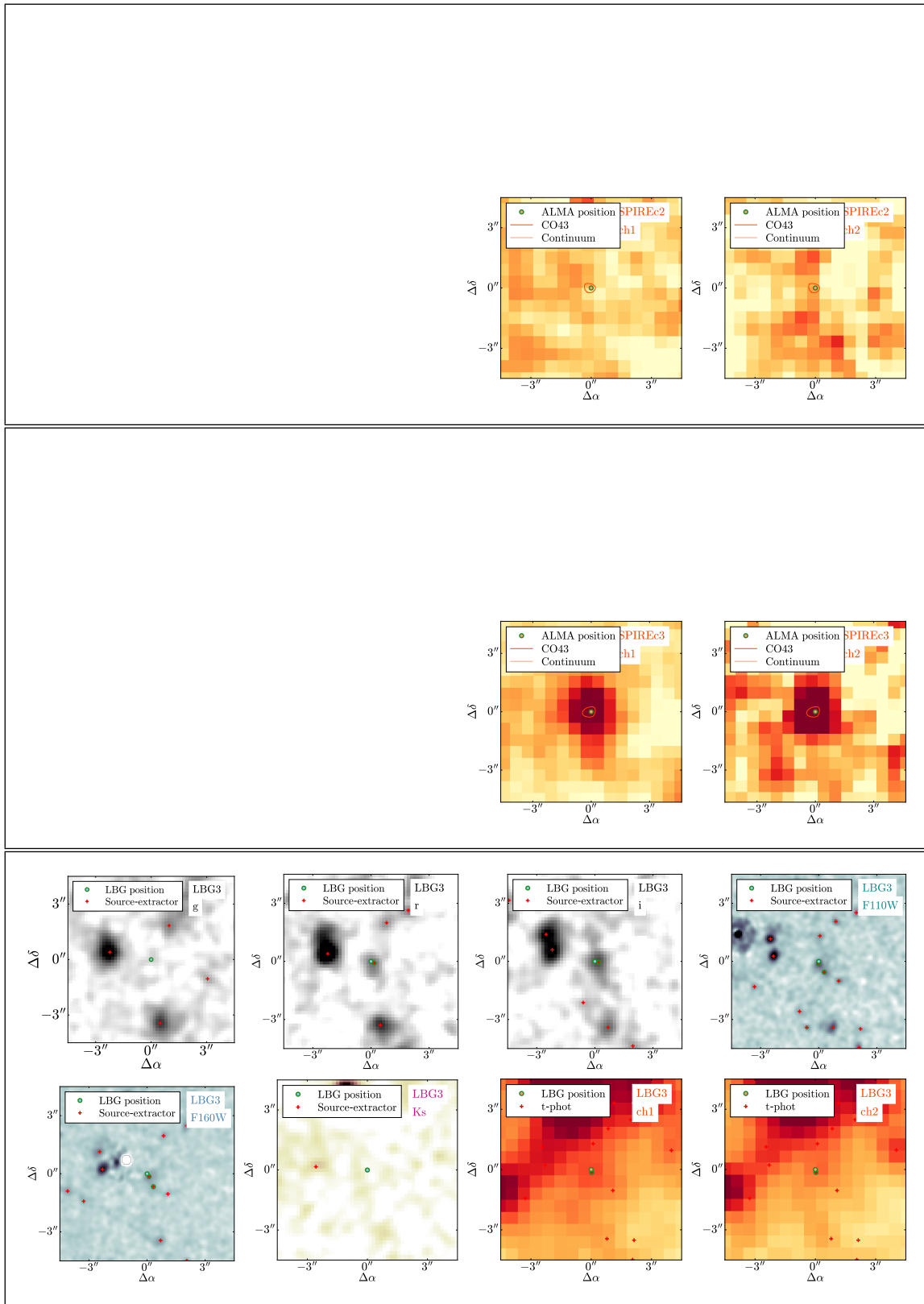


Figure B1 (Cont.).

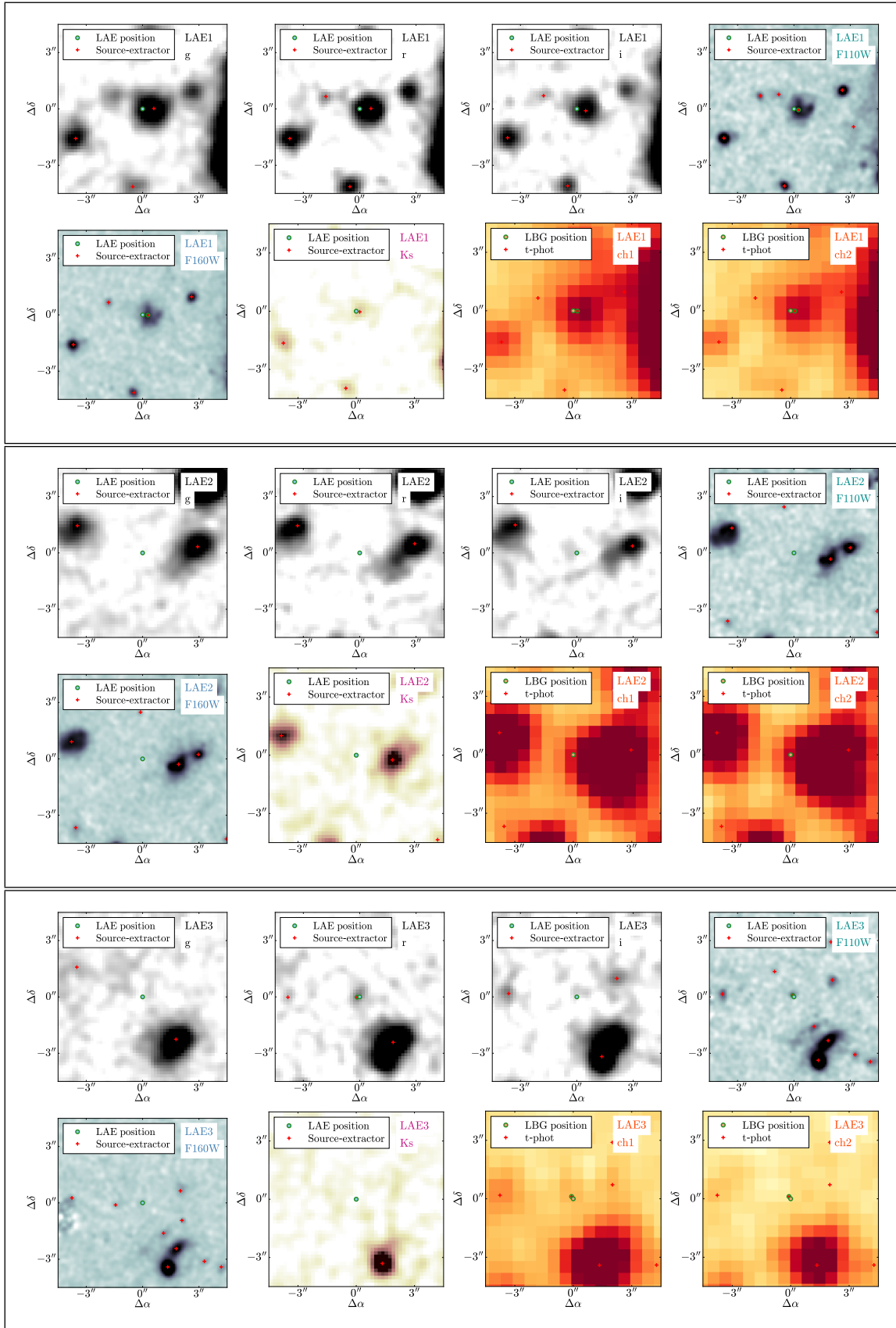


Figure B1 (Cont.).

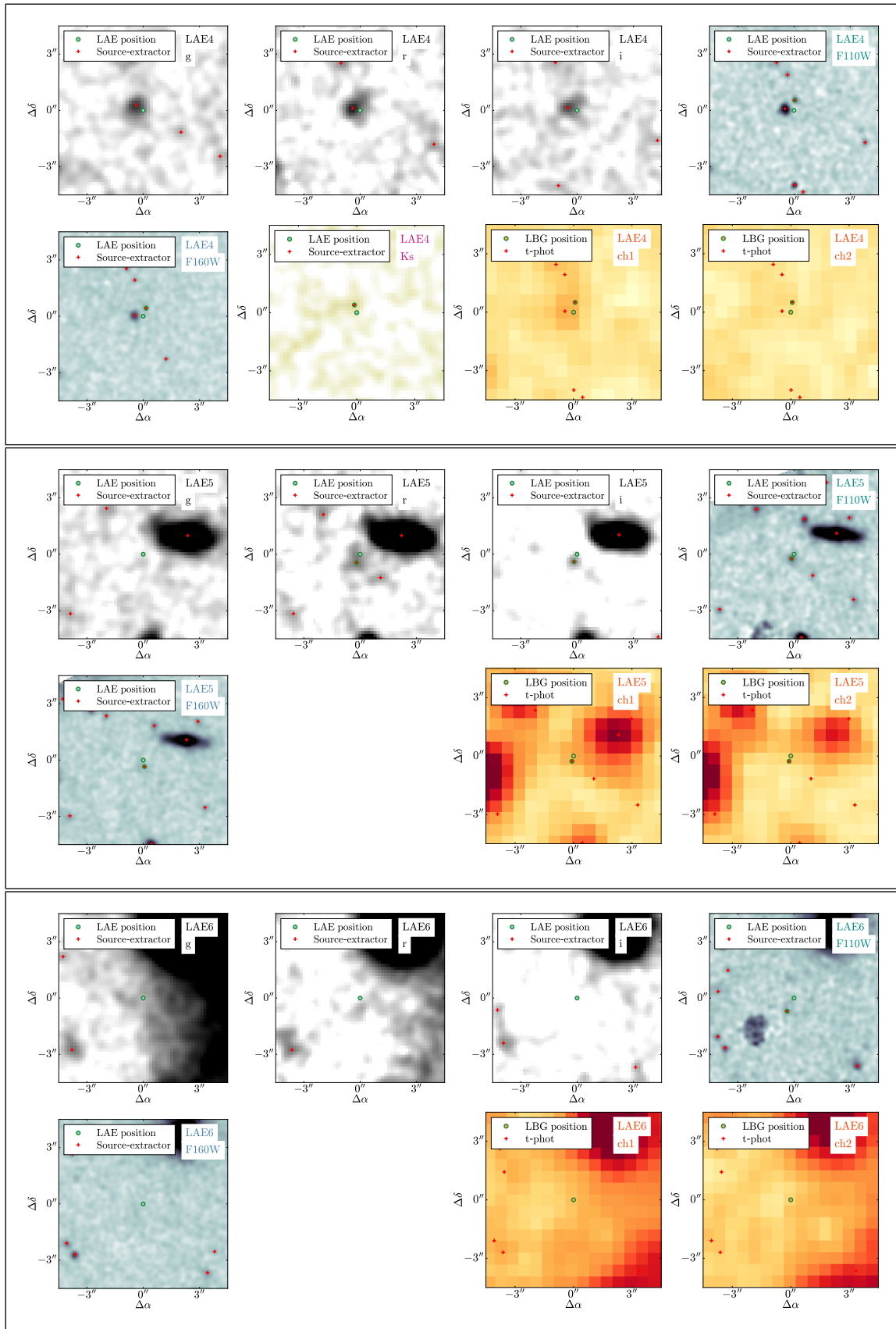


Figure B1 (Cont.).

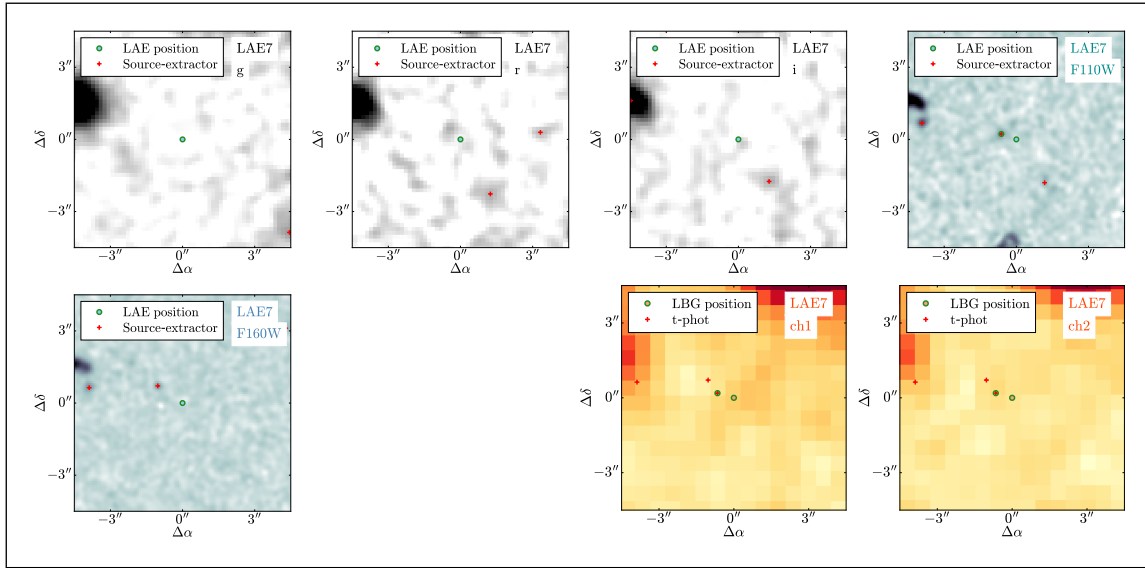


Figure B1 (Cont.).

APPENDIX E: [CII] PROFILE FITS

In Fig. E1 we provide [CII] cut-outs of our sources obtained from the high-resolution ALMA Band 7 imaging. Line-emission channels were determined from our deeper Cycle 5 data by fitting Gaussian profiles to each spectrum (see Hill et al. 2020), and these channels were stacked in the high-resolution data to create moment-0 maps. Sérsic profiles were fit to all sources with pixels detected in the moment-0 maps above 5 times the local rms, taking into account the instrumental PSF by convolving the model with the best-fit synthesized beam, and half-light radii were estimated from the fits.

The left panels show these stacked images with 2 and 3σ contours, then increasing in steps of 3σ , with positions found in the Cycle 5 data shown as blue points and positions found from the Sérsic profiles shown as red points. The red bars indicated the sizes of the half-light radii resulting from the Sérsic profiles, and best-fitting half-light radii in units of kiloparsecs and Sérsic indices are shown in the top left. The middle panels show our Sérsic profile models, and the right panels show the residuals. For sources below 3σ , where we did not attempt to fit Sérsic profiles, we leave the middle panel blank.

This paper has been typeset from a $\text{\TeX}/\text{\LaTeX}$ file prepared by the author.

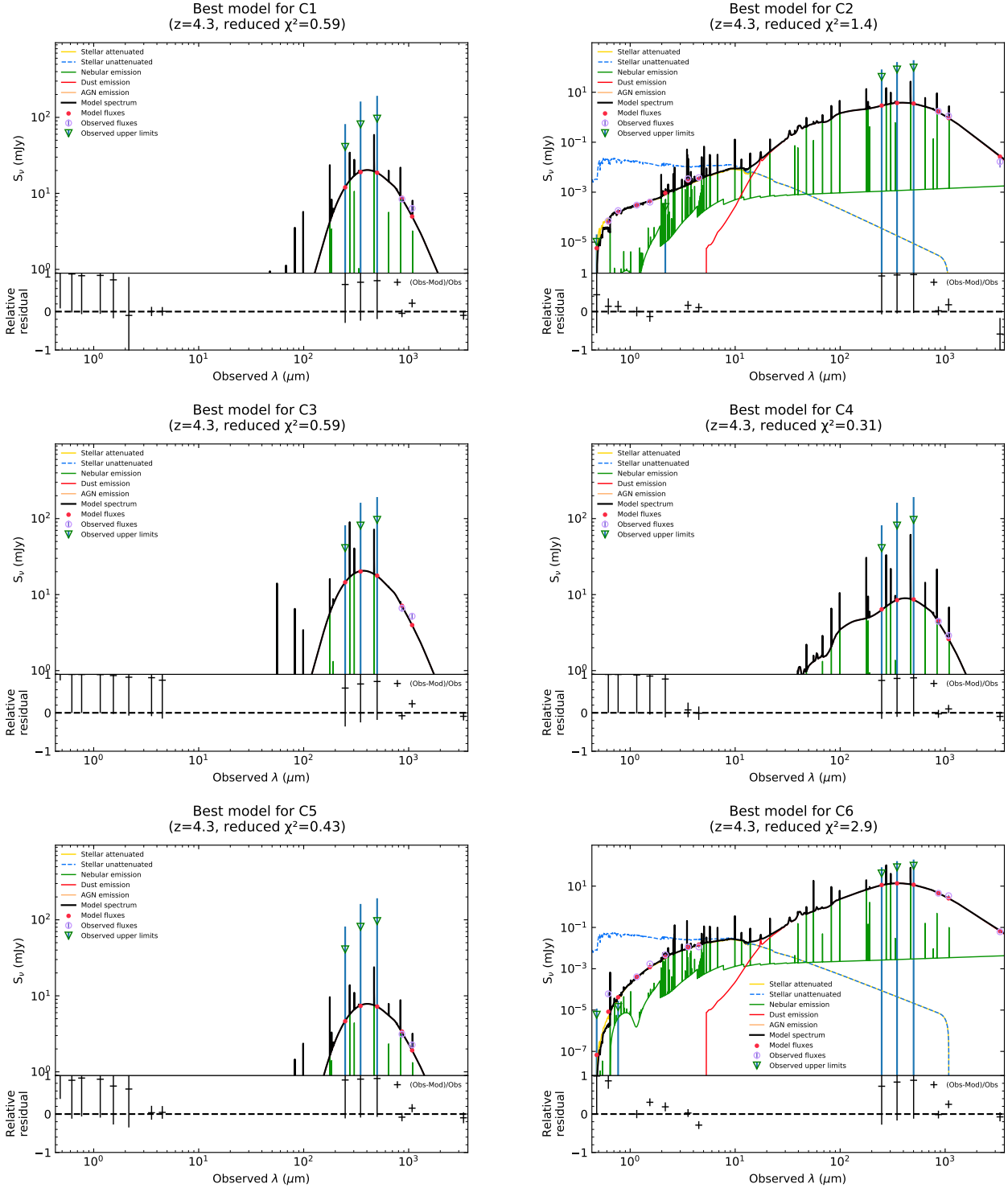
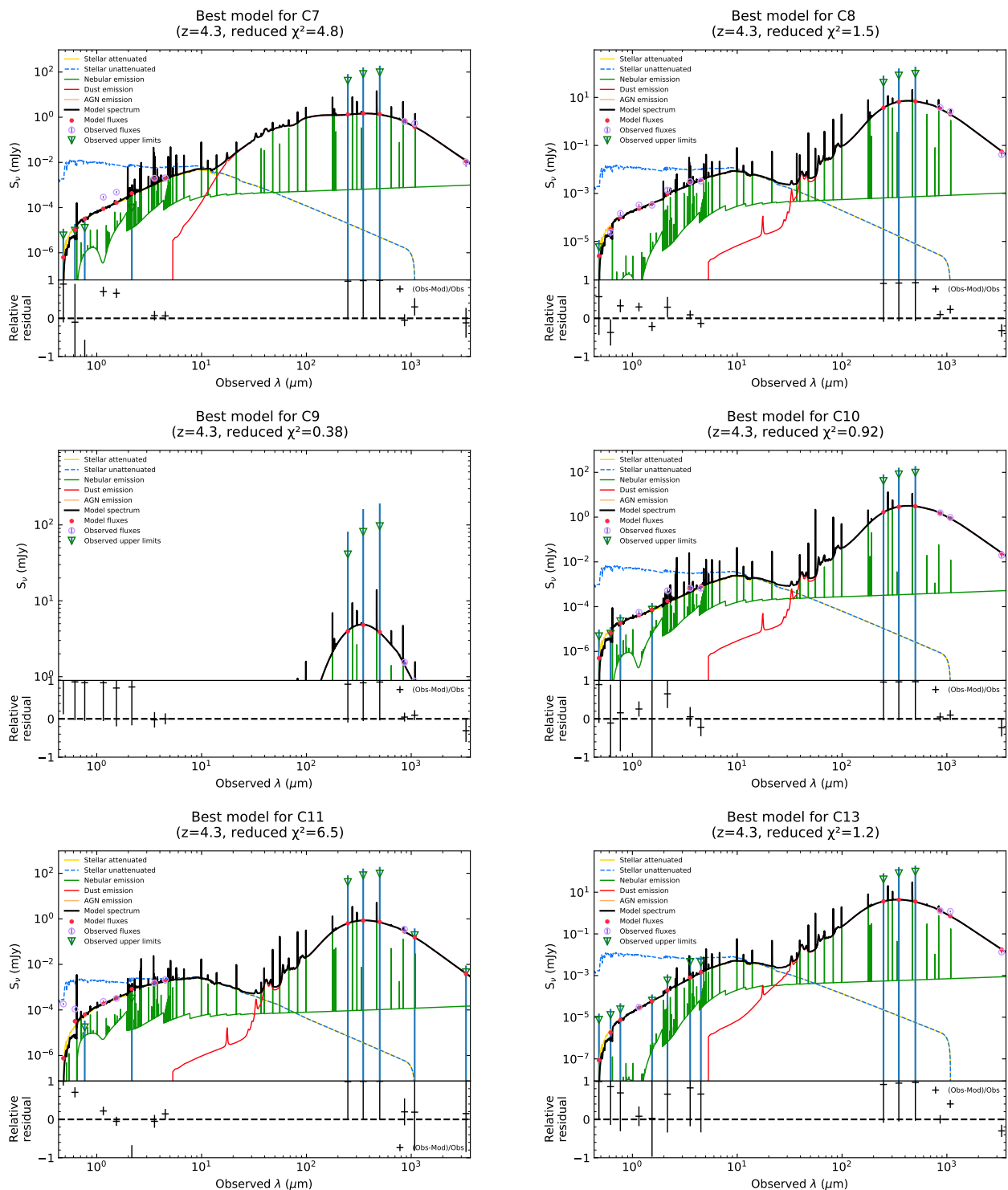
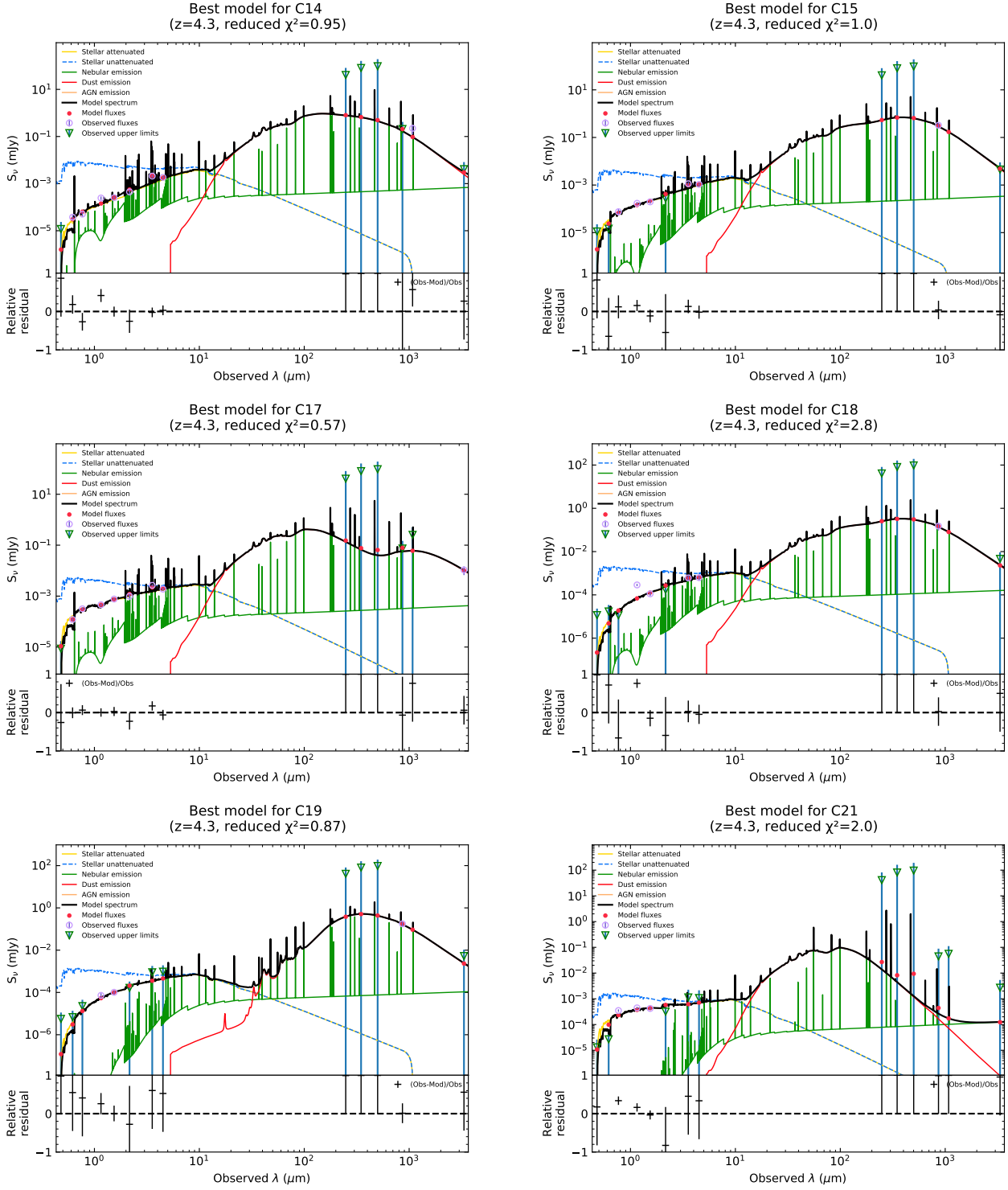


Figure C1. Best-fit SEDs from CIGALE using the photometry in Table 1 and in Hill et al. (2020). Detected flux densities are shown as circles and flux density upper limits are shown as downward-pointing arrows, while flux densities predicted from the SED model are shown as red circles. The total best-fit SED is the black solid line, plotted along with contributions from stellar emission (unattenuated as the blue dashed line, attenuated as the yellow solid line), dust emission (red solid line), AGN emission (orange solid line), and nebular emission containing various strong emission lines (green solid line). Residuals are plotted at the bottom of each panel.





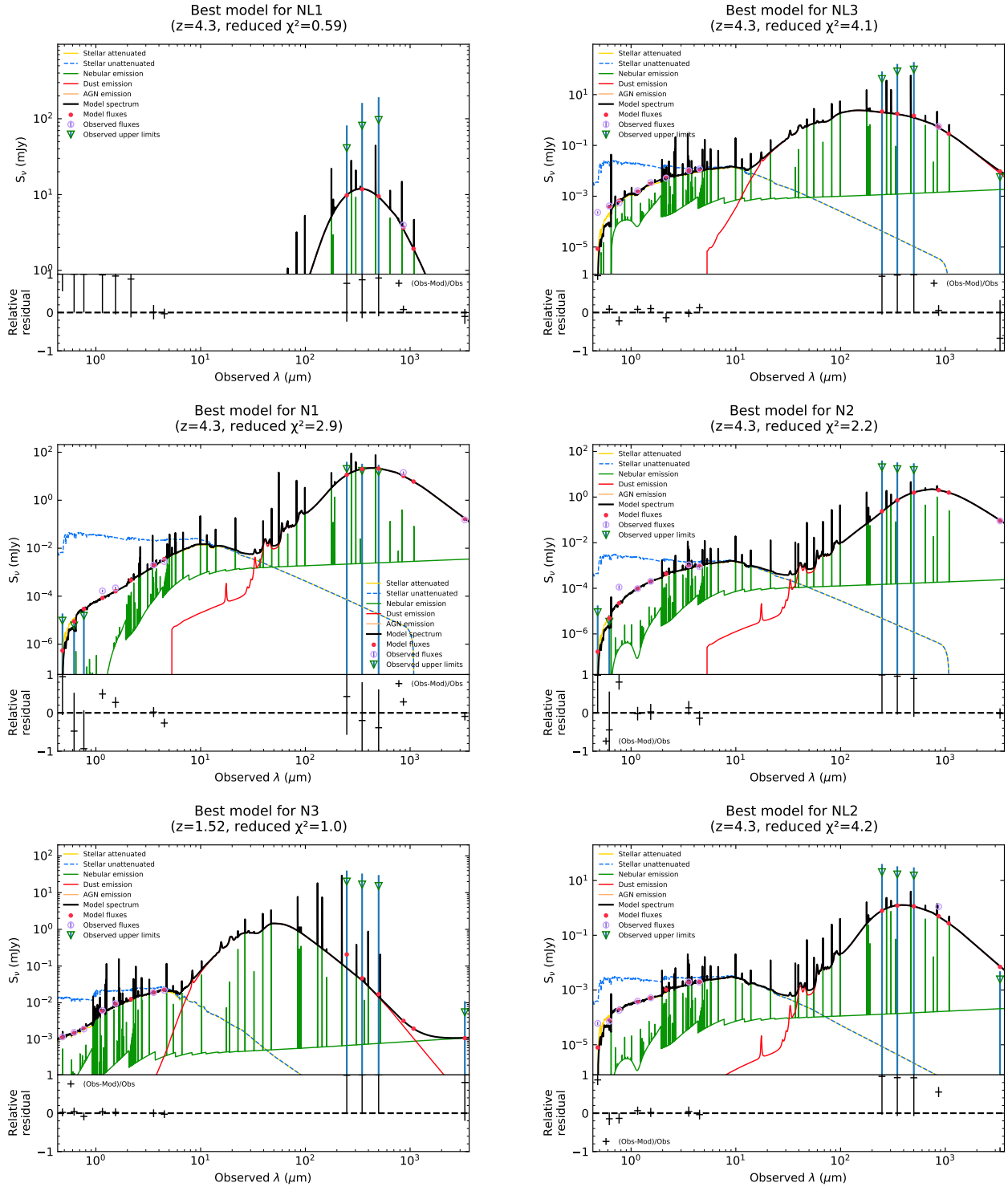


Figure C1 (Cont.).

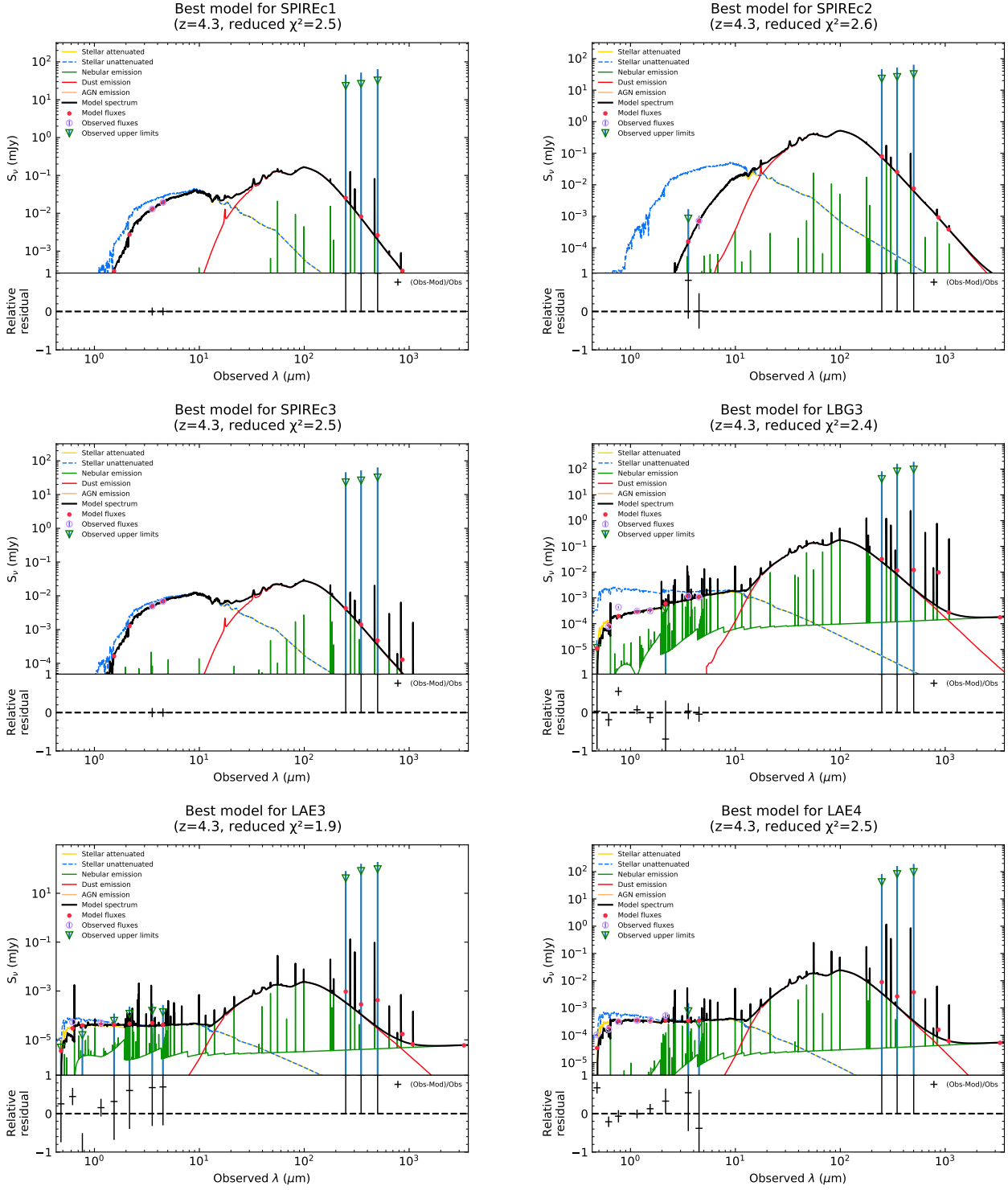


Figure C1 (Cont.).

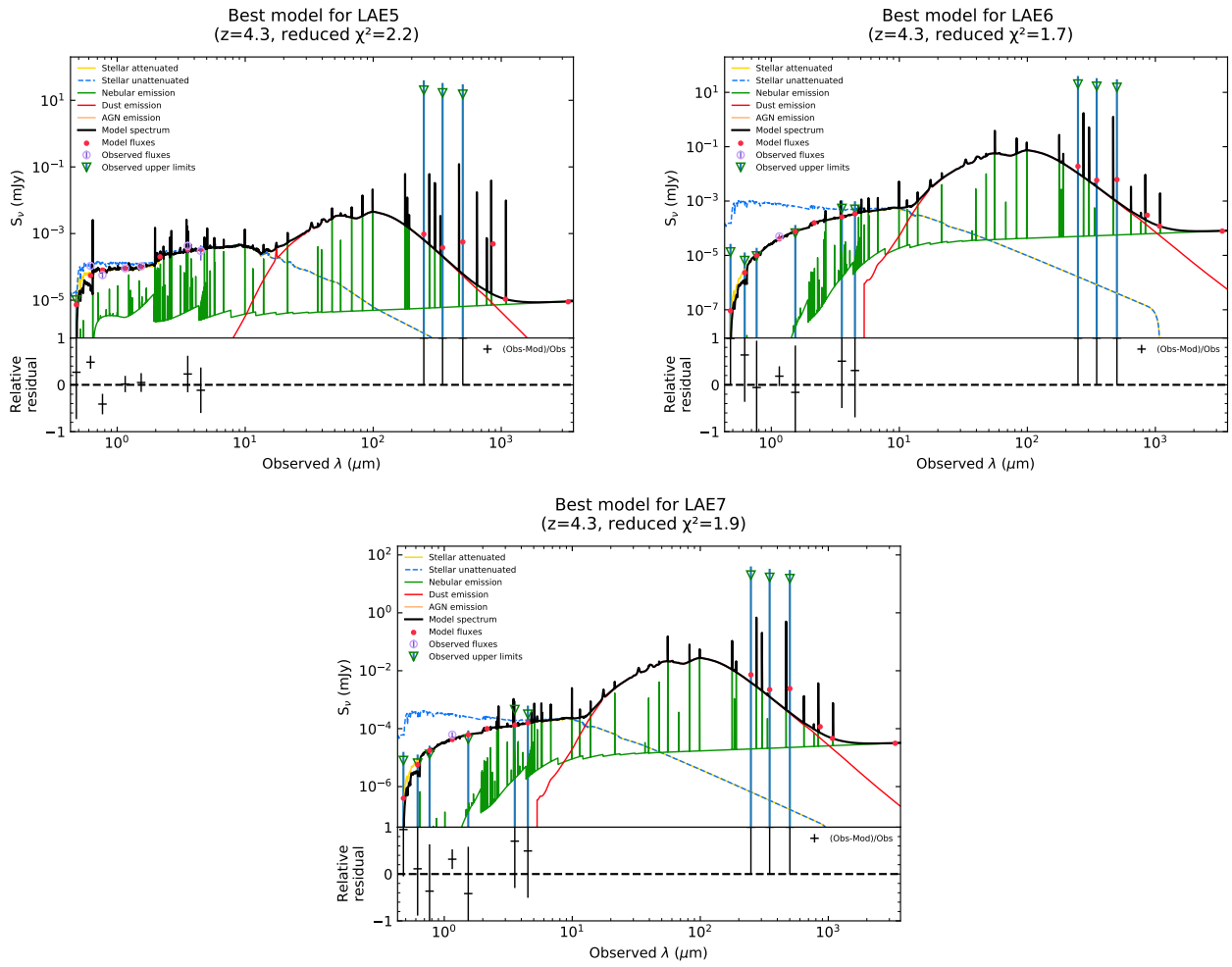


Figure C1 (Cont.).

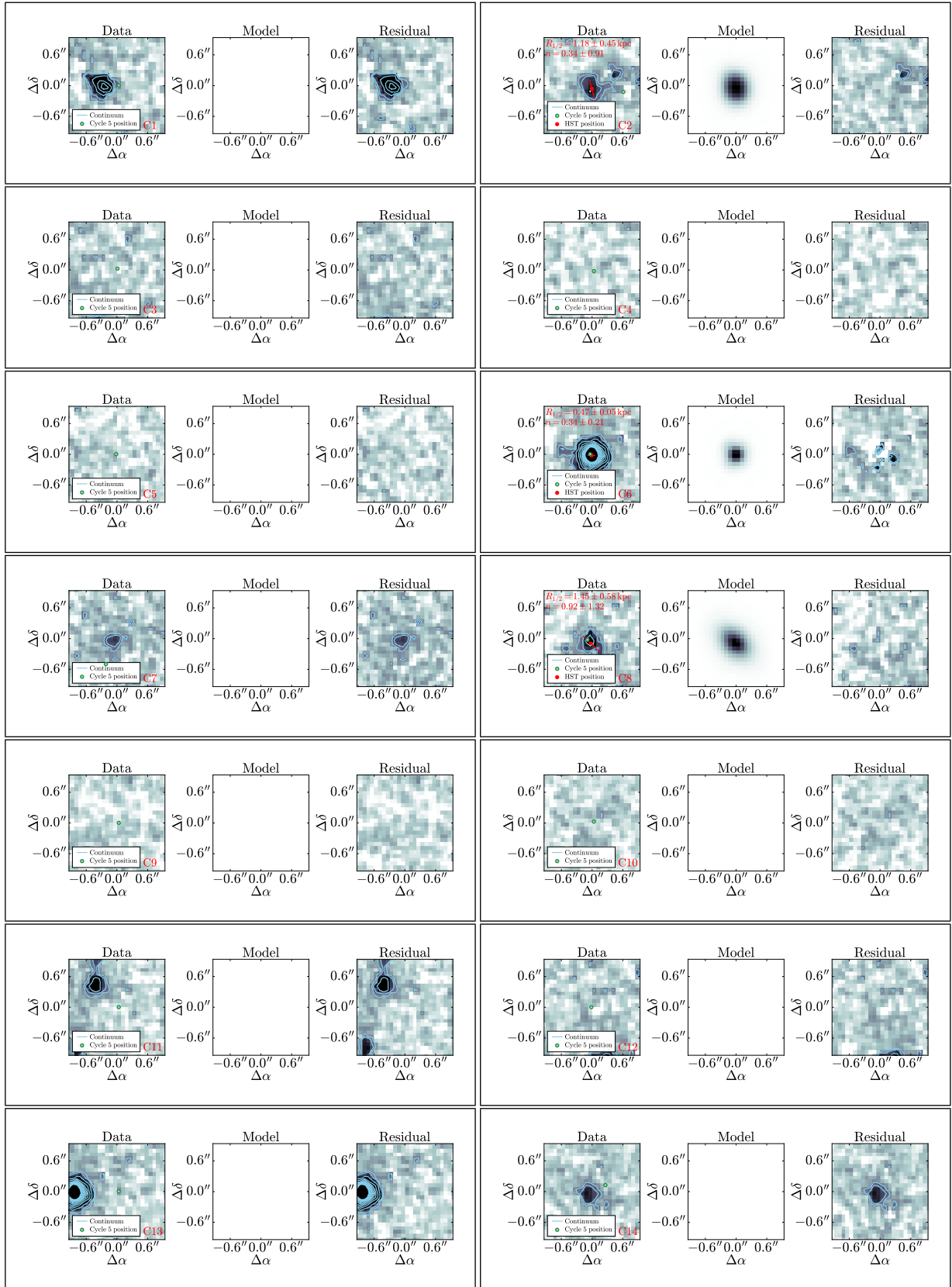


Figure D1. *Left:* Rest-frame optical (observed-frame $1.5\ \mu\text{m}$) images from our *HST* F160W imaging. Contours are 2 and 3σ , then increase in steps of 3σ . The blue points are positions found in our lower resolution Cycle 5 data, and red points are the centres of the Sérsic profiles fit to the optical image. The red bars show the lengths of the half-light diametres determined from the best-fitting Sérsic profiles, and best-fitting half-light radii and Sérsic indices are shown in the top left. *Middle:* Best-fitting model Sérsic profiles. Sources without enough pixels above 5σ were not fitted, and for these cases we leave this panel blank. *Right:* Residuals from the Sérsic profile fits.

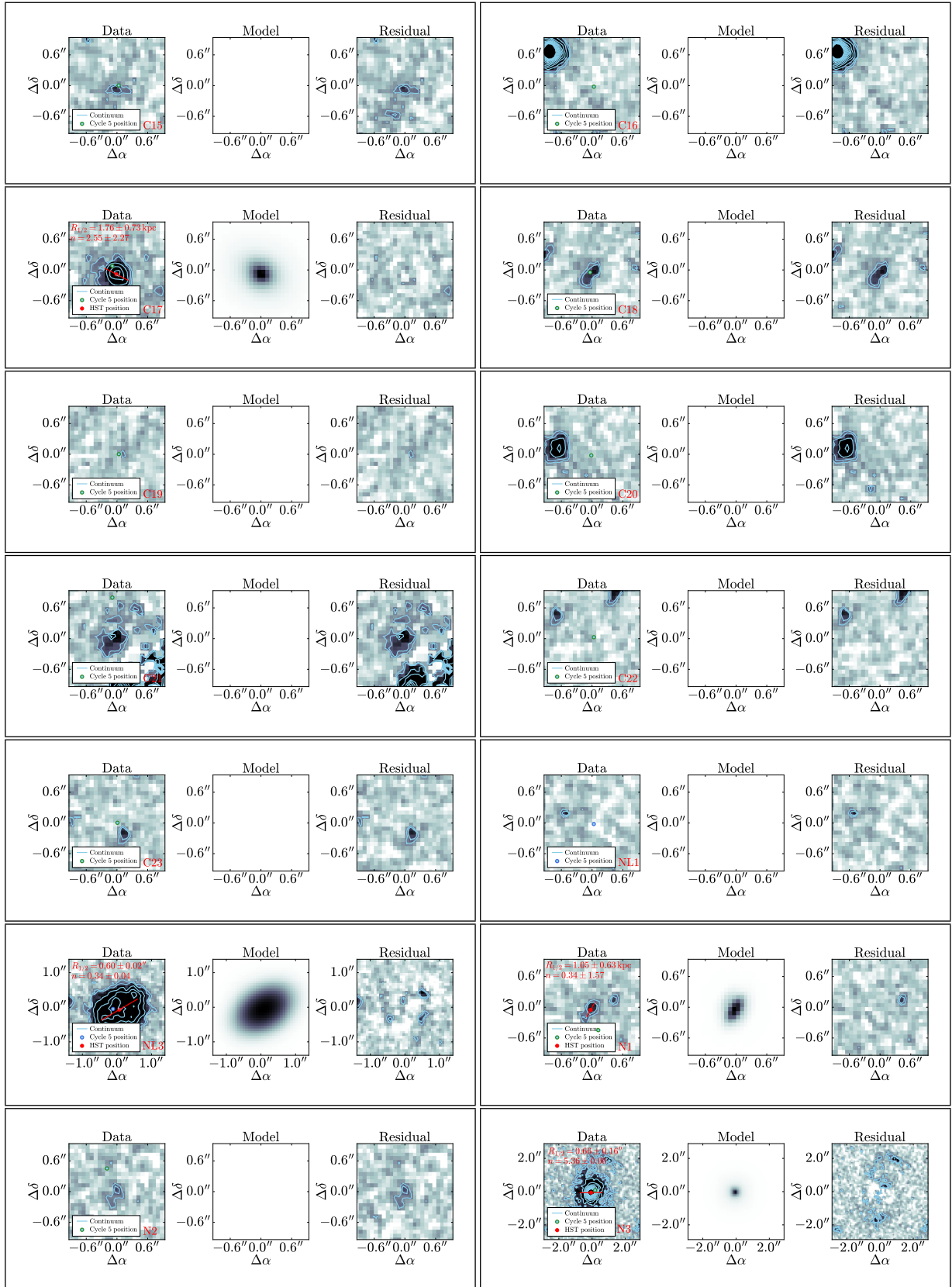


Figure D1 (Cont.).

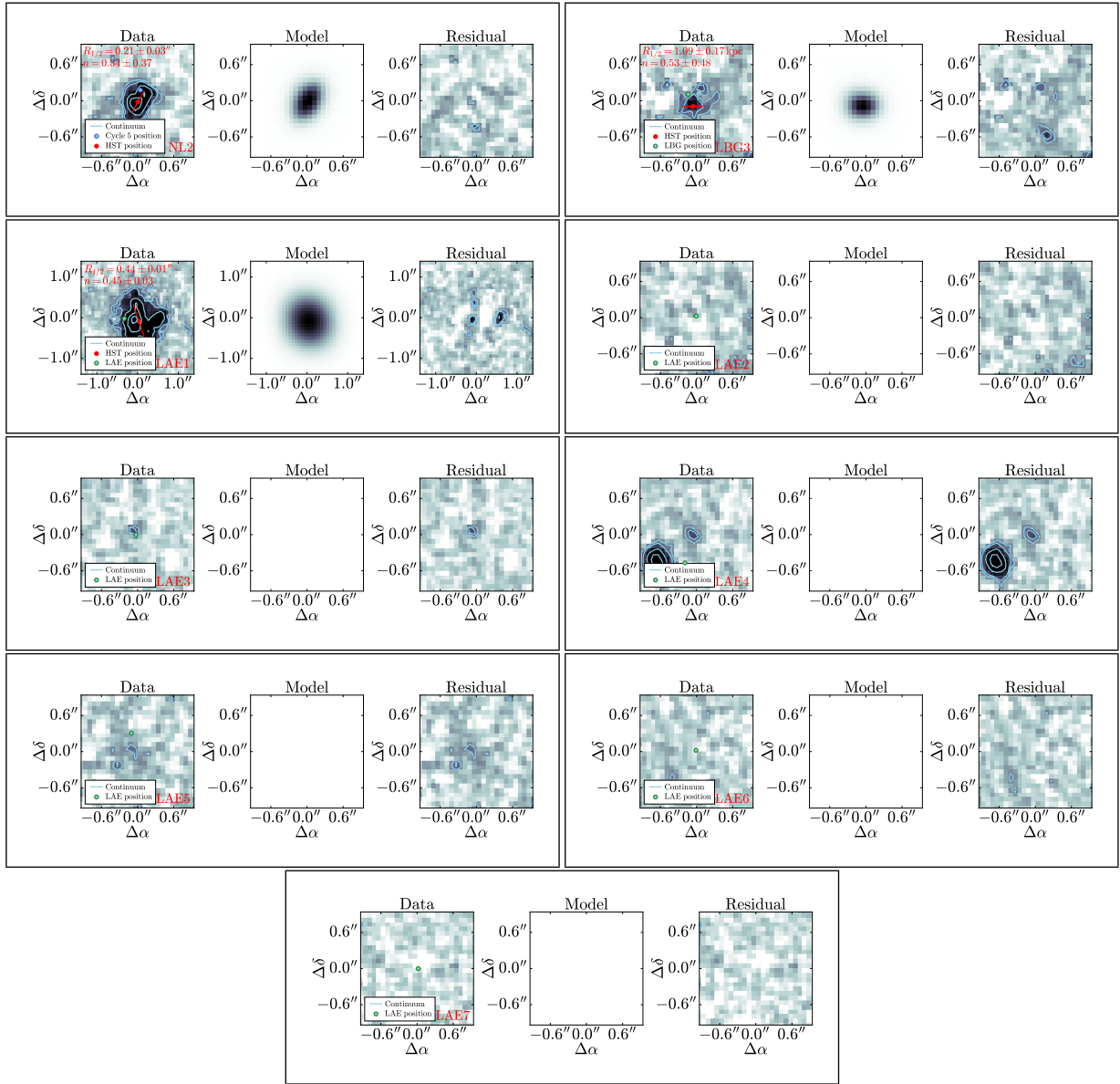


Figure D1 (Cont.).

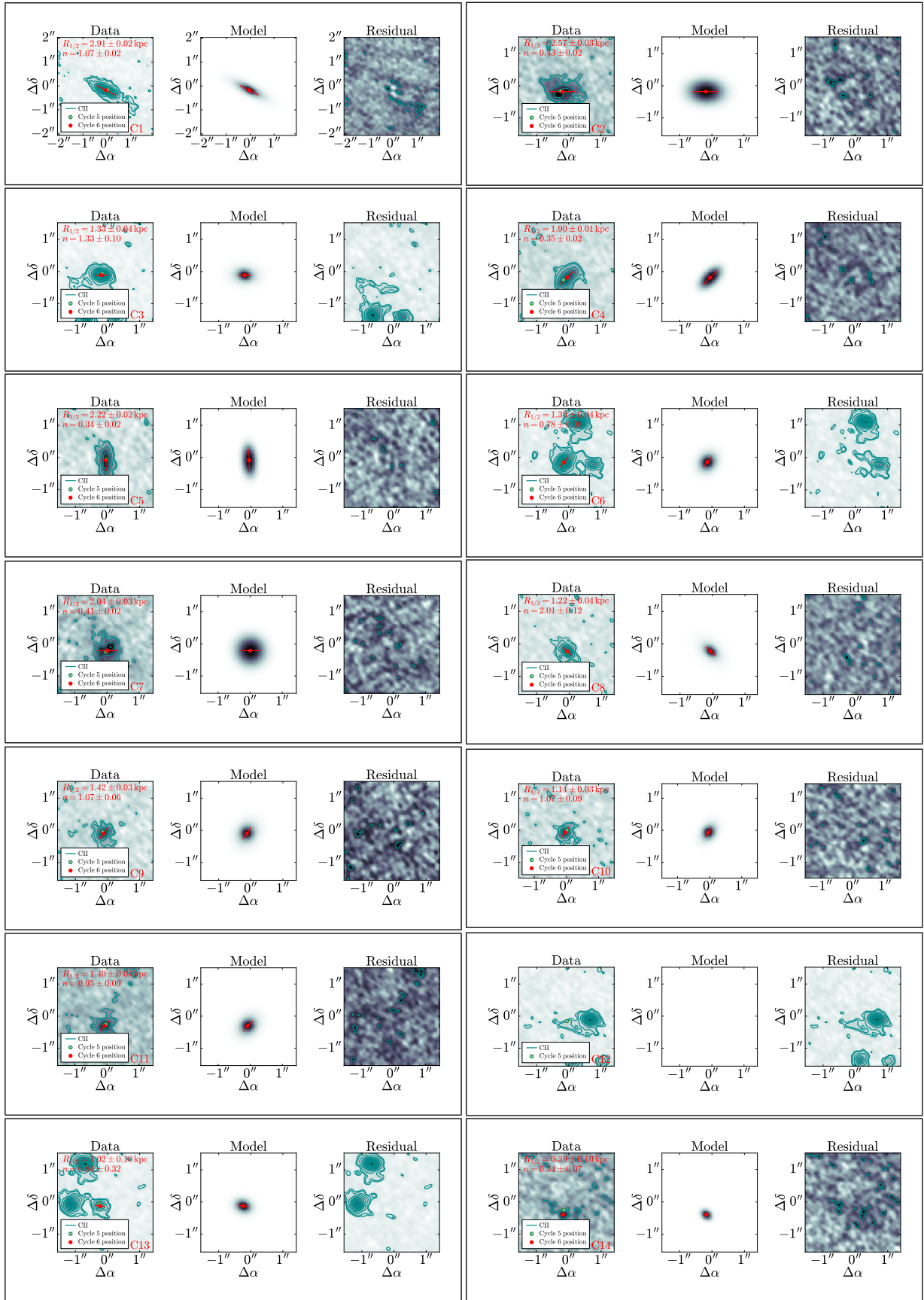


Figure E1. *Left:* [CII] images from the high-resolution Band 7 Cycle 6 data. Contours are 2 and 3 σ , then increase in steps of 3 σ . The blue points are positions found in our lower resolution Cycle 5 data, and red points are the centres of the Sérsic profiles fit to these higher resolution images. The red bars show the lengths of the half-light diameters determined from the best-fitting Sérsic profiles, while best-fitting half-light radii and Sérsic indices are shown in the top left. *Middle:* Best-fitting model Sérsic profiles. Sources undetected above 3 σ were not fitted, and for these cases we leave this panel blank. *Right:* Residuals from the Sérsic

MNRAS **000**, 1–40 (2021)

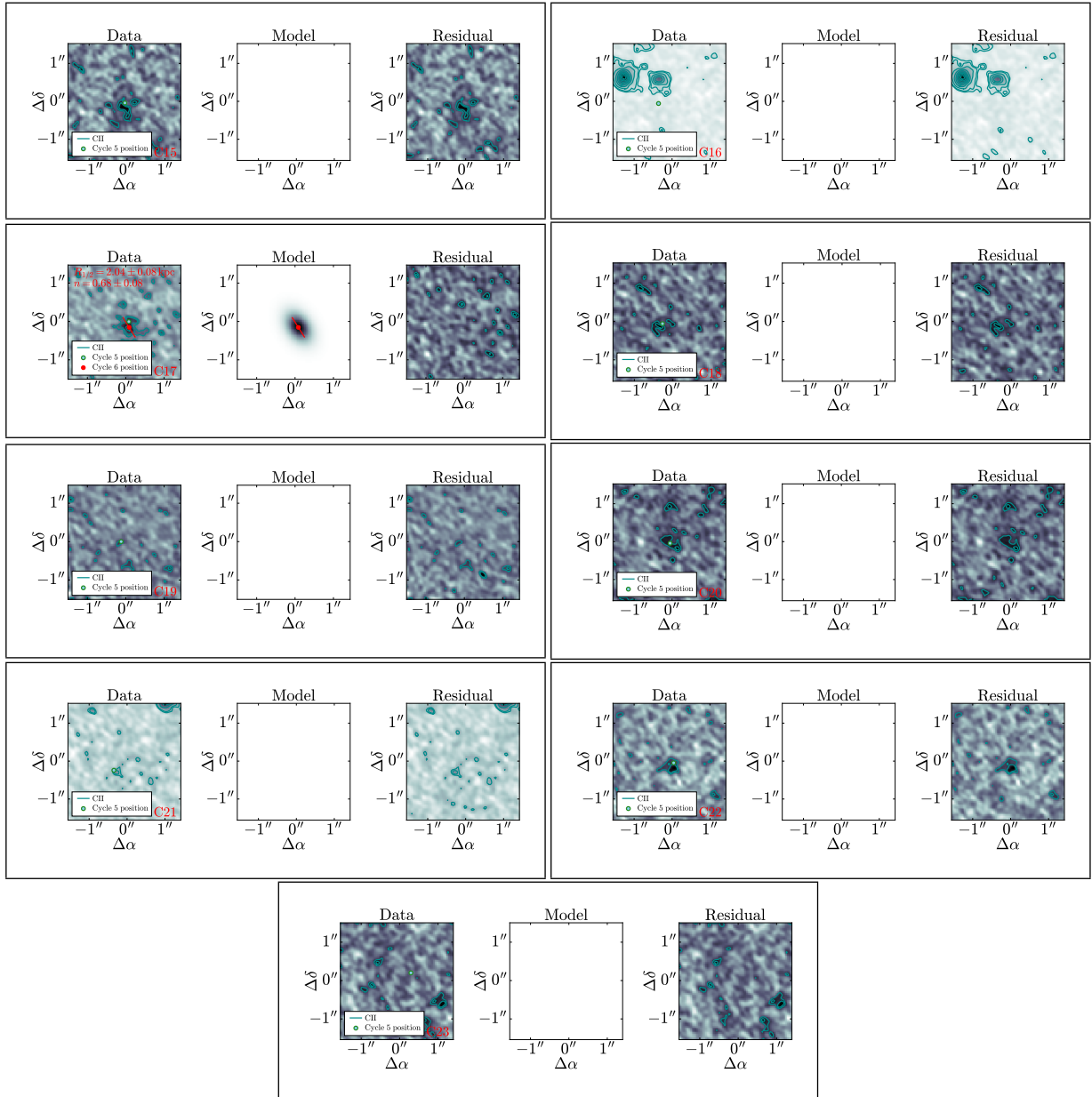


Figure E1 (Cont.).